THE FLORIDA STATE UNIVERSITY

COLLEGE OF ARTS AND SCIENCES

DIRECT REACTIONS WITH EXOTIC BEAMS AND POLARIZED

LITHIUM BEAMS

By

BRIAN T. ROEDER

A Dissertation submitted to the
Department of Physics
in partial fulfillment of the
requirements for the degree of
Doctor of Philosophy

Degree Awarded:
Summer Semester, 2006

The members of the Committee approve the dissertation of Brian T. Roeder defended on May 12, 2006.

_____
Kirby Kemper
Professor Directing Dissertation

_____
Brooks Keel
Outside Committee Member

_____
Ingo Wiedenhoever
Committee Member

_____
Jorge Piekarewicz
Committee Member

_____
Edmund Myers
Committee Member

The Office of Graduate Studies has verified and approved the above named committee members.

To Mom and Dad; thanks for helping me
to achieve…

ACKNOWLEDGEMENTS

TABLE OF CONTENTS

LIST OF TABLES

LIST OF FIGURES

ABSTRACT

In the first two chapters of this dissertation, the total cross sections for 38 different reaction products produced in the interaction of ^{48}Ca, ^{40}S and ^{42}S beams at energies around 100 MeV/nucleon with a liquid deuterium target are reported. The cross sections for the ^{48}Ca+d products are compared to those with ^{48}Ca incident on the commonly used fragmentation targets ^{9}Be and ^{181}Ta, and also to global calculations for fragmentation reaction cross sections based on the EPAX parameterization performed with the program LISE. The sizes of the measured reaction cross sections for the deuterium target were comparable to the cross sections measured on the heavier targets indicating that both nucleon addition and removal from a deuterium target can be carried out for comparative "stripping" and "pickup" reaction studies. It was also found that the charge exchange cross sections were large enough so that it should be possible to obtain nuclear structure information from these reactions. Calculations using the Johnson-Soper adiabatic model and Eikonal nucleon knockout theory were performed to study the reaction mechanisms for the "stripping" and "pickup" reactions studied in the experiment. It was found that the magnitude of the cross sections for both the single nucleon "stripping" and single nucleon "pickup" reactions were consistent with the assumption that they proceeded as direct, single step reactions.

In the third chapter of this dissertation, the recent upgrade to the Florida State University Optically Pumped Polarized Lithium Ion Source (OPPLIS) is summarized. A new laser system was installed, and the laser optics were modified to increase the laser power available for optically pumping the lithium atomic beam from about 40 mW to nearly 200 mW. This improvement, along with proper alignment of the laser beam divergence to the atomic beam divergence, increased the vector polarization t_{10} of the beam on-target from about 40% to about 60%.

FOREWARD

The study of nuclei far from the valley of stability has been a field of active research for two decades. The interest in these exotic, $\beta-$unstable nuclei that are not normally found in nature (that is to say, on Earth) stems from the need to answer certain fundamental questions that can not be answered by studying stable nuclei alone. Some of these questions include: Why are some nuclei particle bound and why do others decay spontaneously? Where did the elements heavier than iron come from and how were they made (elements lighter than iron are mostly made in stellar fusion processes in stars larger than the Sun)? And finally the ultimate question of nuclear physics: Is it possible to discover a law or set of rules that describe how the strong nuclear force between protons and neutrons behaves such that all properties of any nucleus can be predicted?

This dissertation does not even scratch the surface of most of these questions. The questions above represent problems that a nuclear physicist might spend their entire career researching. As with most dissertations, this one represents an attempt at a small step forward in answering the following question: Do the same models that nuclear physicists apply to stable nuclei, such as the single particle shell model and others, apply to exotic nuclei with high isospin (asymmetry in the numbers of protons and neutrons)? If they do, physicists already have most of the theoretical framework for answering some of these questions about nature and only measurements of the nuclei involved need to be conducted. More likely, however, certain second and third order effects on the stability of nuclei that are too weak to be observed in stable nuclei, but are very important in determining the particle stability of proton-rich and neutron-rich exotic nuclei, will be observed in the experiments. Thus, developing experimental techniques for observing the structure of proton-rich and neutron-rich exotic nuclei is important if these effects are to be observed and understood.

Over the past ten years, the removal of nucleons via knockout reactions in inverse kinematics at intermediate energies (> 50 MeV/nucleon) has become a specific and quantitative tool for studying the single-particle occupancies of stable and exotic nuclei [1]. Knockout reactions performed in inverse kinematics have been useful in observing exotic nuclei because targets of exotic nuclei are difficult or impossible to make (see chapter 1). Single nucleon knockout reactions such as $^9Be(^ZA,^ZA\text{-}1)X$ (where X represents

the undetected left-over nucleons from the reactions) have been particularly useful in the study of nuclei near the proton and neutron driplines (the limits of particle instability) because of their relatively high cross section [1,2]. The high cross section helps to overcome the problem of low beam rates ($1\text{-}10^5$ particles per second) relative to what is commonly used in stable beam experiments ($\sim 10^9$ particles per second). These reactions probe the single nucleon hole states of a given nucleus (see Chapter 1: section I). However, these reactions do not probe the single particle states of these nuclei. Thus, nucleon pickup reactions of the type $d(^ZA,^{Z+1}A+1)n$ and $d(^ZA,^ZA+1)p$ should also be performed to complete the study of the single particle structure of a given nucleus. Such information will help test the validity of the single particle shell model and other models for exotic nuclei.

Chapter 1 of this dissertation reports the cross section for several pickup reactions with stable and exotic nuclei at intermediate energies (100 MeV/nucleon) to see if future experiments of this type are feasible. These cross sections are compared to the cross sections for single nucleon knockout with the same beams. In Chapter 2, the total cross sections for both the nucleon pickup and nucleon knockout reactions are compared to calculations of the cross section to determine whether the residual nuclei are populated via single particle, direct transfer reactions or by some other statistical processes.

Chapter 3 contains the contributions of the author to the recent upgrade of the Florida State University optically pumped polarized lithium ion source (OPPLIS) [3]. The purpose of the upgrade was to increase the nuclear polarization of the ^{7}Li beam as observed on target during experiments [4], thus allowing for more precise experiments to be conducted in the near future. OPPLIS is a unique device that produces polarized ^{6}Li and ^{7}Li ions for nuclear scattering experiments. Depending on the magnetic substate of the spin of the incoming ion, the cross section for a given reaction can be enhanced or reduced. Measurements of the same reaction with different beam spin projections lead to the measurement of analyzing powers, which are spin-dependent observables that can be used to measure the strength of spin-orbit (first order) and quadrupole (second-order) interactions between the scattering nuclei. Measurements of analyzing powers also provide information about the scattering reaction mechanism that would otherwise not be observed if only the reaction cross section was measured. In addition, ^{6}Li and ^{7}Li,

although stable nuclei, are loosely-bound by 1.5 MeV and 2.5 MeV respectively [5]. The loosely-bound property of ^{6}Li and ^{7}Li makes them similar to the loosely-bound, exotic nuclei found near the proton and neutron driplines. Thus, understanding the reaction mechanisms involved in lithium scattering through experiments with polarized lithium beams will provide insight into the reaction mechanisms that are important in the scattering of exotic nuclei. Such information may help decipher some of the unexplained results of scattering experiments with exotic nuclei, as well as lead to the improvement of current scattering models. This information will also be vital if it is found that new models for the scattering of nuclei need to be developed. Only the details of the OPPLIS upgrade are included in this work, but the results of the upgrade will hopefully lead to the improved study of the scattering reaction mechanisms mentioned above.

CHAPTER 1

PARTICLE TRANSFER REACTIONS WITH STABLE AND EXOTIC BEAMS AT INTERMEDIATE ENERGIES

I. Background

Single nucleon transfer reactions have been widely used at low beam energies (5-10 MeV/nucleon) to study the structure of the atomic nucleus since the 1950s. In a typical single nucleon transfer reaction experiment, a beam of light ions such as deuterium (*d*), tritium (*t*), or ^{3}He, is accelerated and then impinged on a stationary target of some stable nucleus, and the resulting outgoing reaction products are detected. Often, detectors are placed at several angles with respect to the beam axis, and data is recorded for the energy of the outgoing light particle, the type of particle it is, and the number of particles detected for a given target thickness and beam flux. These data lead to the identification of the reaction that took place between the beam nucleus and the target nucleus, measurements of any excited states that may have been populated in the residual nucleus, and an angular distribution of the differential cross section ($d\sigma/d\Omega$) for the population of specific excited states. Data of this type from reactions performed in forward kinematics such as $^ZA(d,p)^{Z+1}A+1$, $^ZA(d,n)^{Z+1}A+1$, $^ZA(^3He,d)^{Z+1}A+1$, $^ZA(d,t)^ZA-1$, $^ZA(d,^3He)^{Z-1}A-1$ and others have been studied within the theoretical framework of the Distorted Wave Born Approximation (DWBA) [1] and other techniques to explain the results of certain experiments that would otherwise appear ambiguous.

As an example of how single particle transfer reactions can explain the structure of a nucleus, as well as shed light on the results of different experiments, consider the nucleus ^{49}Sc. Although ^{49}Sc is not found in nature, it can be made in nuclear reactions such as $^{48}Ca(^3He,d)^{49}Sc$ [2,3] and $^{50}Ti(d,^3He)^{49}Sc$ [5]. ^{49}Sc can also be studied by observing the characteristic gamma rays that result from the β^--decay of ^{49}Ca, which can be made with the reaction $^{48}Ca(n,\gamma)^{49}Ca$ among others [5]. The excited states in ^{49}Sc observed through the gamma decays resulting after the β^--decay of ^{49}Ca are shown in figure I.1.
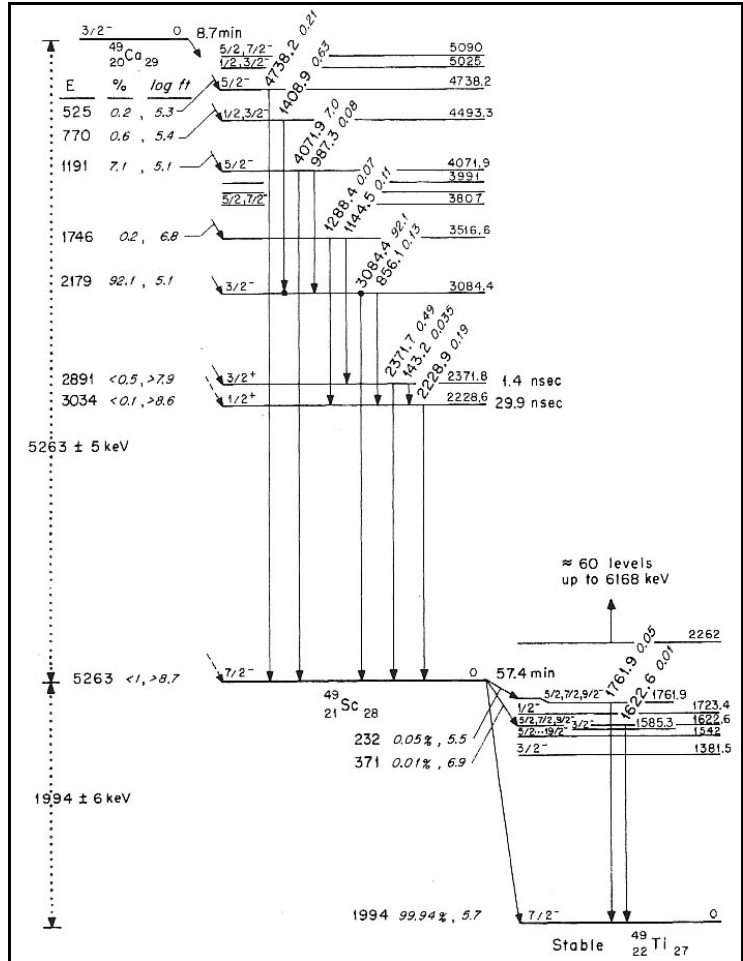
Figure I.1: β^--decay of ^{49}Ca creating excited states in ^{49}Sc. Excited states in ^{49}Sc are observed via their characteristic gamma decays [5].

In the experiment in [5], there were eight separate levels populated in ^{49}Sc between the ground state and 4.738 MeV. While the results shown in figure I.1 provide some information about the structure of the excited states in ^{49}Sc, the information gained about the nucleus is limited. For example, due to the difference in binding energy between the ground states of ^{49}Ca and ^{49}Sc, excited states in ^{49}Sc above 5.2 MeV [5] are not observed with the β^--decay of ^{49}Ca. Also, information about the possible spins and parities of the excited states in ^{49}Sc is limited because the spins and parities can only be inferred based on if the β^--decay to these states is allowed or forbidden (In β^--decay experiments, allowed decays occur when the parent nucleus decays to excited states in the product (daughter) nucleus with similar spin and parity to the ground state of the parent nucleus. These decays are the most likely and thus occur most frequently in the experiment.

5

Forbidden decays occur infrequently in experiments and represent β^--decays to excited states in the daughter nucleus with different spins and parities from the ground state of the parent nucleus.). Finally, if the β^--decay to a given state in ^{49}Sc is strongly forbidden, it may not even be observed in the experiment above the background if not populated by gamma decays from higher-lying excited states.

For comparison, if ^{49}Sc is made via a single particle transfer reaction, such as the particle stripping reaction $^{48}Ca(^7Li,^6He)^{49}Sc$ [6], then different results are obtained. In this experiment, a single proton is transferred from the ^{7}Li to the ^{48}Ca target, and the resulting ^{6}He was detected at different angles with respect to the beam axis. A spectrum showing the states populated in ^{49}Sc is shown in figure I.2a. Several dominant peaks corresponding to excited states in ^{49}Sc are immediately obvious, while other excited states are barely observed at all. Certain excited states, such as the 3.81 MeV and 5.09 MeV states, which were not observed in the ^{49}Ca β^--decay experiment, are strongly populated with this reaction. Finally, if angular distributions of the differential cross sections for the ^{49}Sc states are compared with DWBA calculations, the spins and parities of the states can be determined.

However, this is not the end of the story. Suppose instead the single particle pickup reaction $^{50}Ti(d,^3He)^{49}Sc$ is investigated [5], in which a single proton is removed from ^{50}Ti to make ^{49}Sc and the resulting ^{3}He particle is detected. A spectrum showing the states in ^{49}Sc populated in the $^{50}Ti(d,^3He)^{49}Sc$ reaction is shown in figure I.2b. Naively, one might expect that the same excited states detected in the $^{48}Ca(^7Li,^6He)^{49}Sc$ reaction would be observed with similar cross sections. While the $^{50}Ti(d,^3He)^{49}Sc$ reaction populates many of the same excited states in ^{49}Sc, some states that were strongly populated in both the ^{49}Ca β^--decay and $^{48}Ca(^7Li,^6He)^{49}Sc$ experiments (most notably the 3.08 MeV state) were only weakly populated or not observed at all. Also, some states that were only weakly populated in the $^{48}Ca(^7Li,^6He)^{49}Sc$ experiment, such as the 2.23 MeV and 2.36 MeV states, were strongly populated in the $^{50}Ti(d,^3He)^{49}Sc$ experiment. These results seem to suggest that there is some underlying reason that different excited states in ^{49}Sc are selectively populated depending on the reaction used to produce the ^{49}Sc.
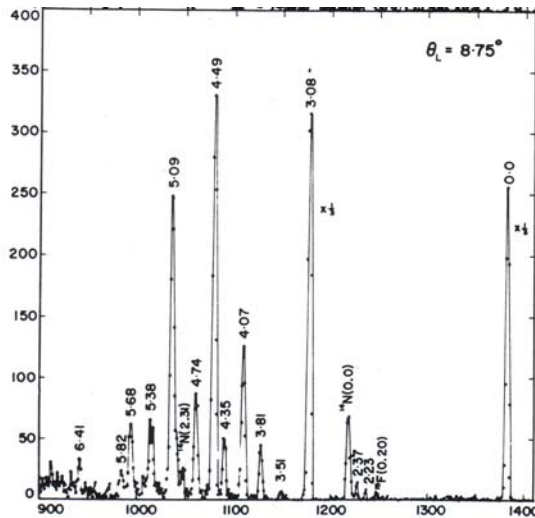
Figure I.2a: Spectrum of states populated in the $^{48}Ca(^{7}Li,^{6}He)^{49}Sc$ reaction [6]. The single particle states are represented by the large peaks in the spectrum.
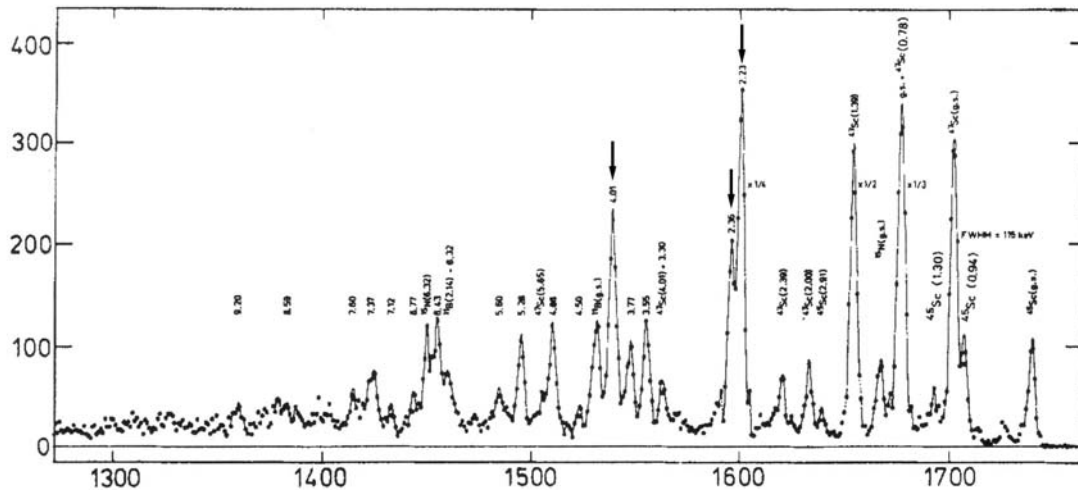
Figure I.2b: Spectrum of states populated in the $^{50}Ti(d,^{3}He)^{49}Sc$ reaction [5]. The strong single nucleon hole states at 2.23 MeV, 2.36 MeV and 4.01 MeV are shown with arrows. The large peaks at the low energy end (right side) of the spectrum were due to contaminants.

The difference in the results between the $^{48}Ca(^{7}Li,^{6}He)^{49}Sc$ and the $^{50}Ti(d,^{3}He)^{49}Sc$ experiments is most easily explained with the single particle shell model of Mayer and Jensen [7]. According to this model, ^{49}Sc in its ground state has filled neutron shells up to the $1f_{7/2}$ shell and filled proton shells up to the $1d_{3/2}$ shell with a single proton in the $1f_{7/2}$ shell. Excited states of ^{49}Sc are modeled by promoting the protons and neutrons to higher shells. The proton shell structures of ^{49}Sc, ^{48}Ca, and ^{50}Ti are shown in figure I.3. It should be noted here that ^{48}Ca is a *doubly-magic* nucleus, meaning that it is very stable in its ground state configuration and is not easily excited because both the protons and neutrons

7

are in closed shell configurations. It costs energy (about 3.8 MeV) to excite the ground state configuration of ^{48}Ca [8]. Therefore, to make ^{49}Sc from ^{48}Ca as in $^{48}Ca(^{7}Li,^{6}He)^{49}Sc$, it is easiest to simply add the proton to the proton shells above the ^{48}Ca to make the ground and excited states of ^{49}Sc observed in the experiment. Excited states that can be modeled in this way are referred to as *single particle states*, because they have the structure of a single nucleon above a closed shell configuration and were populated in a reaction that transferred a single specific particle to the target nucleus. Similar to ^{48}Ca and ^{49}Sc, ^{50}Ti also has a filled $1f_{7/2}$ neutron shell, but has two protons in the $1f_{7/2}$ proton shell. In the case of $^{50}Ti(d,^{3}He)^{49}Sc$, a proton must be removed from the ^{50}Ti in order to make ^{49}Sc. Removing a proton from the $1f_{7/2}$ shell makes the ground state of ^{49}Sc, but to create excited states in ^{49}Sc from ^{50}Ti, the proton must be removed from lower shells. States that can be modeled in this way are referred as *single hole states*, because they have a structure of a single nucleon missing from the original closed shell configuration and were populated in a reaction that removed a single specific particle from the target nucleus. Since the single particle states and single hole states are made in different reactions and have different structure, it is reasonable to suggest that this is the underlying reason why certain states in ^{49}Sc are selectively populated according to the reaction used to produce them. Once the spins and parities of the individual excited states are measured, the resulting shell structure of each single particle or single hole state can be determined.

By performing two types of single particle transfer reactions, the ground and low-lying excited states of ^{49}Sc have been measured and classified into two separate types of states. Note that the underlying structure of the states in ^{49}Sc was not uniquely determined with one experiment, and important information about the excited states would have been missed if both experiments had not been performed. One could imagine further experiments in which the single particle and single hole neutron states of ^{49}Sc were investigated with reactions like $^{48}Sc(d,p)^{49}Sc$ or $^{50}Sc(d,t)^{49}Sc$. Perhaps these experiments would selectively populate excited states in ^{49}Sc that had not previously been observed, or illuminate the structure of states that were not strongly populated in other reactions. These experiments are difficult because both ^{48}Sc and ^{50}Sc are radioactive and
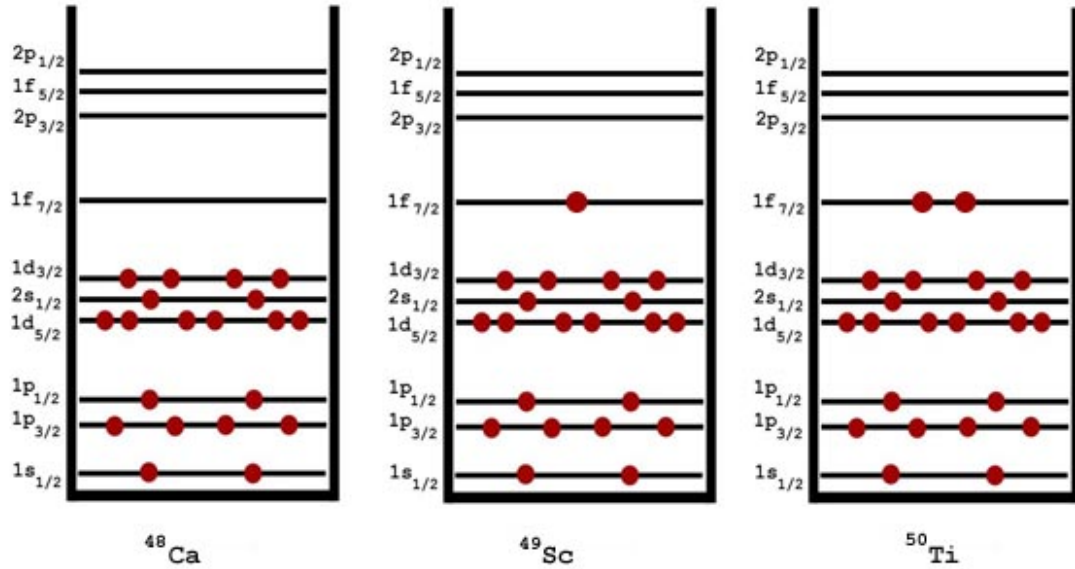
Figure I.3: Single Particle Shell Models of the ^{48}Ca, ^{49}Sc, and ^{50}Ti ground states

decay too quickly to make targets out of them. However, such an experiment can be conducted if it is performed in inverse kinematics with exotic (radioactive) beams on a light target, such as deuterium. The work presented in this dissertation investigates the feasibility of measuring single particle transfer reactions with exotic beams such that the structure of both stable and exotic nuclei can be better understood in future experiments.

II. Experiment Proposal

Figure I.4 shows a drawing of the chart of the particle bound nuclei. The stable nuclei found on Earth are shown in black, and the unstable, exotic nuclei that are known to exist are shown in beige, and nuclei that are thought to exist according to theory, but have not been observed yet are shown in the green "Terra Incognita" region . While the exotic nuclei shown in beige have been observed in the laboratory, to date they have not been as well studied as the stable nuclei due to the difficulty in performing experiments with them. Experiments with exotic nuclei are limited by several factors. First, exotic nuclei, in general, have short half-lives ($T_{1/2}$ < 1 day), although there are some with half-lives of years or longer. As was mentioned before, this prevents experiments from being conducted in the traditional way in forward kinematics with a light ion beam and a heavy target, since targets made of exotic nuclei would decay too quickly to be measured in

9

experiments. So, most experiments with exotic nuclei must be conducted in inverse kinematics with beams of exotic nuclei on stationary targets of stable nuclei.
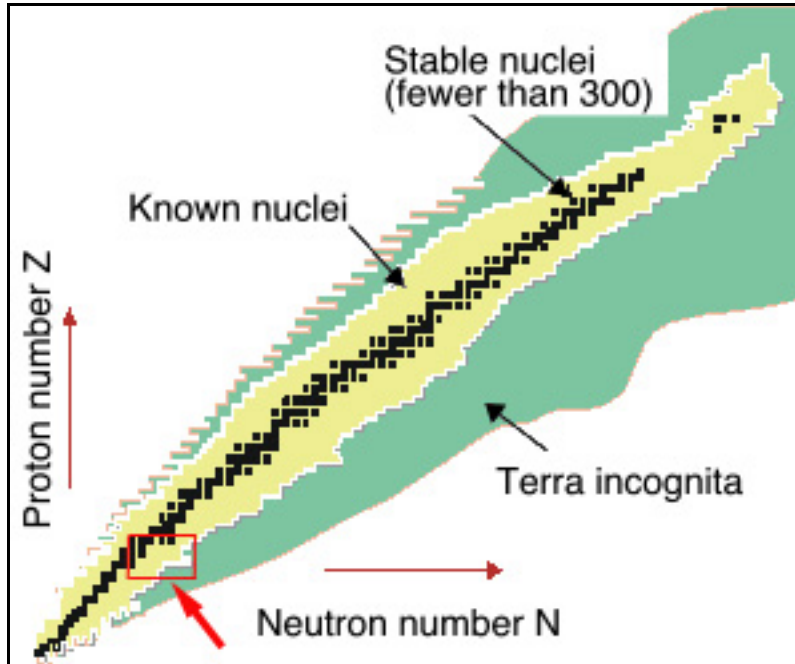
Figure I.4: Chart of known nuclei plotted with respect to proton number *Z* and neutron number *N*. See the text for an explanation of the different regions. The red box indicates the region where the nuclei studied in this dissertation are located.

Currently, exotic beams of nuclei are produced in one of two ways, although other methods are under development. The first method is known as the Isotope Separation Online or ISOL technique. The ISOL technique produces exotic beams with nuclear reactions involving a beam of intermediate to high-energy protons (50 MeV to ~1 GeV) scattering from a thick, heavy target material that often completely stops the proton. The most commonly used target material is uranium carbide, which fissions into a wide assortment of exotic, neutron-rich nuclei when excited by the proton beam. Other targets are also used when beams of specific isotopes are required. Once the exotic nuclei are produced in the ISOL target, the target material is then heated such that the exotic atoms diffuse out. Then, the exotic atoms are ionized, magnetically separated and focused into a beam for experiments. The major limitation of this technique is that the short-lived beams with ($T_{1/2}$ < 100 ms) cannot be separated quickly enough from the target material before they decay. Also, separating beams from the target material can at times be very difficult because the exotic atoms form chemical bonds with the target material.

Figure I.5: Chart of nuclei showing some of the nuclei populated in this experiment [9]. Note that most of the neutron-rich nuclei in this region have short $T_{1/2}$. The ^{40}S and ^{42}S beams used in the experiments, for example, both have $T_{1/2} < 10$ sec. These beams would be difficult to produce with ISOL due to the chemistry involved in separating them from the target material.

The second method of producing exotic beams is the heavy-ion fragmentation technique. In this technique, a beam of stable heavy ions bombards a target of light nuclei, often ^{9}Be or ^{12}C, at intermediate beam energies (> 50 MeV/nucleon). When the heavy-ions react in the target, they are fragmented through a two-step process known as abrasion-ablation [10]. These processes create a wide variety of nuclei lighter than the initial beam [e.g. 11]. With modern separation techniques involving magnetic separation and energy loss (see section III.B), beams of specific exotic nuclei can be created. These beams often contain more than one type of nucleus, but reactions that come from the beam contaminants can be separated in the data using time of flight and other measurements. With heavy ion fragmentation, in principle, beams of any nucleus that is particle bound ($T_{1/2} > \sim 10^{-9}$ sec) can be made for experiments. Another advantage of this

technique is that although the beam rates are often quite low ($1 - 10^5$ particles per second) in comparison with normal experiments (~ 10^9 particles per second), thicker targets can be used in experiments since the exotic beams are at intermediate energies (> 50 MeV/nucleon). While the cross section for a given reaction may be small, the experiments can still be performed in a reasonable amount of time (few days) because the thick target increases the event rate of the reaction.

Over the last ten years, several experimental techniques have been developed to study exotic beams produced with heavy-ion fragmentation. One of the most successful techniques for probing the structure of exotic nuclei has been the single-nucleon knockout reaction [12-16]. These reactions collect spectroscopic information on states that have the structure of a single hole in the beam nucleus [12, 17], similar to the types of states populated in the reaction $^{50}Ti(d,^3He)^{49}Sc$ [5] discussed in section I. However, to date, complimentary reactions that populate single particle states on exotic nuclei have not been measured. Therefore, measurements of nucleon pickup reactions, such as $d(^ZA,^{Z+1}A+1)n$ and $d(^ZA, ^ZA+1)p$ reactions in inverse kinematics, are required to fully characterize the single particle structure of exotic nuclear species.

The goal of the experiment in this dissertation was to investigate the feasibility of measuring single nucleon transfer reactions in inverse kinematics at intermediate beam energies (~100 MeV/nucleon). Measurements of the inclusive cross sections for a well-studied neutron-rich stable beam, ^{48}Ca, and for two neutron-rich exotic beams, ^{40}S and ^{42}S are reported. The constraints of high beam energy and inverse kinematics were chosen because exotic beams (with masses A>20) near the neutron dripline are only available using heavy-ion fragmentation, as discussed above. A secondary target of liquid deuterium was used, provided by RIKEN [18]. The advantage of this target over a deuterium gas or CD_2 target was that it provided a thick deuterium target without background from the reactions of the beams with carbon.

The reaction mechanisms and deduced spectroscopic strengths, when using normal kinematics (d,p) and (d,n) reactions and stable targets, are relatively well understood at low energies. If the cross sections for these single nucleon transfer reactions are sufficiently large at intermediate energies, then the experimental setup

12

described in section III can be used in future experiments to study single-particle spectroscopy for a wide range of exotic beams.

Other reactions, such as single-nucleon knockout, which produce heavy residues of similar magnetic rigidity to the transfer reaction products, were simultaneously observed during collection of the data. Thus, a comparison of the cross sections of the transfer reactions and the single-nucleon knockout reactions can be made. The cross sections for multi-nucleon removal and charge exchange reactions with the deuterium target are also reported.

Most single-nucleon knockout experiments have used either ^{9}Be [12,15,16] or ^{12}C [13,14] targets. The present work employs a deuterium target and hence the results of the cross section measurements can also be compared with experiments involving deuterium beams and stable targets at low energies. Like the ^{9}Be target, the deuteron has no bound excited states, is lighter than the beam projectile, and can be excited during the reaction. An eikonal few-body model description of the single nucleon knockout reaction on the (two-body) deuteron target is presented in Chapter 2 and the resulting cross sections are compared with the experimental data.

III. Experiment Setup Overview

A. Primary Beam Production

Experiment 02010 was conducted at the National Superconducting Cyclotron Laboratory (NSCL) from November 13-17, 2003. The experiment required a ^{48}Ca primary beam at the highest energy possible in order to maximize the amount of ^{40}S and ^{42}S exotic beams produced for the radioactive beam runs. The ^{48}Ca beam was produced in an Electron-Cyclotron Resonance (ECR) ion source as ^{48}Ca^{8+} and injected into the K500 cyclotron where it was accelerated to a kinetic energy of about 12 MeV/nucleon. The beam was then extracted from the K500 cyclotron and passed through a transfer line. While in the transfer line, the beam was passed through a carbon stripper foil, which ionized the beam further into ^{48}Ca^{19+}. Next, the beam was injected into the K1200 cyclotron and accelerated to 141.96 MeV/nucleon. Finally, the primary ^{48}Ca beam was extracted from the K1200 cyclotron and entered the A1900 fragment separator.

For the reactions in the experiment involving the ^{48}Ca beam, the energy of the primary beam needed to be degraded so that it would have kinetic energy similar to that

of the ^{40}S and ^{42}S exotic beams. In this way, the cross sections for the reactions involving the three beams could be directly compared at similar center of mass energies. To degrade the energy of the ^{48}Ca beam, the beam was passed through a thick aluminum wedge at the middle position of the A1900. Reactions of the ^{48}Ca beam with the aluminum in the wedge were filtered out by the dipole and quadrupole magnets in the A1900 after the wedge. The ^{48}Ca beam became fully ionized to ^{48}Ca^{20+}, and the energy was degraded to 102 MeV/nucleon. This beam was then transferred from the A1900 to the S800 spectrograph for the experiments with the ^{48}Ca beam. Details about the ^{48}Ca primary beam used in the experiment can be found in table I.1.

B. Exotic (Secondary) Beam Production

The ^{48}Ca^{19+} primary beam at 141.96 MeV/nucleon extracted from the K1200 cyclotron was also used to produce the ^{40}S and ^{42}S exotic beams. After entering the A1900 fragment separator, the ^{48}Ca^{19+} beam bombarded a beryllium target of thickness 650 mg/cm^2. This interaction produced a wide variety of fragments in a cocktail beam, including the ^{40}S and ^{42}S exotic beams of interest. In order to separate the ^{40}S and ^{42}S beams from the other fragments, the A1900 fragment separator employed three techniques to filter the unwanted contaminant fragments and the left over primary beam out of the exotic beam.

The first technique was the magnetic separation technique, which separates beam particles according to their mass to charge (*M/Z*) ratio and velocity. To see how this works, suppose an ion with mass "*M*", charge "*Z*" and velocity "$\vec{v}$" enters a dipole magnet with bending radius "ρ" and static magnetic field "$\vec{B}$". If there is no electric field acting on the ion, then the centripetal force on the ion is equal to the Lorentz force as follows,

where it is assumed that the ion is traveling at non-relativistic velocities. If the velocity of the ion is perpendicular to the magnetic field, then the above equation reduces to

$$F_{centripetal} = F_{Magnetic}$$

$$\frac{Mv^2}{\rho} = Z(\vec{v} \times \vec{B})$$

$$\frac{M}{Z}v = B\rho$$

such that a dipole magnet with field of magnitude *"B"* and bending radius *"ρ"* only allows ions with charge to mass ratio *"M/Z"* and velocity *"v"* to pass through it. Other ions that do not have the proper *M/Z* ratio are bent either too much or too little by the beam and thus do not make it around the magnet. The quantity *"Bρ"* is referred to as the magnetic rigidity of a particular ion.

All the beams in experiment 02010 have energies at around 100 MeV/nucleon and thus travel at relativistic velocities of around 0.43**c**. For a relativistic ion traveling at a velocity $\vec{v}$ in a static magnetic field $\vec{B}$, the equations of motion with respect to energy and momentum are [19],

$$\frac{d\vec{p}}{dt} = Z(\vec{v} \times \vec{B})$$

$$\frac{dE}{dt} = 0$$

where $\vec{p}$ is the relativistic three momentum of the ion, *E* is the energy of the ion, and *Z* is the charge of the ion. An ion moving in a static magnetic field experiences no change in energy. If the velocity of the ion is perpendicular to the magnetic field as in the non-relativistic case, the motion of the ion is circular such that,

$$\frac{dp_{\perp}}{dt} = p_{\perp}\frac{d\theta}{dt} = p_{\perp}\frac{v}{\rho}$$

where is assumed the other momenta are 0, $d\theta$ is the circular angle through which the ion travels in a time dt, and ρ is the radius of circle of motion, also considered as the bending radius of the dipole magnet as before. It follows that,

$$\frac{dp_{\perp}}{dt} = p_{\perp}\frac{v}{\rho} = ZvB$$

$$\frac{p_{\perp}}{Z} = B\rho$$

15

The above result is equivalent to its non-relativistic counterpart, except that here $p_\perp = \gamma \cdot Mv$ and γ is defined as follows.

$$\gamma \equiv \frac{1}{\sqrt{1 - \frac{v^2}{c^2}}}$$

For the beam velocities in this experiment $\gamma \approx 1.11$, so the non-relativistic result for the magnetic separator equation is within 11% of the actual result. However, the non-relativistic version of this equation is just as useful in the sense that it shows that the real power of the magnetic separation technique is that it separates the different ions in the cocktail beam with respect to their M/Z ratios.

While the magnetic separation technique is effective in filtering out many of the contaminate fragments in the cocktail beam, including the left-over primary beam, further separation is needed because isotopes of other elements often have identical or similar M/Z ratios to the exotic beam of interest. Therefore, the cocktail beam is filtered further with the energy loss separation technique. In this technique, the cocktail beam is passed through a block of material, often aluminum, referred to as the "wedge". As the ion passes through the wedge, it is subject to energy loss according to the relativistic Bethe-Bloch formula [20]:

$$-\frac{dE}{dx} = \frac{4\pi Z^2 e^4}{Mv^2} NQ \left[\log \frac{2Mv^2}{I} - \log\left(1 - \beta^2\right) - \beta^2 \right]$$

where E, M, Z, and v refer to the energy, mass, charge and velocity, respectively, of a particular ion in the cocktail beam, $\beta = v/c$, x is the thickness of the wedge and N, Q, and I are the density, charge and mean atomic excitation of the wedge, respectively. If the fragments in the cocktail beam all have the same velocity v, then the energy loss of the different fragments after passing through the wedge is proportional to Z^2 [20]. Thus, the remaining components of the cocktail beam are separated with respect to energy and velocity. The wedge itself does not filter out any of the contaminate fragments. However, now that the components of the cocktail beam are separated with respect to velocity, the magnetic separation technique can be applied a second time to 1) select the magnetic rigidity that allows the exotic beam of interest to pass through the magnet while other

16

fragments are filtered out and 2) to filter out other contaminate fragments that were created from reactions of the cocktail beam with the wedge.

The combination of the two techniques described above filters most of the contaminate fragments out of the cocktail beam containing the exotic beam, once the proper magnetic rigidity and wedge combinations are chosen. A final filtering for the remaining contaminants of the cocktail beam involves the position of beam slits at the end of A1900. This technique again takes advantage of the magnetic separation technique, except this time the position of the beam of interest in the beamline is taken into consideration. If the components of the cocktail beam have similar M/Z ratios and are separated slightly with respect to velocity, then they are separated by position in the beamline after the final dipole bending magnet. By selecting the proper separation of the beam slits and the proper position of the slits at the end of the A1900, the contaminant fragments are further filtered from the cocktail beam. As a result, fairly pure beams of exotic nuclei can be obtained for experiments. One drawback of this technique is that in the attempt to block the contaminant beams, the beam of interest may also be attenuated. Thus, some experiments accept some contaminants in the cocktail beam in order to get a higher rate for the exotic beam. These contaminants are acceptable as long as they have slightly different kinetic energies from the beam of interest, and thus slightly different velocities. Since the cocktail beams are produced at relatively low rates, the time of flight of each beam ion can be measured event by event. This allows a separation of the events associated with each component of the cocktail beam in the experimental data, provided there are only a few types of fragments in the beam. The separation of the components of the final cocktail beam used in the experiment with respect to time of flight is discussed in detail in section 3.

For experiment 02010, the ^{40}S cocktail beam was produced by setting the rigidity of the first two dipoles of the A1900 to 4.0042 T·m. The resulting cocktail beam was then passed through an aluminum wedge 441.406 mg/cm^2 thick. After the wedge, the cocktail beam was passed through the last two dipoles of the A1900 with the magnetic rigidity set to 3.7219 T·m. Finally, at the end of the A1900, the separation of the beamline slits were reduced such that the acceptance of the A1900 with respect to the beam momentum Mv/Z was $\pm 1\%$. This produced a cocktail beam containing mostly ^{40}S ions with a kinetic

energy of 99.3 MeV/nucleon and with some contamination from ^{42}Cl ions. The ^{42}S cocktail beam was produced with the same setup of the A1900 fragment separator, except in this case the magnetic rigidity of the first two dipoles was set to 4.2082 T·m and the magnetic rigidity of the last two dipoles was set to 3.9276 T·m. This produced a cocktail beam containing ^{42}S ions with a kinetic energy of 99.8 MeV/nucleon and with contamination from ^{44}Cl. Details about the ^{40}S and ^{42}S cocktail beams and the ^{48}Ca primary beam can be found in table I.1.

TABLE I.1. Information about the beams used in the experiment.

Beam	^{48}Ca	^{40}S	^{42}S
Incident Energy (MeV/nucleon)	99.3	99.3	99.8
Avg. mid-target E_{beam} (MeV/nucleon)	93.1	92.4	93.3
Avg. Intensity (s^{-1})	$7.8*10^4$	$7.8*10^4$	$1.7*10^4$
Incoming beam purity (%)	100	84.5	57.6
Main beam contaminant	none	^{42}Cl	^{44}Cl

C. Detector Setup Overview

After being produced in the A1900 fragment separator the ^{48}Ca primary beam and the ^{40}S and ^{42}S exotic beams were transported to the S800 spectrograph where they bombarded a liquid deuterium target. The reactions of the beams with the target were identified with the analyzing magnets and focal plane detector system of the S800 spectrograph. Gamma decays in coincidence with events from the reactions detected in the S800 focal plane were detected with SeGA (Segmented Germanium Array). Detailed explanations of the setup of the detectors in the S800 spectrograph and SeGA, and the liquid deuterium target are given in the following paragraphs.

The S800 Spectrograph (shown in figure I.6) consists of two major sections: the analysis line and the spectrograph. The total length of the spectrograph is 40 m. The analysis line, which refers to the section of the spectrograph before the target, contains beamline elements for tuning onto the reaction target. The analysis line also is used to set the beam optics mode for the spectrograph. The two most common beam optics modes used in experiments are the dispersion matched and focused modes [21]. In the dispersion-matched mode, the beam is tuned such that it is achromatic throughout the

18

entire system, which means that the momentum spread of the beam at the entrance of the spectrograph is canceled at the focal plane [21]. This mode allows the highest possible resolution for momentum distributions, although the momentum acceptance of the beam is limited to $\pm 0.5\%$. However, a dispersed, achromatic beam requires a large diameter reaction target (about 10cm) that was not available for this experiment. In focused mode, the beam is focused into a beam spot at the target and is dispersed with respect to momentum. In this mode, smaller diameter targets can be used and the spectrograph has slightly more acceptance ($\pm 2\%$) in the analysis line, allowing for more intense beams. However, in this mode the beam is chromatic at the S800 focal plane, and due to this the intrinsic momentum width of the beam is folded with any momentum change induced by the target. Thus, the beam momentum must be corrected for in order to get the best momentum resolution for momentum distributions.

The analysis line contains, in addition to the beam tuning elements, detectors for monitoring the beam rate, time of flight and tracking of the beam. The signal that starts the time of flight measurement is generated by thin plastic scintillator detectors that are positioned such that the beam passes through them. The extended focal plane scintillator (XFP) is located at the end of the A1900 fragment separator and the object scintillator (OBJ) is located in the object box at the entrance of the S800 spectrograph. Both scintillators were used in the experiment for beam rate monitoring and for generating time of flight start signals for the incoming beam. The difference in time of flight measurements started at the two different scintillators was used to separate the components of the cocktail beam with respect to mass. Also, the time of flight was used in the identification of the mass of the reaction products. Assuming a beam velocity of 0.43**c**, a typical time of flight for a beam ion through the spectrometer is around $310 \pm 1 \, \text{ns}$. The resolution of the time of flight improves to $\pm 0.1 \, \text{ns}$ as the number of events in the S800 focal plane detectors decrease.

About halfway through the S800 analysis line, the incoming beam encounters two Tracking Parallel Plate Avalanche Counters (TPPACs). The TPPACs, as the name implies, track the trajectory of the incoming beam particles by measuring the position and angle of the particles. With this information, an optics calculation can be performed that relates the trajectory of the beam at the TPPACs to the trajectory of the beam at the

target. This optics calculation is necessary for the measurement of momentum distributions in the S800 focal plane. In focus mode, the measurement of the beam particle's trajectory angle through the two TPPACs is related to the momentum spread of the incoming beam. This measurement of the angle, called the intermediate image angle, is used to correct for this intrinsic beam momentum width in the momentum distributions at the S800 focal plane.
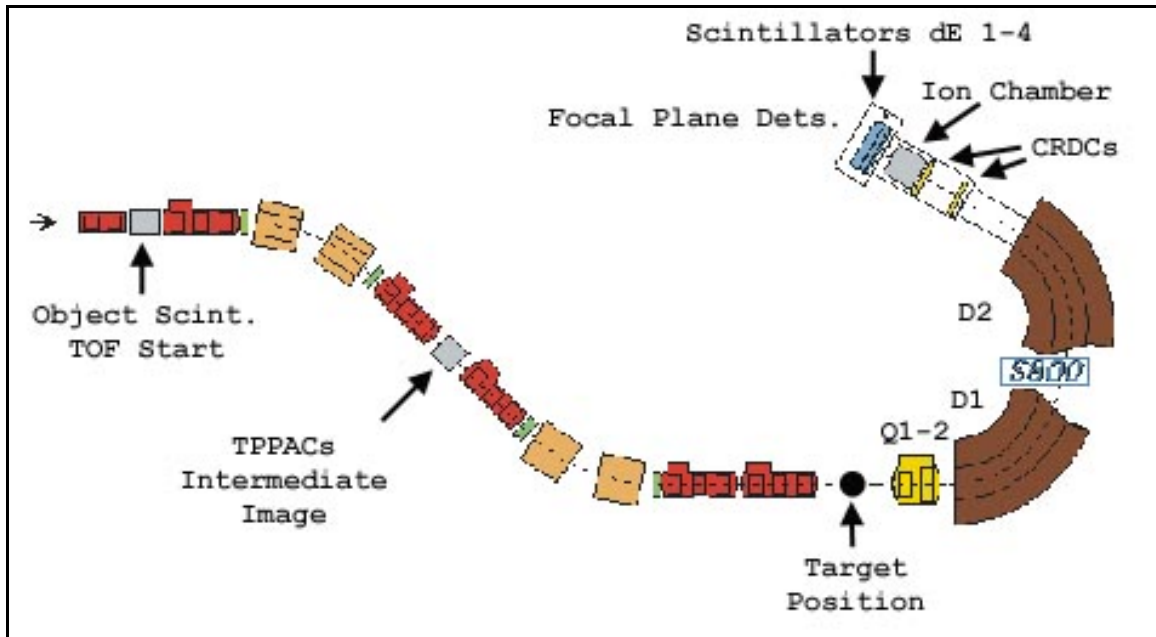
Figure I.6: Setup of the S800 spectrograph. The liquid deuterium target and the SeGA array are placed at the target position.

The TPPACs can also provide time of flight "stop" signals for use in separating the mass of different incoming beam components. While this was not the primary method employed in the analysis of the data, this method can serve as a check to make sure the time of flight gating on the incoming beam particles is correct. This is discussed in detail in the analysis section (section III.F).

At the end of the analysis line, the beam encounters the reaction target. The target for the experiment was the RIKEN liquid hydrogen target [18], filled with liquid deuterium. The target consisted of a cylindrical cell 30 mm in diameter by 9 mm long. The liquid deuterium was contained by two thin aluminum windows that were both about 0.2 mm thick. The aluminum entrance window for the target cell had an areal density of 56.2 mg/cm^2 and the aluminum exit window had an areal density of 57.2 mg/cm^2.

Experimental runs on the empty target cell showed that the cross sections for reactions in the aluminum were negligible. The target was filled with liquid deuterium to a pressure of 1100 hPa (1100 mbar), producing a target 11.2 mm thick. Assuming the density of liquid deuterium is 0.169 g/cm^3, the areal density of the target was 190 ± 2 mg/cm^2. Small pressure drifts observed during the experiment resulted in thickness fluctuations of $\pm 1\%$. These thickness changes did not have a significant effect on the measured cross sections in the experiment compared with other sources of error to be discussed later.
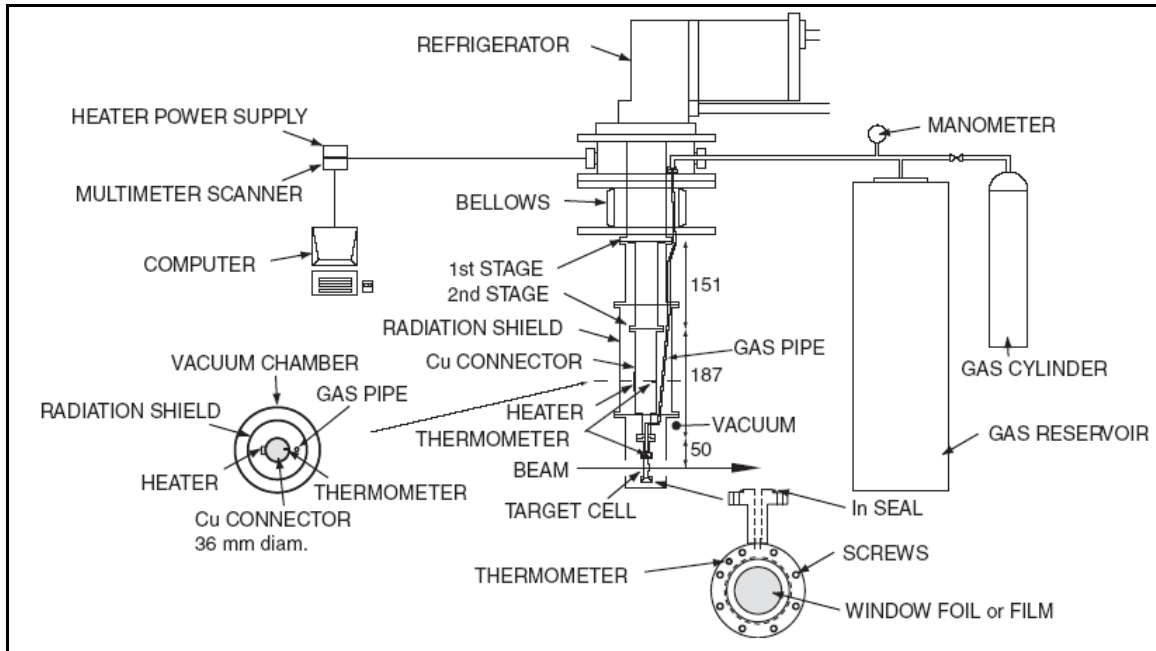
Figure I.7: Schematic view of the liquid hydrogen target taken from [18].

Mounted around the reaction target and outside of the beamline was SeGA (Segmented Germanium Array). The Segmented Germanium Array (SeGA) consists of 16 32-fold segmented high-purity Ge detectors [22] arranged in two rings with central angles of 90° and 37° relative to the beam axis. For this experiment, the 90° ring consisted of nine individual detectors and was positioned perpendicular to the target. The 37° degree ring consisted of seven detectors and was positioned behind the target. In the experiments, the beam particles and their reaction products were traveling at around 0.44c, or a gamma factor of about $\gamma \approx 1.11$. The segmentation of these detectors, and the geometry of the setup, allowed for an accurate event-by-event Doppler reconstruction of the γ-rays emitted in flight by the products of the reactions. The results of the Doppler reconstruction for the reaction $d({}^{48}Ca, {}^{47}Ca + \gamma)X$ are shown in figure I.8. The detection of

21

the γ-rays served as a way to determine which excited states in the reaction products were being populated, and helped to decipher the level schemes of previously unmeasured nuclei. In addition, the γ-rays provided a check for the reaction product identification in the S800 spectrograph.
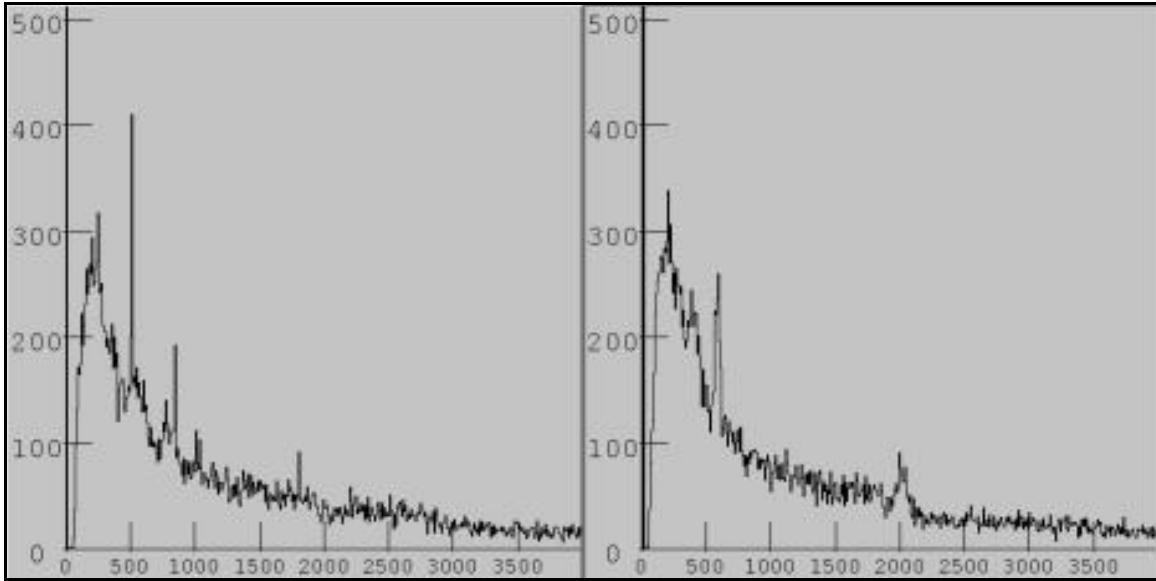
Figure I.8: Doppler reconstruction example showing gamma rays detected from the reaction $d(^{48}Ca,^{47}Ca+\gamma)X$ (counts vs. energy in keV). The left panel shows the gamma ray spectrum from the complete SeGA array before the Doppler reconstruction. Note the large peak at 511 keV from e^+-e^- annihilation. The right panel shows the gamma ray spectrum after the Doppler reconstruction. Note that the peak at 511 keV has disappeared and gamma ray transitions from ^{47}Ca at 570 keV and 2 MeV are now visible.

After the target, the beam passes into the spectrograph part of the S800. The spectrograph consists of two dipole magnets that are set to the magnetic rigidity of the reaction product of interest. The momentum acceptance of these magnets is much larger than that of the analysis line ($\pm 6\%$), and the spectrograph has a large lab angular acceptance of $7°$ in the dispersive plane and $10°$ in the non-dispersive plane. At intermediate beam energies, heavy-ion beams such as those used in this experiment, are forward focused by the kinematics of the scattering of a heavy projectile on a light target. Thus, the entire angular distribution from $0°$ to $180°$ in the center of mass frame can be measured for a given reaction because all the reaction angles are focused into about $\pm 3°$ around the central beam axis. This forward focusing allows for inclusive (total) cross section measurements for given reactions without changing the angle of the spectrograph
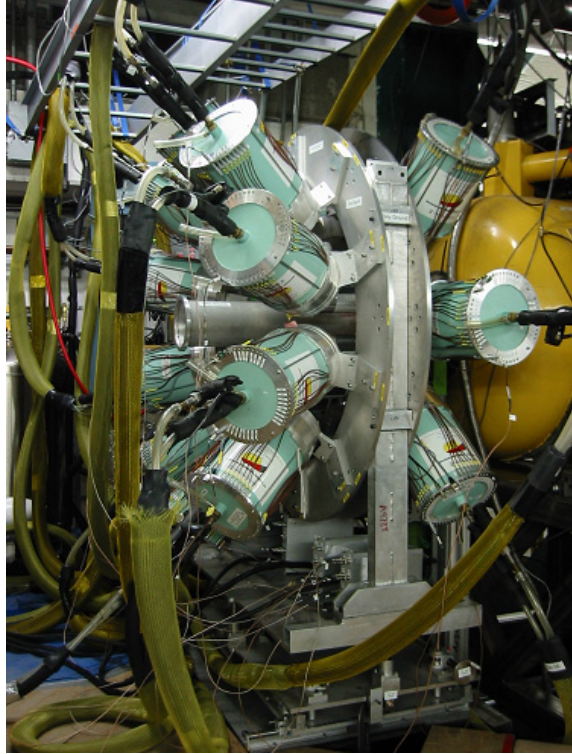
Figure I.9: Picture showing the Sega Array setup in front of Q1 and Q2 of the S800. Liquid deuterium target is not shown.

with respect to the target. It also allows the detection of the products of several different reactions at once, provided the magnetic rigidity of those products is similar to the magnetic rigidity of the product of interest.

As in the A1900, the S800 spectrograph dipole magnets make use of the magnetic separation technique in order to separate the reaction products of interest from other reactions that occur in the target and to aid in the identification of the reaction products. From the A1900 section, the magnetic separation technique equation is,

$$\frac{M}{Z}v = B\rho$$

where the quantity "$B\rho$" defines the magnetic rigidity and is a constant for a given setup. Again, the non-relativistic version of the equation is referred to here because the gamma factor is low ($\gamma \approx 1.11$) and the result is more transparent. Assuming that the incoming beam particles have the same velocity before interacting with the target, then the dipole magnets only allow reaction products with the proper *M/Z* ratio to pass through them and be detected by the focal plane detectors. This assumption works well as long as the "*Z*" of

the reaction products of interest are not too much different from that of the incoming beam. In cases where many nucleons are removed from the incoming beam, such as in heavy-ion fragmentation measurements, the energy-loss of the reaction product in the target must be taken into account when determining the proper magnetic rigidity of the spectrograph dipole magnets.

The reaction products that have the proper magnetic rigidity are finally detected and identified by the focal plane detectors [23]. The focal plane consists of two CRDC detectors for position and angular trajectory measurements, an ionization chamber for measuring the energy loss of the reaction products as they pass through it, and four plastic scintillator detectors to provide additional energy loss information as well as the final "stop" signal for the time of flight measurements. These detectors allow the unambiguous identification of the reaction products in the experiment.
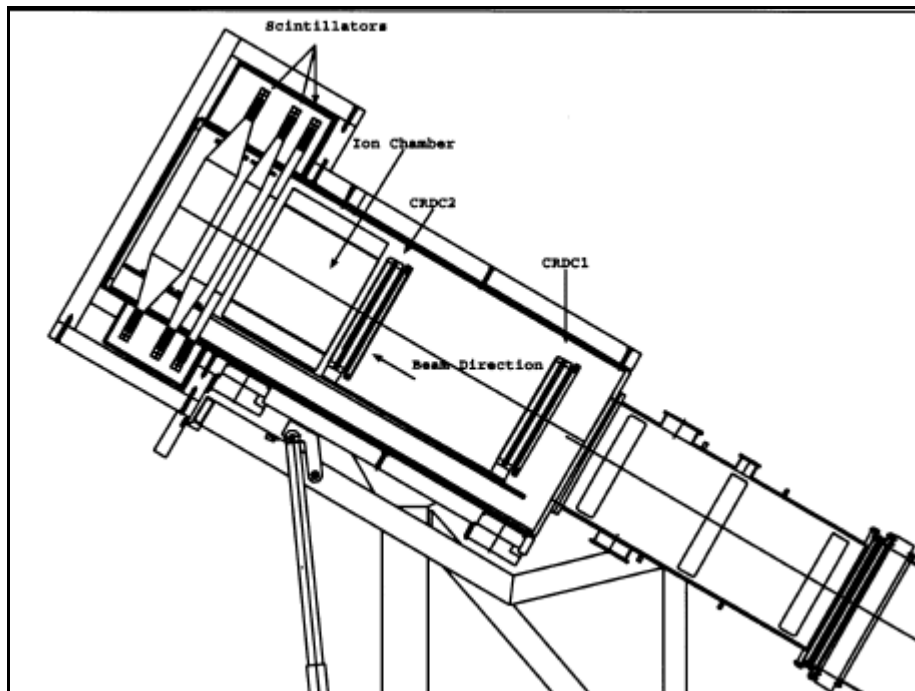
Figure I.10: A close up of the S800 focal plane detectors, taken from [23].

The CRDC (Cathode Readout Drift Chamber) detectors measure the position and angle of trajectory of the reaction products at the focal plane. These measurements determine the momentum of the reaction product for the momentum distributions. Also, the position measurement aids in the identification of the reaction product, since particles

with different *M/Z* ratios will have different positions in the focal plane according to the magnetic separation technique. They are located at the front of the focal plane and are spaced 1m apart. Each CRDC contains 224 individual, equally spaced pads. An event in a pad determines the position of the reaction product particle as it passes through the detector. The CRDC detectors are filled with a gas mixture of 80% CF_4 and 20% isobutene at a pressure of 50 torr. They detect the particles by measuring the drift of the electrons displaced in the gas of each pad by the passing ion. While this method of detection allows a position resolution of about 0.5 mm, the time for each measurement is relatively slow; around 20 μs per event. Due to this, it has been observed that the event rate in experiments should be limited to about 5000 events per second in order to obtain 100% detection efficiency. In this experiment, the combination of relatively high beam rate and thick target produced event rates greater than 5000 events per second, resulting in a loss of efficiency in the CRDC detectors. The efficiency correction for the CRDCs is determined by comparing the number of events in the CRDCs with the number of counts for a given element in the ionization chamber detector. The method for efficiency correction is described in detail in section IV.B.

After passing through the CRDC detectors, the reaction products pass through the ionization chamber. The ionization chamber is also a gas detector that measures the energy loss of the ions as they pass through it. Ions with higher charge "Z" lose more energy as they pass through this detector than ions with lower charge. Thus, with this detector, the reaction products are separated with respect to charge. Assuming that all the reaction products are fully stripped of their electrons and their charge only depends on their proton number, then the energy loss of the ions as they pass through the ionization chamber uniquely identifies each element from the reaction. Further separation of each element group into individual isotopes is obtained from TOF and position measurements in the focal plane.

Finally, the reaction products encounter four large plastic scintillator detectors immediately behind the ionization chamber, labeled E1 though E4. These detectors are 3 mm, 5 cm, 10 cm, and 20 cm thick, in that order, behind the ionization chamber. The detectors provide energy loss and/or total energy measurements, as well as the "stop" signal for TOF measurements. In this experiment, only the ion chamber and the first two

scintillator detectors were used to identify the elemental charge "Z' by measuring the energy loss of the reaction products. The energy resolution of the scintillator detectors was not as good as the ionization chamber, but comparing the energy loss in the different detectors allows additional separation between elements. This will be shown in detail in the analysis section. Also, the TOF for the reaction products was measured from the XFP or OBJ scintillator to the E2 scintillator. This particular TOF measurement is defined in the software to record the TOF of a particle only when both CRDCs detect a given particle. The advantage of this measurement is that it is independent of the efficiency of the TPPACs, making this TOF ideal in determining mass of the particle in software gating schemes for measuring the cross section.

D. Experiment Details

The experiment was conducted from November 13 to November 17, 2003. The cross sections for four different single-particle transfer reactions were measured separately with four different magnetic rigidity settings of the S800 spectrograph. The types of reactions measured, the beam time for determining each cross section, and the S800 spectrograph magnetic rigidity settings for the dipole magnets after the reaction target are given in table I.2.

TABLE I.2. S800 spectrograph settings for the various transfer reactions

Transfer Reaction	Beam Time	S800 $B\rho$
$d(^{48}Ca,^{49}Sc)n$	12 hrs.	3.0995
$d(^{48}Ca,^{49}Ca)p$	3 hrs.	3.3467
$d(^{40}S,^{41}Cl)n$	12 hrs.	3.3660
$d(^{42}S,^{43}Cl)n$	12 hrs.	3.4423

E. Data Analysis – Calibrations

The data from NSCL experiment 02010 was analyzed within the framework of the software program SpecTCL, version 1.1. The software codes for both the S800 spectrograph and SeGA were integrated together within SpecTCL to allow measurements of both the reaction products in the S800 and the in-flight gamma decays detected in coincidence with the reaction products.

Both the S800 spectrograph and SeGA have a large number of individual detector channels. For example, each CRDC detector has 224 individual pads, and the signal gain for each pad must be calibrated for each experiment. Due to the setup of the S800 focal plane, it is difficult to check the signal gain of the pads for each experiment, and the gain matching of each pad may change during the experiment if different particles are observed. Thus, the signal amplifier gains of the CRDC pads are set to the same values in the hardware, and then the signal gains are later adjusted in the software so that the pads are gain matched. Similar software corrections to the energy calibration of the germanium detectors in SeGA are also possible within SpecTCL. The software calibrations for the detectors used in the analysis of this experiment are described in the following paragraphs.

1. S800 CRDC Calibrations

Figure I.11 shows a summary of the signal pulse heights in the pads of CRDC1 before gain matching for the $d(^{48}Ca,^{49}Sc)n$ data runs, gated on the calcium reaction products. The x-axis shows the pad number, 0-223, and the y-axis shows the number of events associated with a given signal pulse height. The events with low pulse height are considered to be noise and are discarded by including the pre-determined pad pedestals in the variable list. The pedestal settings for each pad were provided by the S800 support staff. The pulse height associated with the detection of a calcium particle for each pad (in general, higher than the noise on spectrum) is highlighted in green on the spectrum in figure I.11a and is estimated, in general, as the pulse height with the second highest number of events in each pad. The pulse heights for each pad must be gain matched in order to obtain the best resolution for the position of the reaction products in the focal plane, thereby giving the cleanest particle identification. The CRDC detectors in the S800 were gain matched in the analysis software with the following procedure. First, a software gate was created on the energy loss in the ionization chamber associated with an individual element, in this case calcium. This gate was then applied to spectra showing the pulse height vs. number of events for each CRDC pad. Assuming that particles with the same charge "Z" should produce the same pulse height in each pad, the SpecTCL S800 variable s800.fp.crdcX.pad.slope.N (where "X" refers to the CRDC number and "N" refers to the pad) was adjusted such that the pulse height associated with the peak in

the pulse height distribution associated with the calcium events were matched to the same pulse height. A spectrum for a typical CRDC pad before and after the gain adjustment is shown in figure I.12. The result of the pulse height matching of the CRDC pads is shown in figure I.11b. Note that whereas before gain adjustment the calcium events had varying pulse heights with respect to each pad, after the adjustment the pulse heights in each pad appear well matched.

Another noticeable feature in the summary of the CRDC pads are gaps that appear between different sections of the pads. These gaps are shown in figure I.11 by the pads that appear to have very few events with respect to the pads around it. This identifies pads within the CRDC that were not functioning properly during the experiment. These "badpads" can be identified within the software and left out of the calculation of the particle position in the focal plane by assigning the badpad number to the variable s800.fp.crdcX.calc.badpad.Y, where "Y" denotes up to 20 possible badpads. Badpads often lead to confusing features in the particle position measurements. For example,
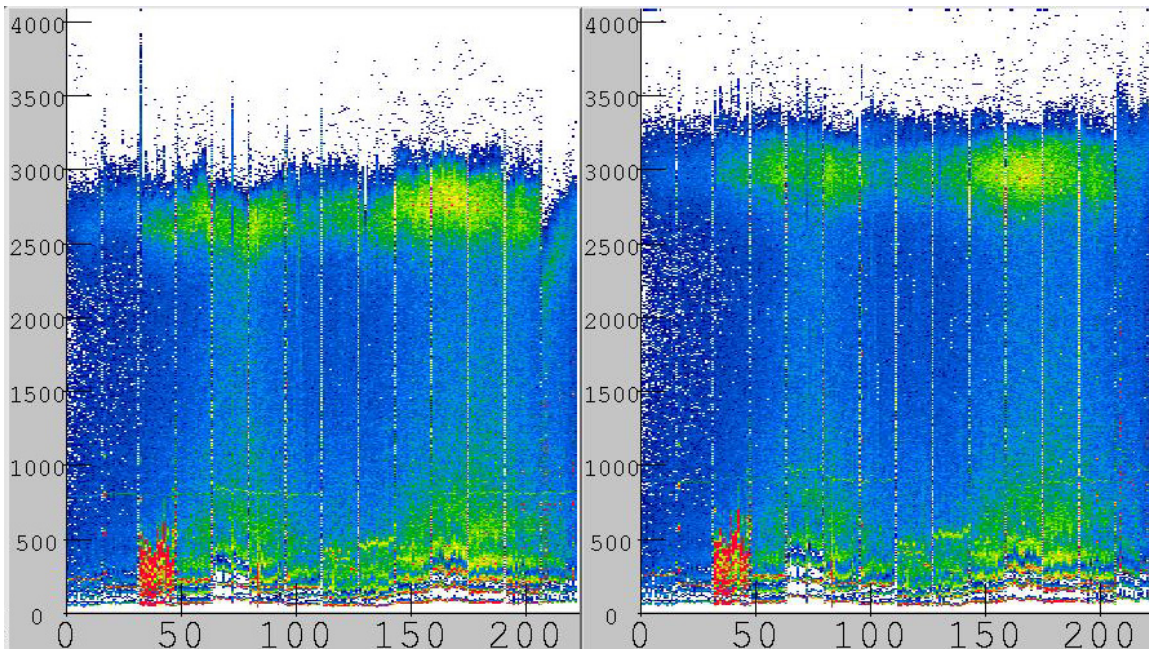
Figures I.11a and I.11b: CRDC1 pad summary spectrum before (left panel) and after gain matching (right panel). Pulses from calcium events are shown by the upper green areas. "Badpads" are shown as the white gaps between groups of pads.
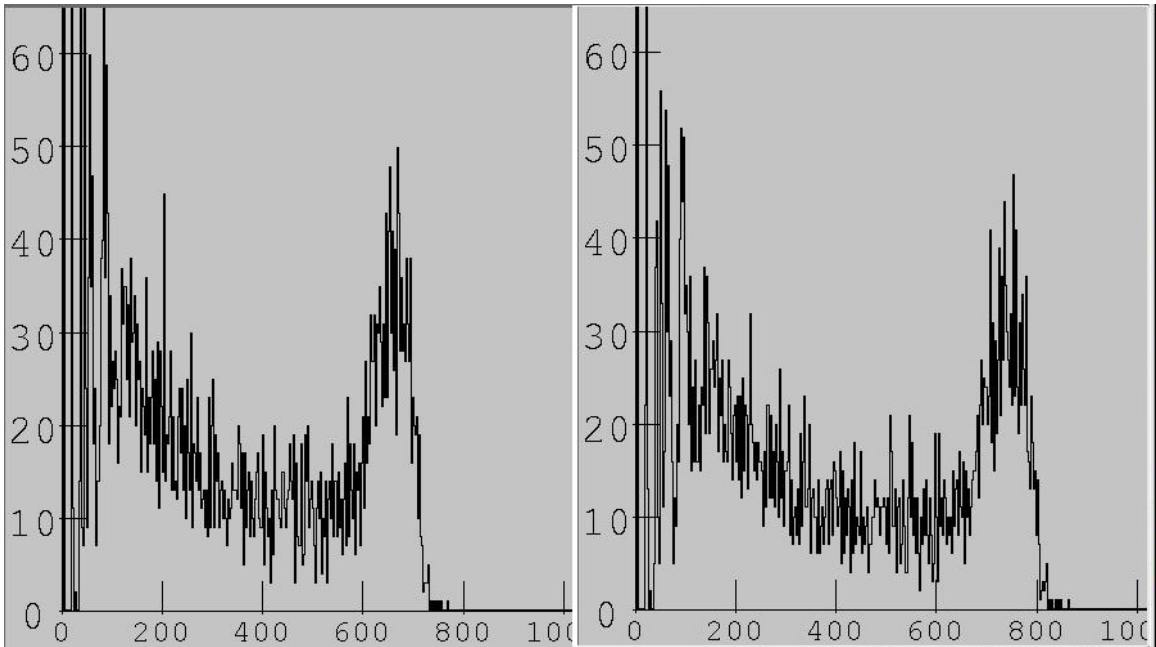
Figures I.12a and I.12b: Individial pad pulse spectrum for CRDC pad #86 before and after gain matching. Note the position of the peak has increased along the X-axis to match the pad with the other pads.

badpads in CRDC1 led to confusing peaks in the position measurement for $d(^{48}Ca,^{47}Ca)X$. Assigning CRDC1 pads such as 31 and 32 as badpads and properly gain matching the other pads created a much smoother position spectrum as shown in figure I.13. In all, CRDC1 had 17 badpads and CRDC2 had 19 badpads. Once the CRDC pad pulse height gains are matched and the badpads are defined in the software, the method of determining the position of the particle from the charge distribution left by the track of the particle as it passed through the detector can be changed to the Gaussian fit method [23]. This method is superior to the default position determination method given by the center of gravity of several pads around peak of the charge distribution in the detector, since the Gaussian method has higher position resolution. The center of gravity method has the advantage that it does not require the CRDC pad pulse heights to be matched in order to determine the position of the particle and thus is useful during the online analysis of the experimental data despite the lower position resolution. The analysis of the position data from the CRDCs presented in this report was carried out with the Gaussian fit method.
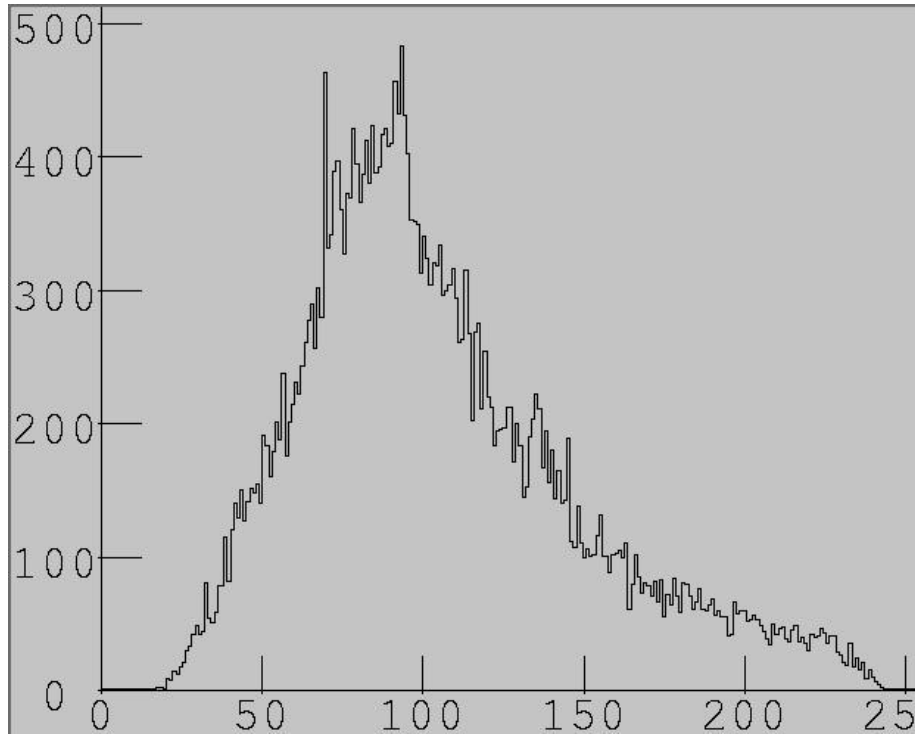
Figure I.13: Calibrated Counts vs. CRDC1 x-position spectrum for d(^{48}Ca,^{47}Ca)X.

In addition to the CRDC detector calibrations, typically the particle time of flight (TOF) must also be calibrated in the software in order to obtain the best mass resolution for the incoming beam particles and the reaction products detected in the S800 focal plane. Figure I.14 shows the energy loss in the ionization chamber versus the TOF from the object scintillator to the E2 scintillator (OBJE2). While the particle groups are well separated with respect to "Z" in this spectrum, the individual isotopes are indistinguishable. This is due to path length differences for the reaction products as they exit the target and travel to the focal plane. For example, although the magnetic rigidity is constant for two particles of the same isotope, the time of flight for each particle will different for particles exiting from the target at different positions. The difference in the path length for different isotopes of the same element is best observed by measuring the focal plane angle for the particle between CRDC1 and CRDC2, also known as the angle in the focal plane (AFP). The path length difference effect on the TOF measurement is corrected by adjusting the S800 variable s800.tof.obje2Correction such that the particle mass groups in the AFP spectrum (s800.track.afp) have the same TOF. A sample

spectrum showing the AFP vs. TOF OBJE2 before and after the TOF correction is shown in figure I.15. The OBJE2 TOF corrections for the data sets are given in table I.3.
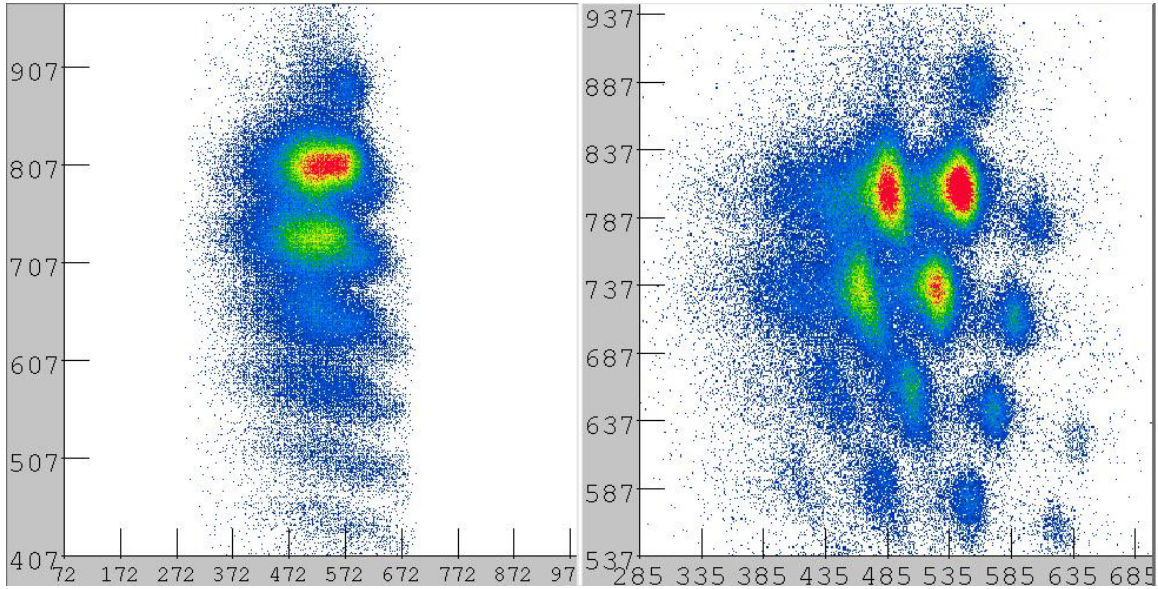
Figures I.14a and I.14b: Energy loss vs. TOF OBJE2 spectra before (left panel) and after (right panel) TOF correction. Note that the elements are separated into groups of isotopes in the right panel.
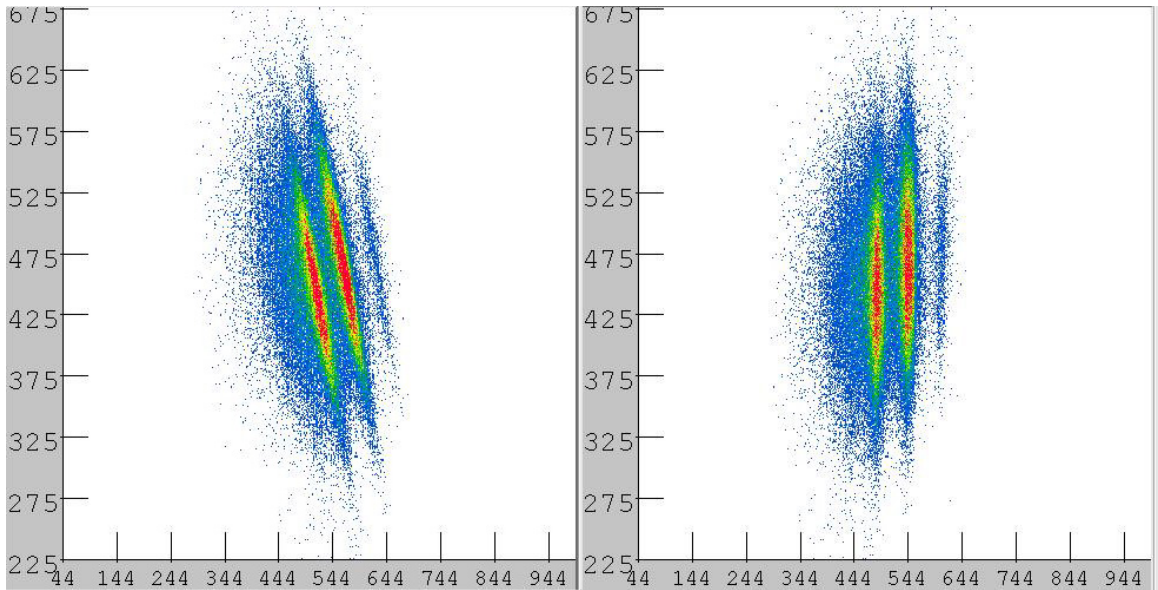
Figures I.15a and I.15b: AFP vs. TOF OBJE2 spectrum for ^{48}Ca+d, gated on calcium events. The left panel shows the spectrum before the TOF correction and the right panel shows the spectrum after the TOF correction.

TABLE I.3: OBJE2 Time of Flight Corrections for the various transfer reactions

Transfer Reaction	S800 $B\rho$	OBJE2 TOF Correction
$d(^{48}Ca,^{49}Sc)n$	3.0995	825
$d(^{48}Ca,^{49}Ca)p$	3.3467	825
$d(^{40}S,^{41}Cl)n$	3.3660	825
$d(^{42}S,^{43}Cl)n$	3.4423	825

2. SeGA Calibrations

SeGA has several important software calibrations that are necessary in order to accurately determine the energy of a gamma ray emitted in-flight by a reaction product and the efficiency of detection for a gamma ray of a given energy. The energy calibration of the individual detectors in SeGA, the calibration of the Doppler correction with respect to the velocity of the beam and the target position with respect to the array, and the gamma ray detection efficiency calibrations are described in the following paragraphs.

The absolute energy calibration for the germanium detectors in SeGA was determined by placing ^{152}Eu and ^{56}Co gamma ray sources in the beamline at the target position while the target was removed. Data were recorded for these calibration sources and others in one hour runs before and after the experiment. The energies of the gamma rays emitted by these sources as they beta and electron capture decay are well known. The principal gamma rays from the decay of ^{152}Eu range from 121 keV to 1408 keV [24] and are most useful in determining the calibration of the low energy gamma rays detected by SeGA. The gamma rays from the electron capture decay of ^{56}Co range from 846 keV to 4458 keV [24], although in practice the low count and low detection efficiency for the gamma rays above 3548 keV limit the effective energy calibration range for the two sources to 121 keV to 3500 keV. Gamma ray energies below 121 keV can be calibrated with data runs measuring the gamma rays from the electron capture decay of a ^{133}Ba calibration source down to 80 keV. However, this source was not considered in the energy calibration because the germanium detector thresholds were set to 100 ± 10 keV, vetoing most of the gamma rays below 121 keV.

To calibrate the energy spectrum of each detector in the software, a spectrum of the data from the [152]Eu and [56]Co calibration sources was generated for each germanium detector. The known energy peaks were then fitted individually assuming a Gaussian distribution with the program *gf3* [25], and the channel number of the centroid of each peak was recorded. The channel number of the centroid was plotted versus the known energy of each peak, and a least squares fit was made to the data to determine the conversion from channel number to gamma ray energy in keV for each detector. The conversion from channel number to gamma ray is linear in general, although a small second order correction to this fit is needed in order to obtain the best reproduction of the original calibration peak energies. The need for this second order correction is believed to arise from the Ortec 413A ADCs used in the data acquisition electronics for SeGA [26]. With the second order correction, the error in the centroid of a given calibration peak is within 0.5 keV of the actual energy of the gamma ray for all detectors. The energy calibrations of the germanium detectors were checked before and after the experiment, and it was noted that the energy calibration of the detectors did not change significantly during the experiment.

Each germanium detector in SeGA is segmented into 32 individual segments. In principle, each segment can act as its own detector and measure the energies of the gamma rays it detects. The energy and position measurement of the gamma rays detected in the detector segments are important in determining the Doppler correction of the gamma ray. Therefore, in principle, the individual segments should also be calibrated with respect to energy. In practice, this can be a tedious task since there are 32 x 16 = 512 total segments to calibrate for the entire array. However, since the germanium in the segments of a given detector are all part of the same germanium crystal, it is reasonable to suggest that the energy calibration for each segment should be similar to the energy calibration for the entire detector. This assumption has been tested by Hu et al. [27]. As a result, a program for determining the energy calibration for the individual segments of each detector from the energy calibration of the central conductors of each detector has been integrated into the data analysis software. This program must be run each time new calibrations for the central conductors of the germanium detectors are fitted such that the individual segments are also calibrated.

3. Calibration of Software for Doppler Corrections

The data analysis software in SpecTCL also allows event-by-event Doppler reconstruction of gamma ray spectra detected by SeGA. In figure I.16a, the raw particle-gamma coincidence data from the reaction $d(^{42}S, ^{40}S + \gamma)X$ has broad peaks for strong gamma ray transitions and weak gamma ray transitions are indistinguishable from the background. Also, if the gamma rays detected in SeGA are separated into the rings of detectors at $90°$ and $37°$ with respect to the target, it appears that there is one strong gamma ray transition present only in the $90°$ ring and a separate gamma ray transition present only in the $37°$ ring. These two seemingly separate peaks are actually from the same transition; the 904 keV ($2^+ \to 0^+$) in ^{40}S. The difference in energy depending on the position of the detector ring with respect to the target is due to the semi-relativistic velocity of the reaction product with respect to the lab frame. The gamma rays are emitted from the reaction product nuclei in the rest frame of the reaction products, whereas the gamma rays are detected by SeGA in the lab frame. Thus, the energy of the gamma rays detected by SeGA must be boosted so that the true gamma ray spectra in the rest frame of the reaction product can be observed.

The Doppler correction software in SpecTCL requires four pieces of information in order to properly correct the gamma ray spectra. First, the velocity of the reaction product particle when it emits its gamma ray must be considered. With the assumptions that the reaction between the beam and the target happens at the middle of the target (on the average), and that the reaction product gamma decays instantaneously after its creation ($T_{1/2} < 1$ fs), then a first guess for the reaction product velocity is the velocity derived from the particle's mid-target velocity. Further, if the Q-value for a given reaction is small compared to the kinetic energy of the beam, then the mid-target velocity of the reaction products will not be significantly different than the mid-target velocity of the beam. The Q-values for the reactions considered in this experiment are typically between -10 and $+10$ MeV, whereas the mid-target kinetic energy of the beams is around 90 MeV/nucleon (see table I.1). Thus, the mid-target velocity of the reaction product, to first approximation, is the same as the mid-target velocity of the beam. The mid-target velocities of the beams in the experiment, as calculated by the program LISE [28], are

shown in table I.4. Measurements for the front aluminum window thickness and ½ the liquid deuterium target thickness are taken from section III.C.

TABLE I.4: Beam Velocities for Doppler Corrections for each data set

$$c \equiv speed\ of\ light = 3 \cdot 10^8\ m/s$$

Transfer Reaction Data Set	Mid-target beam velocity	Optimum velocity used in Analysis
$d(^{48}Ca,^{49}Sc)n$	0.417**c**	0.408**c**
$d(^{48}Ca,^{49}Ca)p$	0.417**c**	0.408**c**
$d(^{40}S,^{41}Cl)n$	0.415**c**	0.4105**c**
$d(^{42}S,^{43}Cl)n$	0.417**c**	0.4087**c**

The resulting gamma ray spectra taken from the data for $d(^{42}S,^{40}S+\gamma)X$ (assuming $\beta(^{42}S) = 0.417$) are shown in figure I.16b, expanded in the area around the 904 keV ($2_1^+ \rightarrow 0_1^+$) transition. Note that the 511 keV peak from $e^+ - e^-$ annihilation has disappeared because the 511 keV gamma rays were created in the lab frame. Thus, in the Doppler corrected gamma ray spectrum, these gamma rays have been broadened to the extent that they are part of the background. More importantly, the two prominent peaks in figure I.16a for all SeGA detectors have now become one peak, centered at 904 keV. Also, the 1352 keV ($2_2^+ \rightarrow 2_1^+$) transition, which was little more than a small bump on the non-Doppler corrected spectra, is now a strong peak.

However, the velocity calibration of the beam is not quite complete because if the 904 keV transition is viewed with respect to the two detector rings, there is still a slight difference in the measured gamma ray energies. In figure I.16b, the $90°$ ring has the gamma ray at 908 keV and the $37°$ ring has the gamma ray at 899 keV. While this averages out to about 904 keV for the measurement of the entire array, further improvement to the Doppler correction for the beam velocity is possible. The proper beam velocity for the Doppler correction, which results in better energy resolution for the gamma ray detection in SeGA, can be found by adjusting the beam velocity slightly until the gamma ray has the same energy in both the $90°$ and $37°$ detector rings. The
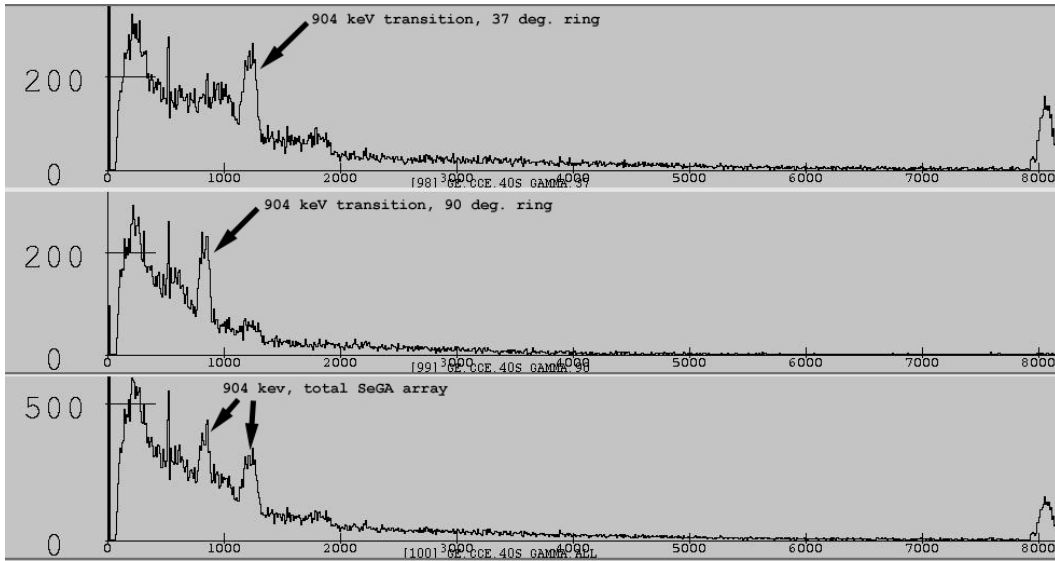
Figure I.16a: Non-Doppler corrected SeGA spectra for $d(^{42}S,^{40}S)X$ reaction.
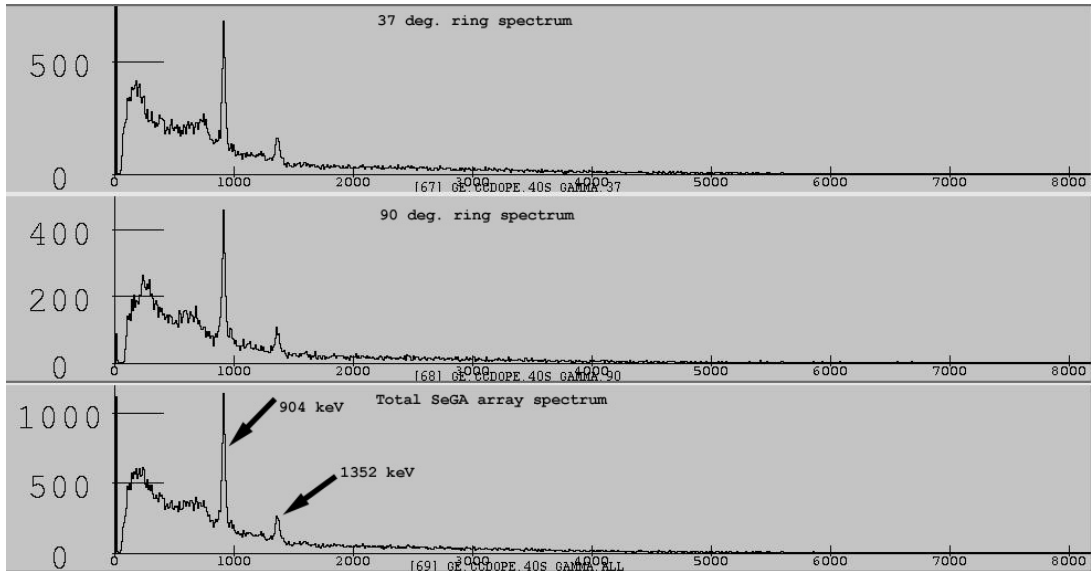
Figure I.16b: Doppler Corrected spectra for $d(^{42}S,^{40}S)X$ with Beta=0.417. Note the alignment of the peaks in the two detector rings.

adjustment of the velocity roughly follows the rule that if $E_\gamma(90°) < E_\gamma(37°)$, then the beam velocity needs to be increased and if $E_\gamma(90°) > E_\gamma(37°)$, then the beam velocity needs to be decreased. Typically, the optimum value for the beam velocity is within 5% of the mid-target beam velocity estimate. The optimum values for the beam velocity used in the analysis of the data for this experiment are given in table I.4.

The Doppler correction of the gamma ray spectra also depends on the position of SeGA with respect to the target position along the beam axis (z-axis). So, even if the

36

energy of a given transition is matched in both the $90°$ and $37°$ detector rings, the gamma ray peak does not appear at the proper energy in the Doppler corrected spectrum unless the target is in the proper z-position with respect to the detector array as defined in the analysis software. The position of each detector in SeGA with respect to the other detectors is accurately measured with surveying instruments. However, the target position is different from the position expected in the software because the target position in the beamline is estimated with a "measuring stick" that has a length the same as the distance from the end of a section of beamline to the center of the $90°$ detector ring. It was found during the analysis of the data that the position of the liquid deuterium target with respect to the beam axis was within $\pm 1.5\,\text{mm}$ of the origin position for SeGA as determined in the analysis software. Thus, the slight adjustment of the target position along the beam axis served only to match the energies of the gamma rays measured in the experiment with the known gamma ray energies determined in previous experiments. The gamma ray energies from the known transitions were taken from β-decay or similar experiments where the energies of the gamma ray transitions were measured to high precision. The energies of other gamma rays in the same data set that were not seen in β-decay measurements were determined assuming that the target position was correct once it had been determined for the known transition in the analysis software. The known transitions used in the analysis of each of the data sets are given in table I.5.

To obtain the best resolution in the Doppler corrected spectra for the rings and the entire detector array, the position of the target in the plane of the rings (x-y axis position) must also be optimized. While the Doppler corrected spectra for each ring may show the gamma ray peak at the proper energy, the energy of the same gamma ray may vary as much as $\pm 20\,\text{keV}$ if the peak is observed in the individual detectors. This variation in the gamma ray energy is particularly evident in the $37°$ detector ring. The optimum position in the x-y plane was determined with a known gamma ray transition in each data set (the same as in the determination of the optimum z-axis position). The energy of the gamma ray as measured in each detector versus the position on the x-axis and the y-axis was plotted and the optimum position on each axis was determined by the position where the peak energies from each detector converged. It was found that the optimum x-axis position was within $\pm 1\,\text{mm}$ of the "0" position defined in the software, whereas the y-axis

TABLE I.5: Optimized Target Positions for Doppler Corrections for each data set

Transfer Reaction Data Set	Target Position (x,y,z) (cm)	Known gamma ray transition for calibration
$d(^{48}Ca,^{49}Sc)n$	0, 0, -0.028	^{46}Ca, ($2_1^+ \rightarrow 0_1^+$), 1346 keV
$d(^{48}Ca,^{49}Ca)p$	0, 0, -0.028	^{46}Ca, ($2_1^+ \rightarrow 0_1^+$), 1346 keV*
$d(^{40}S,^{41}Cl)n$	0.1, 0.55, -0.028	^{38}S, ($2_1^+ \rightarrow 0_1^+$), 1292 keV
$d(^{42}S,^{43}Cl)n$	0, 0.55, 0.12	^{40}S, ($2_1^+ \rightarrow 0_1^+$), 904 keV

*It was assumed for the $d(^{48}Ca,^{49}Ca)p$ runs that since the same beam tune was used, the target position would be the same as it was for the $d(^{48}Ca,^{49}Sc)n$ data set. The above calibration gave the proper energies for known gamma ray transitions in ^{46}K and other nuclei.

varied within ± 0.55 cm of the "0" position. The slight change in the target position with respect to SeGA between data sets is due to the slight changes in the position of the beam spot on the target for the different beams used in the experiment. The $x,y,$ and z positions of the target with respect to SeGA for each data set are given in table I.5.

The parameters given in tables I.4 and I.5 are the parameters that were used in the analysis of the gamma rays in coincidence with the reaction products observed in the S800 focal plane. These parameters give the best energy resolution in the Doppler corrected gamma ray spectra for most energies between 100 keV and ~2500 keV. However, the Doppler correction for SeGA has its limitations. The Doppler correction becomes more difficult when the energy of the gamma ray transition is greater than ~2500 keV because the large amount of energy deposited in the germanium crystal of the detector triggers several detector segments simultaneously. This makes the precise determination of the position where the gamma ray hit the detector more difficult and causes problems for the Doppler correction. Also, high-energy gamma rays are more likely to Compton scatter in the germanium crystal, making a measurement of their total energy impossible with the current data analysis software. The difficulty in detecting high-energy gamma rays was most evident in the attempts to measure the decays of excited states from the $d(^{48}Ca,^{49}Sc)n$ and $d(^{48}Ca,^{49}Ca)p$ reactions, where there are many gamma decays from single particle states with energies above 3000 keV. For reaction products with excited states that decay via gamma rays with energies below 2500 keV,

however, the energy resolution of the gamma ray peak in the Doppler Corrected spectrum for the entire detector array was typically around 30 keV FWHM. The optimum energy resolution for SeGA was limited mainly by the thickness of the liquid deuterium target.

4. SeGA Detection Efficiency

The detection efficiency of SeGA, or the probability that a gamma ray of a given energy is detected by the array, is intrinsically low (around 2% for detection of the 1332 keV gamma ray from ^{60}Co Beta-decay). The efficiency is low for several reasons. First, the coupling of a gamma ray to matter depends on the atomic number "Z" of the detection material, in this case germanium with Z=32. Detectors made of materials with higher "Z", such as NaI detectors (iodine has Z=53) have higher efficiencies, but lower energy resolution than germanium detectors. Another reason for the low detection efficiency of SeGA is that the detector rings do not surround the entire surface area around the target with germanium. Thus, some gamma rays from reactions will miss the detector array entirely. Also, the gamma rays must pass through several objects before they reach the germanium crystal in the detector. For this experiment, the gamma rays travel through the remainder of the target material, the aluminum that forms the outside of the liquid deuterium target chamber, the outer shell of the beamline, the air between the beamline and the germanium detector and the outer shell of the detector that contains the germanium crystal. Any of these objects can scatter the gamma ray before it ever reaches SeGA. Passing through matter on the way to the detector lowers the detection efficiency of low energy gamma rays ($E_\gamma < 1000\,\text{keV}$). Finally, the efficiency changes with respect to gamma ray energy. The maximum detection efficiency for SeGA is for gamma rays around 130 keV and then decreases after that with respect to energy.

F. Data Analysis – Particle Identification and Software Gating

1. Beam Identification

The first step in determining the unique identities of the reaction products in the S800 focal plane was to identify the incoming beam components. This was not difficult for the reactions produced by the ^{48}Ca primary beam since ^{48}Ca ions were the only species present in the beam. However, since both the ^{40}S and ^{42}S cocktails beams

contained contaminants, it was necessary to separate reaction products with respect to the beams that produced them in the analysis.

The compositions of the cocktail beams were measured with separate experimental runs where the magnetic rigidity of the S800 spectrograph was set to detect the elastic scattering of each cocktail beam while accounting for the energy loss of the beam in the liquid deuterium target. The components of the beam were detected in the S800 focal plane, since most beam particles pass through the target without producing reactions. The components of the beam were most easily observed in the data by plotting the energy loss of the beam particle in the S800 ionization chamber detector (ΔE) vs. the time of flight between the Object scintillator and the E2 scintillator (TOF OBJE2). The resulting spectrum is shown in figure I.17a. In this example, the main components of the cocktail beam, mainly ^{40}S and ^{42}Cl, are clearly visible. The ^{40}S beam particles are clearly separated in the data because they have lower energy loss than the ^{42}Cl ions, and they also have a longer TOF since they are at a slightly lower kinetic energy than the ^{42}Cl (note that in figure I.17a, the TOF decreases along the x-axis according to convention). The ^{42}Cl ions are expected to have more kinetic energy than the ^{40}S ions because, according to the magnetic separator equation, if the magnetic rigidity $B\rho$ of the S800 spectrograph is a constant, then ^{42}Cl must travel at faster velocity than ^{40}S because ^{42}Cl has a smaller M/Z ratio than ^{40}S. It follows that since ^{42}Cl travels at a faster velocity, then it has more kinetic energy and a shorter TOF as it travels through the spectrograph. The ^{42}S and ^{44}Cl components of the ^{42}S cocktail beam can also be identified with a similar line of reasoning.

Once the components of the cocktail beam are identified in the S800 focal plane detectors with respect to energy loss and TOF, the next step is to create a software gate on the beam ion of interest, thus identifying the type of beam particle that led to a specific reaction product. However, once the magnetic rigidity of the spectrograph is changed to look for the reaction product of interest, the beam particles are no longer detected in the S800 focal plane. In addition, the reactions of the beam in the target create a wide variety of reaction products, making it difficult to decipher which beam the product came from. There are two different methods for creating a software gate to separate the components of the cocktail beams in the reaction runs. The first method involves using the TPPACs at

the intermediate position in the S800 analysis line as the time of flight "stop" signal for the beam. If one plots the angle between the two TPPACs (the *image theta* angle) of the cocktail beam particles as they pass through the TPPACs vs. the time of flight from the XFP scintillator to the TPPAC detectors, then groups of particles appear in the spectrum associated with the separate components of the cocktail beam. A sample spectrum of this type for the ^{40}S cocktail beam is shown in figure I.17b. One way of identifying the groups of particles is by applying a software gate around the desired beam particles in the ΔE vs. TOF OBJE2 spectrum from figure I.17a to the TPPAC *image theta* vs. TOF XFP spectrum and seeing which particle group appears in the spectrum if the elastic scattering run is scanned. The other way is to note that the TOF relationship between the components of the cocktail beam in the TPPAC *image theta* vs. TOF XFP spectrum is the same as it is in the ΔE vs. TOF OBJE2 spectrum. Thus, for the example in figure I.17b, the left particle group in the spectrum is the ^{40}S since it has a longer TOF.
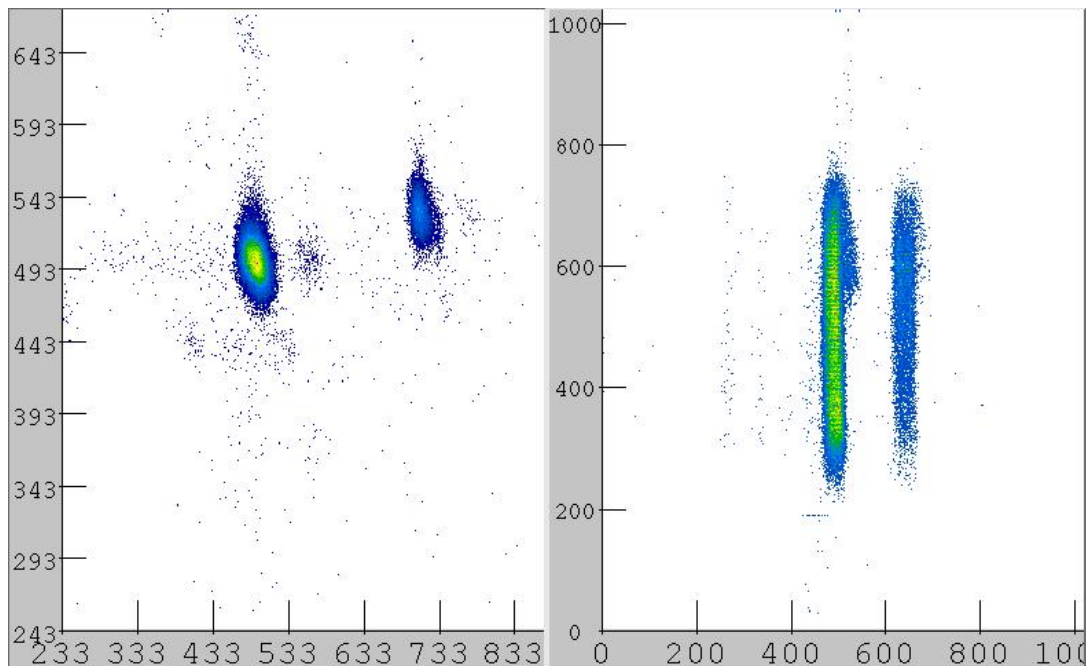
Figures I.17a and I.17b: The left panel shows $\Delta E - ICSUM$ vs. *TOF OBJE2* for the ^{40}S beam elastic scattering run. Events from the ^{40}S beam particles (middle, longer TOF) and ^{42}Cl beam particles (right, shorter TOF) are cleanly separated. The right panel shows *TPPAC image theta* vs. *TOF XFP* for the ^{40}S beam elastic run. The two particle groups have the same relationship with respect to TOF, with the ^{40}S centered in the spectrum.

While the method above has the advantage that the identity of the beam particle is determined before it interacts with the target, the efficiency of this method is limited by

the detection efficiency of the TPPACs. Even though the highest beam rates observed in the experiment ($\sim 10^5$ particles/sec) did not approach the rate limit of the TPPACS (10^6 events per second), there was the problem that the high voltage of the TPPACs randomly shutdown several times during the experiment. Therefore, it was necessary to develop a second method for beam identification that did not involve the TPPACs in order to get accurate measurements of the reaction cross sections.

The beam identification method used in the analysis of the data took advantage of the difference in TOF of the components of the cocktail beams. In the data analysis software, the two TOF measurements that do not involve signals from the TPPACs are the time of flight from the XFP scintillator to the E2 scintillator in the S800 focal plane (TOF XFPE2) and the time of flight from the OBJ scintillator to the E2 scintillator (TOF OBJE2). If the TOF XFPE2 is plotted versus the TOF OBJE2 and the data from the elastic scattering run is scanned, then two main groups of beam particles appear in the spectrum along the diagonal. An example of this spectrum is shown in figure I.18 for the ^{40}S cocktail beam (note again that the TOF decreases along both the *x*-axis and *y*-axis according to convention). The beam particle group with the shorter TOF according to both measurements is the ^{42}Cl and the beam particle group with the longer TOF measurements is the ^{40}S. The final step is to scan an experimental run where reaction products are detected in the S800 focal plane for this spectrum. The particle groups in the TOF XFPE2 vs. TOF OBJE2 spectrum become broader because the reaction products from the two beams have different times of flight. However, the difference in the times of flight for the components of the beam before they react in the target is enough for all of the reaction products detected in the S800 focal plane to have a time of flight that depends on the time of flight of the beam particle involved in the reaction. Thus, the reaction products associated with a particular beam will be separated according to their differing time of flight in the TOF XFPE2 vs. TOF OBJE2 spectrum. As in figure I.17, the group of reaction products with longer TOF according to both measurements was produced from reactions involving the ^{40}S beam, and the group of reaction products with shorter TOFs was produced from ^{42}Cl reactions. To complete the beam identification step of the analysis, a software gate is drawn around the reaction product group of interest and applied to the particle identification spectra described in the following paragraphs.

42
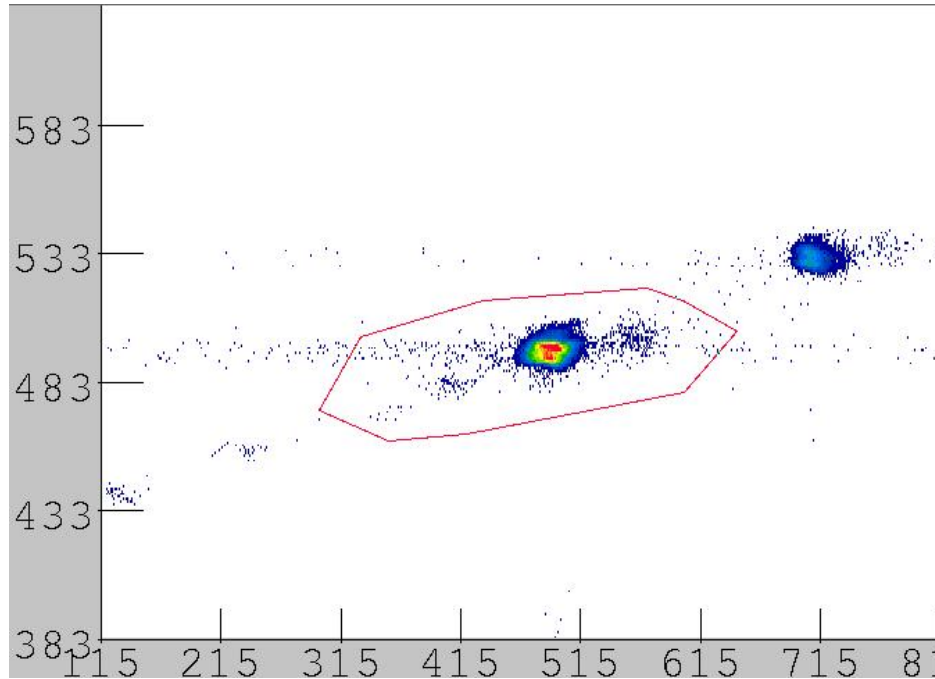
Figure I.18: *TOF XFPE2* vs. *TOF OBJE2* beam ID spectra for the ^{40}S elastic scattering run. Again, the events associated with the ^{40}S beam particles are centered in the spectrum (longer TOF) while the ^{42}Cl beam particles are to the right of the spectrum (shorter TOF).

2. Element Identification (Charge "Z")

The charge "Z" of the reaction products is best measured in the ionization chamber detector of the S800 focal plane. The charge "Z" of the reaction products is equal to the atomic number if the reaction products are fully stripped of their atomic electrons. This assumption is usually true if the incoming beam particles are stripped of their atomic electrons because it is difficult for the reaction products to pickup an electron as they pass through the target at intermediate energies. Also, if the beam particle or reaction were to pickup an electron from the target, the change in charge would change the particle's magnetic rigidity, meaning that it may not make it through the dipole magnets of the spectrograph to be detected by the focal plane detectors (section III.F.3). To identify the "Z" of reaction products, the software gate identifying the beam is applied to the spectrum showing the events in the ionization chamber. Then, the reaction products associated with that beam are separated according to their energy loss (ΔE) in the resulting spectrum. Scanning the elastic scattering run for the beam and viewing the ionization chamber spectrum with the beam identification gate applied tags the reaction products with the same "Z" as the beam. It follows that reaction products with higher ΔE

43

have larger "Z" than the beam and reaction products with lower ΔE have lower "Z". The ionization chamber energy loss spectrum for the ^{40}S production runs is shown in figure I.19.
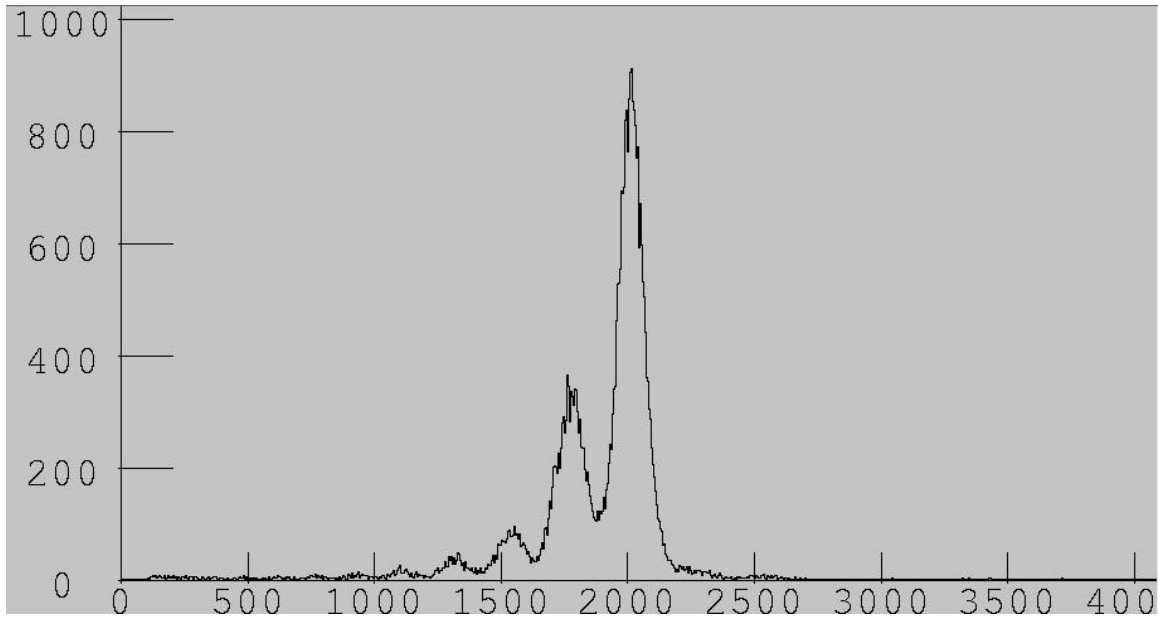
Figure I.19: 1D IC_SUM energy loss spectrum gated on events associated with the ^{40}S beam. The energy loss of the sulfur peak is identified in the ion chamber with the beam elastic scattering run. The largest peak in the spectrum shows the reactions producing sulfur isotopes.

Although most of the elements (products with the same atomic number) are separated from the other elements in the ionization chamber spectrum, some of the events for different elements overlap between the peaks. A better separation between the elements is achieved by comparing two energy loss measurements: one from the ionization chamber ($\Delta E - ICSUM$) and one from the scintillator detectors ($\Delta E - E1$) in the focal plane. The energy resolution of the scintillator detectors alone is not good enough to separate the reaction products with respect to charge, but if used in conjunction with the ionization chamber, some of the events that overlap in the ionization chamber can be separated. Figure I.20 shows $\Delta E - ICSUM$ vs. $\Delta E - E1$ for the ^{40}S beam events in the $d(^{40}S,^{41}Cl)n$ data set. Each elongated "blob" represents a different element produced in the ^{40}S + d reactions. In this step in the data analysis, a software gate identifying the "Z" of the reaction products of interest is created around the proper blob in the $\Delta E - ICSUM$ vs. $\Delta E - E1$ spectrum. This software gate is then used in the next stage of the analysis.

44
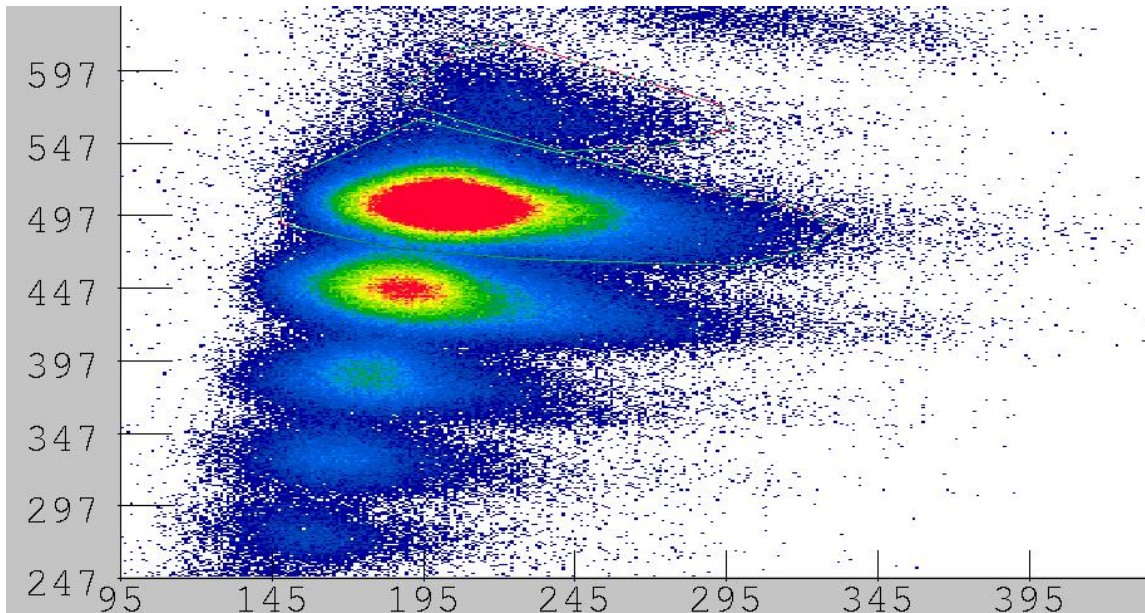
Figure I.20: $\Delta E - ICSUM$ vs. $\Delta E - E1$ gated on the ^{40}S beam. The energy loss of the sulfur blob in the spectrum is identified in the ion chamber with the beam elastic scattering run. The blobs from top to bottom represent events from chlorine, sulfur, phosphorus, and so on.

3. Mass (isotopic) Identification

The next step in the particle identification process is to separate the groups of a given element into individual isotopes, thus uniquely identifying the reaction product with respect to charge, mass and the reaction that produced it. The separation with respect to mass can be done with several different methods, although all of them involve mass separation according to the difference in time of flight (TOF) between reaction products with different mass. Recall once again the non-relativistic version of the magnetic separator equation,

$$\frac{M}{Z}v = B\rho$$

where in the case that the mass separation spectrum is gated on a group of the same element in the $\Delta E - ICSUM$ vs. $\Delta E - E1$ spectrum, the "Z" is a constant. If the magnetic rigidity $B\rho$ is also constant, then heavier isotopes of the same element have smaller velocities in the S800 spectrograph and lighter isotopes have higher velocities. It follows that the heavier isotopes have longer TOFs and the lighter isotopes have shorter TOFs.

Reaction products with the same charge "Z" can also be separated with respect to their position in the S800 focal plane. Since the different isotopes are separated with

respect to velocity by the spectrograph, they are also separated with respect to position on the x-axis in the focal plane. In general, heavier reaction products appear towards the left of the focal plane and lighter reaction products appear towards the right of the focal plane in the position-sensitive CRDC detectors. The position distributions of the particles tend to be quite wide and overlap. Therefore, the position measurement of the reaction products in the focal plane is used with the TOF measurement to obtain the best mass separation between the isotopes.
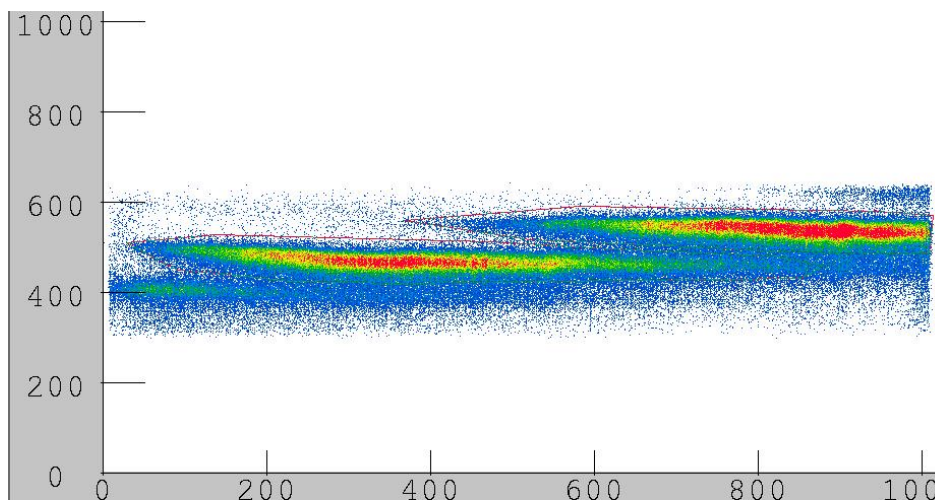
Figure I.21: TOF OBJE2 vs. CRDC1x spectrum showing mass ID of Sulfur events from the ^{40}S beam. ^{39}S events are shown by the red particle group on the left of the spectrum and ^{38}S events are shown by the red particle group on the right of the spectrum.

For this analysis, the mass identification of the reaction products was accomplished by applying both the beam identification gate and the "*Z*" identification gate to the plot of the reaction product's TOF OBJE2 vs. its x-position in the S800 focal plane (CRDC1x). Either of the CRDC detectors could have been used for the position measurement, but CRDC1 had slightly better position resolution. An example of this spectrum is shown in figure I.21, with the "*Z*" identification gate gated on the Sulfur events in the $d(^{40}S,^{41}Cl)n$ data set. The Sulfur events are separated into particle groups, each with about the same TOF and thus the same mass. Also, since TOF decreases with respect to the y-axis in figure I.21, it is evident that heavier mass isotopes have longer TOF and lighter mass isotopes have shorter TOF as expected in the argument given above.

46

The final step in the particle identification process is to assign mass numbers to the isotope groups in the TOF OBJE2 vs. CRDC1x spectrum. The mass numbers are determined by comparing the *M/Z* ratios of the isotopes of the element to the *M/Z* ratio of the reaction product the S800 spectrograph was setup to detect. For example, for the $d(^{40}S,^{41}Cl)n$ data set, the magnetic rigidity of the spectrograph was optimized for the detection of ^{41}Cl ions. This means that the position of the ^{41}Cl ions was setup such that the ^{41}Cl should be detected in the center of the *x*-axis of the S800 focal plane. So, if the *M/Z* ratio of the desired reaction product defines the center position of the focal plane, then isotopes with larger *M/Z* ratios are found to the left of center *x*-position in the TOF OBJE2 vs. CRDC1x spectrum and isotopes with smaller *M/Z* ratios are found to the left. However, the particles in question must have *M/Z* ratios that are close to the *M/Z* ratio of the product the spectrograph was optimized to detect, otherwise they will not have proper magnetic rigidity to make it around the magnet. For example, in figure I.21 where *M/Z*

TABLE I.6: Summary of Reaction Product Identification Steps

Step	Spectrum	Gating Procedure
Beam ID	TOF XFPE2 vs. TOF OBJE2	Gate on reaction product group of interest associated with a given cocktail beam component. Beams are separated with respect to TOF along the diagonal.
Element ("*Z*") ID	$\Delta E - ICSUM$ vs. $\Delta E - E1$	Apply Beam ID gate to this spectrum. Reaction products are separated with respect to charge "*Z*". Gate on the element of interest.
Mass (Isotope) ID	TOF OBJE2 vs. CRDC1x	Apply an "AND" gate with both the Beam ID and the Element ID to this spectrum. Reaction products of different mass are separated with respect to TOF and focal plane position.

for ^{41}Cl is 2.41, the left particle group is the Sulfur isotope with the next larger *M/Z* ratio and the right particle group is the Sulfur isotope with the next smaller *M/Z* ratio. Thus, the particle groups are uniquely identified as ^{39}S (*M/Z* =2.44) and ^{38}S (M/Z=2.38). This result can be verified by applying a gate containing the beam identification, the "Z" identification, and the mass (isotope) identification to a Doppler corrected gamma ray spectrum from SeGA and observing the characteristic gamma rays associated with that nucleus from previous experiments. However, this is not always possible because the

nucleus in question may not have been studied previously. Therefore, checking the particle identification with the gamma rays in coincidence with the particle only serves as a check to the analysis method described above. In the cases where gamma rays are not known for a particular reaction product, the identification with respect to M/Z ratio is verified by comparing the TOF and the position of the product in the focal plane with respect to other nuclei that have known gamma ray transitions. A summary of the steps involved in the identification of the reaction products is given in table I.6.

IV. Experimental Results – Calculation of the Inclusive Cross Sections
A. Calculation of the experimental cross section

The experimental cross sections for the production of a specific reaction product, also known as the inclusive cross sections, are calculated in the usual way with the following equation [29, 30],

$$\sigma_{inc} = \frac{N_R}{N_T N_B}$$

where N_R is the number of reactions resulting in the production of a certain reaction product, N_B is the number of beam particles that pass through the reaction target, and N_T is the number of target particles in the region where the beam interacts with the target. If the target is uniform, then N_T is simply the thickness of the target (in cm) multiplied by the density of the material (in mg/cm^3) and Avogadro's number, and then divided by the mass of the target. For the liquid deuterium target, the areal density of 190 ± 2 mg/cm^2 is the result of multiplying the target thickness in cm by the density of the liquid deuterium (0.169 g/cm^3). N_B is determined using the elastic scattering run to measure the number of beam particles detected in the S800 focal plane for the recorded number of pulses in the XFP and OBJ scintillators. Dividing the number of beam particles detected for the elastic scattering run by the number of pulses in the scintillators calibrates them such that the number of beam particles that interact with the target during the reaction product runs can be calculated based on the number of scintillator pulses recorded in the scaler file for each run. Finally, N_R is measured with the number of S800 event triggers, also known as "trigbits", associated with the reaction product identification gate that includes the beam identification, the element identification, and the mass identification gates combined

together into a single "AND" software gate. This gate is applied to the spectrum "ge.diag.trigbits" in SpecTCL, and channel one in the spectrum corresponds to the downscaled trigbits associated with that gate set. To find the total number of trigbits for a given reaction, the downscaled trigbits must be multiplied by the data acquisition *downscaling factor* (*DS*). The S800 event triggers were downscaled in order to reduce the load on the data acquisition system (dead time) so it could record events from both the reaction product events in the focal plane and the particle-gamma coincidence events in SeGA. The *DS* is calculated by viewing the scalar file for each run and dividing the S800 source pulses (s800.source) by the S800 Trigger pulses (s800.Trig). The *DS* settings used during the experiment are given in table I.7. The *DS* was kept constant for each data set in the experiment. Finally, the trigbits must be corrected to account for the dead time of the data acquisition system. The *live time* (*%live*) of the data acquisition system (1/dead time) is calculated for each experimental run by viewing the scalar file and dividing the pulser live time (pulser.live) by the total number of pulser pulses (pulser.raw) during the run. The *%live* must also be considered for the N_B measurement from the elastic scattering runs, because the number of beam particles detected also depends on the *%live*

TABLE I.7: Downscaling factors (*DS*) for the data sets

Transfer Reaction Data Set	Downscaling factor (*DS*)
$d(^{48}Ca,^{49}Sc)n$	500
$d(^{48}Ca,^{49}Ca)p$	500
$d(^{40}S,^{41}Cl)n$	50
$d(^{42}S,^{43}Cl)n$	50

of the data acquisition system. With N_T, N_B, and N_R calculated, the inclusive cross section in millibarns (mb) can be calculated with the following equation,

$$\sigma_{inc} = \left(\frac{A_{target}}{AD \cdot N_A} \right) \cdot \left(\frac{(XFP_{el} + OBJ_{el}) \cdot \%live_{el}}{(XFP_{prod} + OBJ_{prod}) \cdot Trigbits_{el}} \right) \cdot \left(\frac{Trigbits_{prod} \cdot DS}{\%live_{prod}} \right) \cdot \frac{10^{27}}{0.001}$$

where the first term represents N_T and A_{target} is the mass of the target, *AD* is the areal density of the target (190 ± 2 mg/cm^2), and N_A is Avagadro's number. The second term in the above equation represents N_B as measured in the elastic scattering run where XFP_{el}

and OBJ_{el} are the number of scintillator pulses recorded, $\%live_{el}$ is the live time, XFP_{prod} and OBJ_{prod} are the number of scintillator pulses recorded for the reaction productions run, and $Trigbits_{el}$ is the number of S800 event triggers associated with the beam particle in question. The third term represents N_R as measured in the reaction runs where $Trigbits_{prod}$ is the number of trigbits associated with a given reaction product, DS is the downscaling factor, and $\%live_{prod}$ is the live time during the runs. The final factor of $10^{27}/0.001$ scales the cross section into units of millibarns (mb).

B. S800 Efficiency Corrections

The cross sections calculated with the σ_{inc} equation must be corrected for the efficiency of the S800 detectors. It is assumed that the detection of ions from either the beam or the reaction products in the S800 ionization chamber or focal plane scintillator detectors is 100% efficient, since the rate limits of both detectors were not approached during the experiment. The efficiencies of the TPPACs are not considered in this correction since measurements in the TPPACs were not considered in the analysis as was explained in the gating section (section III.F). Therefore, only the efficiencies of the CRDC detectors need to be considered for the efficiency correction to the cross sections.

In the data acquisition software for the S800 spectrograph, the TOF XFPE2 and TOF OBJE2 measurements are not recorded for an event in the ionization chamber unless events are simultaneously recorded in both CRDC detectors. An event where the TOFs are not recorded is assigned TOF = 0 for the TOF measurements. While these events are detected in the ionization chamber and focal plane scintillator detectors, they are not assigned a TOF OBJE2 or CRDC1x measurement. It follows that these events are not included in the particle identification gating scheme.

Based on the information above, the number of events where the TOF XFPE2 and TOF OBJE2 measurements fail is the same as the number of events where the position measurement in either CRDC1 and/or CRDC2 is not recorded due the efficiency of the detectors. To measure the number of events where the TOF measurements fail for each gating scheme, the following procedure was used. First, a separate spectrum plotting $\Delta E - ICSUM$ vs. $\Delta E - E1$ is created without the beam identification gate applied to it (since the beam ID gate involves TOF measurements). Then, an identical element

identification gate as the one used in the particle identification gating scheme is drawn in this spectrum. This element identification gate will include events from multiple beam particle types if the cocktail beam runs are considered, but it still leads to an accurate measurement of the efficiencies of the CRDCs. The new element identification gate is then applied to a separate spectrum of TOF XFPE2 vs. TOF OBJE2 and the data runs are scanned. The number of events in the TOF XFPE2 vs. TOF OBJE2 spectrum not in channel 0 represent the number of events with good TOF measurements since they were detected simultaneously in both CRDCs. Therefore, the efficiency of the CRDCs is:

$$Eff_{CRDCs} = \frac{\# \text{ of events not in channel } 0 \text{ of TOF } XFPE2 \text{ vs. TOF } OBJE2}{\# \text{ of events in element ID gate of } \Delta E - ICSUM \text{ vs. } \Delta E - E1}.$$

To calculate the *efficiency correction* (eff_{corr}) for the inclusive cross section, the Eff_{CRDCs} is recorded for the elastic scattering and reaction production runs separately. Then, the eff_{corr} for the cross section measurements in a data set is:

$$Eff_{corr} = \frac{Eff_{CRDCs}(Reaction\ Production\ Runs)}{Eff_{CRDCs}(Elastic\ Scattering\ Run\ for\ the\ Data\ Set)}$$

and the measured experimental cross section for a given reaction is:

$$\sigma_{exp} = \frac{\sigma_{inc}}{Eff_{corr}}.$$

The efficiency of the CRDC detectors in the S800 focal plane depended mainly on the rate of the incoming beam particles. The efficiency was relatively good for the

TABLE I.8: Cross Section Efficiency Corrections (Eff_{corr}) for the data sets

Transfer Reaction Data Set	Eff_{corr}
$d(^{48}Ca, ^{49}Sc)n$	0.9617
$d(^{48}Ca, ^{49}Ca)p$	0.9839
$d(^{40}S, ^{41}Cl)n$	0.8291[*]
$d(^{42}S, ^{43}Cl)n$	0.9822

*Only data runs with eff_{CRDCs} above 75% are considered.

^{48}Ca and ^{42}S runs. However, several of the ^{40}S data collection runs were found to have eff_{CRDCs} under 75%. This was because the ^{40}S cocktail beam had more beam particles per second than the ^{48}Ca beam since the cocktail beam contaminants, such as ^{42}Cl, were not included in the calculation of the beam rate listed in table I.1. The low efficiency runs

were not included in the calculation of the inclusive cross sections for the ^{40}S data set. Table I.8 contains the efficiency corrections calculated for each data set. It was noted during the analysis that the efficiency correction did not change significantly ($< 1\%$) for different reaction products.

C. Focal Plane Position Distribution Corrections

The large momentum acceptance of the S800 spectrograph dipole magnets ($\pm 6\%$) allowed other reaction products besides the single nucleon pickup reactions to be detected with the focal plane detectors, as long as their M/Z ratios were not much different than the reaction product of interest. This allowed detection of charge exchange reactions, single and multiple nucleon knockout reactions, and fragmentation reactions. However, there were several reaction products that were detected with incomplete position distributions in the focal plane due to the limited acceptance of the dipole magnets. In general, reaction products with M/Z ratios within $\pm 2\%$ of the optimum M/Z ratio had position distributions that were completely in the focal plane and products within $\pm 4\%$ of the optimum M/Z ratios had position distributions that were only partially in the focal plane.

For the reaction products with position distributions that were more than 50% in the focal plane, the experimental total cross sections were estimated assuming the position distributions were approximately Gaussian shaped and symmetric about the maximum of the distribution. The position distribution was plotted in the spectrum CRDC1x and gated with the particle identification software gate. Then, the number of counts from the edge of the position distribution that was completely in the focal plane to the maximum of the position were calculated and also the total number of counts in the distribution. The percentage of the distribution detected in the focal plane was determined as:

$$\% \text{ in focal plane} = \frac{\text{total counts in the distribution}}{(\text{counts from minimum (edge) of the distribution to the maxmium}) \cdot 2}.$$

It was noted during the analysis of the data that some of the position distributions that were completely detected by the focal plane detectors were not symmetric about their maxima. Usually the asymmetry was characterized by a long "tail" in the distribution on

the right side (low momentum) of the distribution. This "tail" contained around 5% of the counts in the total distribution, but the number of counts in the "tail" varied depending on the reaction, and sometimes was not present. Since the presence and size of the "tail" in the position distribution was impossible to determine unless it was detected, additional systematic error (10%) in the experimental cross section is assumed for reaction products whose distributions were only partially detected in the focal plane.

Cross sections for reaction products with less than 50% of their position distributions detected in the S800 focal plane are also reported in the results section. However, the amount of the distribution in the focal plane was difficult to estimate without detecting the maximum of the distribution. For these reaction products, it was assumed that the shape of their position distributions was similar to that of other isotopes of the same element. Thus, by comparing the incomplete position distribution of one isotope to the complete distribution of another isotope, the percentage of the distribution for the reaction product only partially detected in the focal plane was estimated. In these cases, additional systematic error (up to 50%) is assumed due to the limited information about the position distribution. Experimental cross sections determined for these reactions should not be considered accurate measurements, but are reported as estimates of the sizes of the cross sections for these reactions for future reference.

D. Errors for the Experimental Cross Sections

For the cases where the complete distributions of the reaction products were detected in the focal plane, the main uncertainties in the experimental data arose from the choice of particle identification software gates (10%), the stability of the beam current (5%), and the pressure drifts in the liquid deuterium target cell (1%). These systemic errors were independent and were added in quadrature as follows [31],

$$\delta \sigma_{exp} = \sqrt{(\delta a)^2 + (\delta b)^2 + (\delta c)^2 + ...}$$

where "a", "b" and "c" are independent sources of error. The statistical error, calculated by $\sqrt{N}/N$ where "N" is the number of counts, was ($< 3\%$) because the number of trigbits for the experimental cross sections reported is $N > 1000$ once the trigbits are multiplied by the downscaling factor DS. Thus, the total uncertainty for the reaction products with

complete position distributions was around 11%. For the cases where the position distributions of the reaction products were only partially in the focal plane, but 50% or more of the distribution was detected, an additional error of 10% is added in quadrature as discussed in the previous section. The total uncertainty in the cross section for these reaction products was 15%. Finally, for reaction products that had less than 50% of their position distributions detected in the focal plane, the error was dominated by the problem with estimating the amount of the distribution that was accepted into the spectrograph. For these distributions, an experimental error of up to 50% is assumed.

F. Experimental Results – Experimental Cross Sections for ^{48}Ca+d

The experimental cross sections for the $^{48}Ca+d$ primary beam reactions are reported in tables I.9 and I.10. The S800 event triggers (trigbits) for each reaction product were calculated assuming the particle identification gating scheme summarized in table I.6. The experimental cross sections were calculated using the equation given in section IV.A and were corrected for the detection efficiency of the S800 with the equations given in section IV.B. The estimated percentage of the position distribution for each reaction product detected in the S800 focal plane and the estimates of the total cross section for reaction are also reported.

G. Comparison of ^{48}Ca+d cross sections to ^{48}Ca+^{9}Be and ^{48}Ca+^{181}Ta

The experimental cross sections measured in the $^{48}Ca+d$ experiment were compared with cross sections measured by Mocko et al. [33] for $^{48}Ca+^{9}Be$ and $^{48}Ca+^{181}Ta$ at 141.96 MeV/nucleon to study the target dependence of the reaction cross sections. The measured cross sections for these three reactions were also compared to predictions for the cross sections calculated with the program LISE [28]. The results of this comparison are shown in figure I.22.

For the LISE calculations, it was assumed that the reaction mechanism involved in the three reactions was heavy-ion fragmentation [10, 33]. Heavy-ion fragmentation can be described as a two step process called abrasion-ablation [10, 34]. In the abrasion part

TABLE I.9: Experimental production cross sections for ^{48}Ca + d reactions at 100 MeV/nucleon (S800 spectrograph set for detection of ^{49}Sc).

Reaction Product	Measured σ_{exp} (mb)	Estimated % in S800 focal plane	Estimated Total Cross Section (mb)	Reaction type
^{49}Sc	0.7 ± 0.08	100	0.7 ± 0.08	(d,n)
^{48}Sc	5.4 ± 0.6	90	6 ± 1	(d,2n)
^{47}Ca	125 ± 14	100	125 ± 14	1n out
^{46}Ca	91 ± 10	80	114 ± 23	2n out
^{45}Ca	3.2 ± 0.4	5	64 ± 32 [#]	3n out
^{46}K	5.9 ± 0.6	15	39 ± 20 [#]	1p, 1n out
^{45}K	41 ± 5	70	59 ± 9	1p, 2n out
^{44}K	38 ± 4	70	54 ± 9	1p, 3n out
^{43}K	7.5 ± 0.8	20	37 ± 8 [#]	1p, 4n out
^{43}Ar	7.8 ± 0.8	30	26 ± 13 [#]	2p, 3n out
^{42}Ar	13 ± 2	100	13 ± 2	2p, 4n out
^{41}Ar	4.7 ± 0.5	30	16 ± 8 [#]	2p, 5n out
^{41}Cl	1.0 ± 0.1	20	5 ± 3 [#]	3p, 4n out
^{40}Cl	3.5 ± 0.4	100	3.5 ± 0.4	3p, 5n out
^{39}Cl	4.5 ± 0.5	50	9 ± 2	3p, 6n out

[#] These nuclei were detected on the edge of the S800 focal plane and their detection was confirmed by their signature gamma rays, given in [10]. A much larger uncertainty (50%) was assumed here due to the small amount of the distribution detected.

TABLE I.10: Experimental production cross sections for ^{48}Ca + d reactions at 100 MeV/nucleon (S800 spectrograph set for detection of ^{49}Ca).

Reaction Product	Measured σ_{exp} (mb)	Estimated % in S800 focal plane	Estimated Total Cross Section (mb)	Reaction type
^{49}Ca	0.6 ± 0.06	100	0.6 ± 0.06	(d,p)
^{48}K	2.3 ± 0.3	75	3.1 ± 0.6	(d,2p)
^{47}K	40 ± 4	100	40 ± 4	1p out
^{46}K	21 ± 3	50	42 ± 6	1p, 1n out
^{46}Ar	0.3 ± 0.03	10	3 ± 1.5 [#]	2p out
^{45}Ar	1.8 ± 0.2	100	1.8 ± 0.2	2p, 1n out
^{44}Ar	4 ± 0.4	50	8 ± 1	2p, 2n out
^{43}Ar	3.5 ± 0.4	10	35 ± 18 [#]	2p, 3n out
^{43}Cl	0.2 ± 0.02	25	0.8 ± 0.4 [#]	3p, 2n out
^{42}Cl	1 ± 0.1	100	1 ± 0.1	3p, 3n out
^{41}Cl	1.5 ± 0.2	40	4 ± 1	3p, 4n out

[#] These nuclei were detected on the edge of the S800 focal plane and their detection was confirmed by their signature gamma rays, given in [10]. A much larger uncertainty (50%) was assumed here due to the small amount of the distribution detected.

of the process, some of the nucleons in the projectile and the target overlap and are removed as the particles interact. In the ablation part of the process, the resulting fragment dissipates its excitation energy gained during abrasion by particle emission and
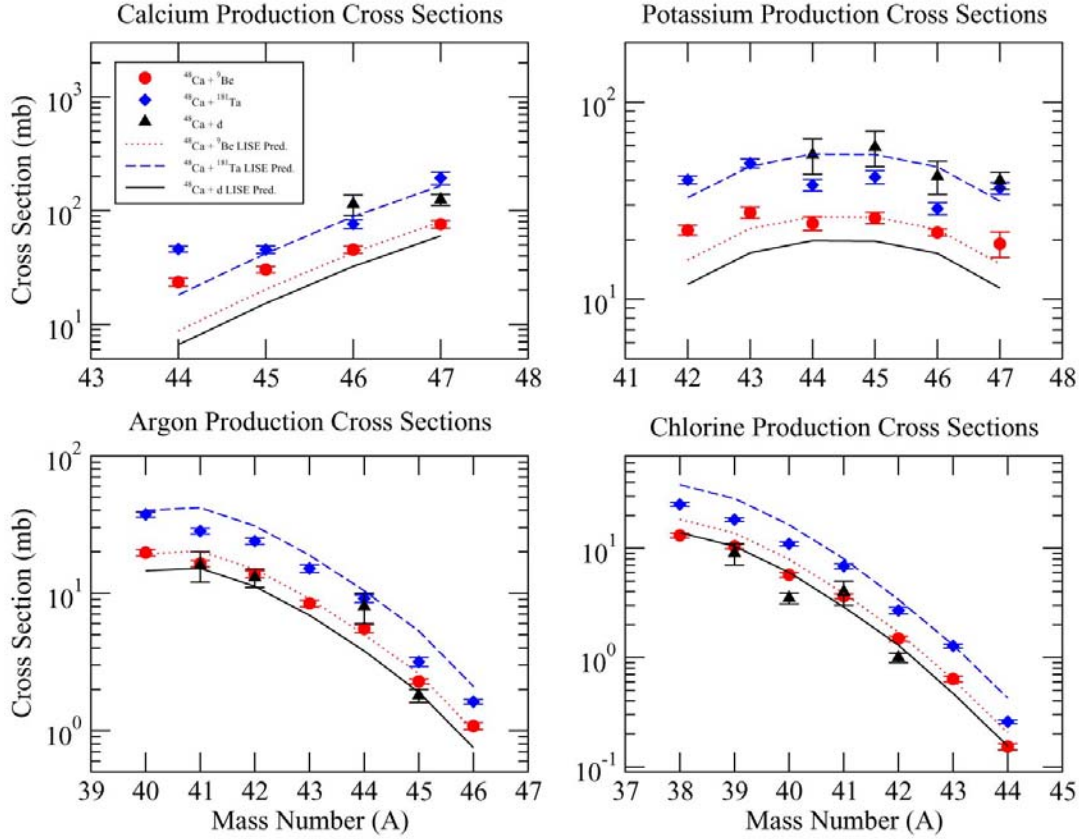
Figure I.22: Cross Sections for the Reactions ^{48}Ca+d from the current work, ^{48}Ca+^{9}Be and ^{48}Ca+^{181}Ta [23].

different states of the resulting reaction product are populated statistically with weights determined by the excitation energy of the product. Since the number of nucleons that overlap in the abrasion part of reaction depends on the number of nucleons in the target (larger target, in general, implies larger volume for stable nuclei), it follows that the size of the cross section for abrasion should increase with the increasing mass of the target. Also, abrasion and ablation are both statistical processes depending on the number of nucleons involved in the reaction and the energy level structure of the resulting reaction product. Thus, these processes produce cross sections of size independent of the kinetic energy of the projectile. With this result, the comparison between the cross sections for the three reactions in figure I.22 is a valid comparison.

Under the assumption that the process involved in the reactions was heavy-ion fragmentation, the ^{181}Ta target should always produce the largest cross section for any reaction and the deuterium target should always produce the lowest cross section. The cross section measurements from the ^{9}Be and ^{181}Ta follow this assumption, although in some cases, such as the potassium and chlorine isotope production, the LISE prediction expects a higher cross section for the ^{181}Ta target. The LISE predictions for all three targets for the argon and chlorine isotopes are also reasonable. However, the experimental cross sections for the removal of 2-5 nucleons in the $^{48}Ca+d$ reactions were much larger (factors of 5) than expected for the deuterium target and in some cases were even larger than the measured cross sections for the ^{181}Ta target. These results suggest that there are other mechanisms that contribute to the size of the $^{48}Ca+d$ reaction cross sections, in addition to heavy-ion fragmentation.

H. Comparison of d(^{48}Ca,^{49}Sc)n and d(^{48}Ca,^{49}Ca)p Cross Sections to other (d,n) cross sections at high energy.

Previous studies of deuteron-induced reactions on stable targets at intermediate energies have focused on using proton removal and forward kinematics to produce high energy neutrons [35,36,37]. These studies have shown that the cross section for neutron production, through reactions such as ^{9}Be(d,n)X and ^{12}C(d,n)X with deuteron beams of 100 MeV/nucleon, are between 500 and 700 mb, decreasing to around 400 mb at 1 GeV/nucleon. However, these experiments are inclusive with respect to all possible final states of the residual nucleus and so are distinct from the current work. References [35] and [36] comment that, at energies of order 100 MeV/nucleon, deuteron breakup reactions produce a significant part of the neutron production cross section. Thus, the reaction cross sections measured here for $d(^{48}Ca,^{49}Sc)n$ and $d(^{48}Ca,^{49}Ca)p$ with bound final states of the reaction products, are a very small component of these large inclusive cross sections for neutron production discussed elsewhere (Chapter 2).

I. Experimental Results – Experimental Cross Sections for ^{40}S+d and ^{42}S+d

The experimental cross sections for the $^{40}S+d$ and $^{42}S+d$ exotic beam reactions are reported in tables I.11 and I.12. The S800 event triggers (trigbits) for each reaction product were calculated assuming the particle identification gating scheme summarized

in table I.6. The experimental cross sections were calculated using the cross section equation given in section IV.A and were corrected for the detection efficiency of the S800 with the equations given in section IV.B. The estimated percentage of the position distribution for each reaction product detected in the S800 focal plane and the estimates of the total cross section for reaction are also reported.

J. Discussion of Experimental Cross Section Results

      One result of this experiment is that it is possible to conduct experiments involving nucleon pickup reactions such as $d(^{Z}A,^{Z+1}A+1)n$ and $d(^{Z}A,^{Z}A+1)p$ at intermediate energies within a reasonable amount of time (a few days). This result is significant because of the large body of previous work, both experimental and theoretical, available for similar single particle transfer reactions on stable nuclei that can be compared to the future new results. Reasonably well-tested models such as the Distorted Wave Born Approximation (DWBA) can be applied to analysis of single particle transfer reactions with exotic nuclei. If successful, these analyses will provide important insight into their structure. However, if there are significant deviations between theory and experiment due to the relatively high energies used to produce exotic nuclei at the proton and neutron driplines, it may be necessary to develop new models for transfer reactions. In this case, the use of the deuterium target should make this development easier because of the extensive knowledge that already exists on the structure of the deuteron.

      The charge exchange reactions $d(^{48}Ca,^{48}Sc)X$, $d(^{48}Ca,^{48}K)X$, $d(^{40}S,^{40}Cl)X$, $d(^{42}S,^{42}Cl)X$ measured in this experiment had larger cross sections than that of the nucleon pickup reactions. While these cross sections were small compared to the nucleon knockout reactions, information on nuclei populated in these reactions can be gathered within a reasonable amount of time also. Here again, knowledge of the deuteron structure should make it easier to obtain structure information on the residual nucleus produced.

      The single nucleon knockout reactions had cross sections that were about 100 times larger than those of the single nucleon pickup reactions. The cross sections for these reactions were also larger than those expected from the projectile fragmentation calculations for the deuterium target. This suggests that the reactions have contributions from direct reactions as has been previously observed with [9]Be and ^{12}C targets. As a

58

TABLE I.11: Experimental production cross sections for ^{40}S + d reactions at 100 MeV/nucleon (S800 spectrograph set for detection of ^{41}Cl).

Reaction Product	Measured σ_{exp} (mb)	Estimated % in S800 focal plane	Estimated Total Cross Section (mb)	Reaction type
^{41}Cl	0.55 ± 0.07	**100**	0.55 ± 0.07	**(d,n)**
^{40}Cl	0.63 ± 0.07	**88**	0.71 ± 0.08	**(d,2n)**
^{39}S	71 ± 8	**100**	71 ± 8	**1n out**
^{38}S	53 ± 6	**84**	63 ± 7	**2n out**
^{37}P	19 ± 2	**80**	24 ± 3	**1p, 2n out**
^{36}P	17 ± 2	**84**	20 ± 2	**1p, 3n out**
^{35}P	4 ± 0.5	**20**	20 ± 10	**1p, 4n out**
^{35}Si	0.8 ± 0.1	**40**	2.1 ± 1	**2p, 3n out**
^{34}Si	5.8 ± 0.6	**100**	5.8 ± 0.6	**2p, 4n out**
^{33}Si	3.0 ± 0.3	**70**	4.3 ± 0.5	**2p, 5n out**
^{32}Al	1.0 ± 0.1	**80**	1.3 ± 0.2	**3p, 5n out**
^{31}Al	2.3 ± 0.3	**71**	3.2 ± 0.4	**3p, 6n out**
^{30}Al	0.4 ± 0.05	**20**	2 ± 1	**3p, 7n out**

TABLE I.12: Experimental production cross sections for ^{42}S + d reactions at 100 MeV/nucleon (S800 spectrograph set for detection of ^{43}Cl).

Reaction Product	Measured σ_{exp} (mb)	Estimated % in S800 focal plane	Estimated Total Cross Section (mb)	Reaction type
^{43}Cl	0.62 ± 0.07	**100**	0.62 ± 0.07	**(d,n)**
^{42}Cl	1.2 ± 0.1	**86**	1.4 ± 0.2	**(d,2n)**
^{41}S	69 ± 8	**100**	69 ± 8	**1n out**
^{40}S	66 ± 7	**100**	66 ± 7	**2n out**
^{39}S[#]	5 ± 0.5	**10**	50 ± 25[#]	**3n out**
^{39}P	10 ± 1	**90**	11 ± 1	**1p, 2n out**
^{38}P	15 ± 2	**100**	15 ± 2	**1p, 3n out**
^{37}P	8 ± 0.9	**80**	10 ± 1	**1p, 4n out**
^{36}Si	2.4 ± 0.3	**88**	2.7 ± 0.3	**2p, 4n out**
^{35}Si	2.5 ± 0.3	**85**	2.9 ± 0.3	**2p, 5n out**
^{34}Si	1.0 ± 0.1	**50**	2.0 ± 0.5	**2p, 6n out**
^{33}Al	1.1 ± 0.1	**100**	1.1 ± 0.1	**3p, 6n out**
^{32}Al	0.6 ± 0.06	**60**	1 ± 0.2	**3p, 7n out**

[#] ^{39}S was detected on the edge of the S800 focal plane and its detection was confirmed by comparing the gamma rays detected in coincidence with the gamma rays detected in the ^{40}S+d runs. A much larger uncertainty (50%) was assumed here due to the small amount of the distribution detected.

result, in future experiments with exotic nuclei where single nucleon knockout and pickup are compared, it will be unnecessary to switch targets to perform different reactions because the knockout cross sections for the three targets are comparable in size.

In addition, the few-nucleon removal reactions (2 to 5 nucleons removed) for the three beams on the deuterium target also had larger cross sections than those expected from heavy ion fragmentation processes. This result supports the conclusion of Obertelli et al. [34] that both non-dissipative processes and statistical mechanisms contribute to the cross section in few-nucleon removal processes.

As a final note, this experiment illustrates that it is possible to produce a wide variety of exotic, neutron rich nuclei by bombarding light targets with stable and exotic heavy ions. The difference with the deuterium target is that it may be possible to better understand the reaction mechanisms at work in the experiment than with heavier targets.

The author's major contribution to this experiment was his participation in the planning leading up to the execution of the experiment. After the experiment, the author led the analysis of the experimental data by installing and calibrating the SpecTCL analysis software, collaborating with the staff scientists at the NSCL to learn how to identify the various reaction products produced in the experiment, and calculate the production cross sections for these reaction products. The results presented in this dissertation will be published in journal articles by the author of this dissertation (see Biographical Sketch).

CHAPTER 2

THEORETICAL CALCULATIONS FOR THE SINGLE NUCLEON PICKUP AND KNOCKOUT REACTIONS

I. Adiabatic Model Calculations for (d,n) and (d,p) reactions

The importance of deuteron breakup at intermediate energies means that transfer reactions should *not* be treated as at lower energies, i.e. using the distorted-wave Born Approximation (DWBA). Even at lower beam energies, breakup effects have been shown to be significant in calculations of deuteron elastic scattering [1] and (d,p) reactions [2]. In addition, it is difficult to obtain empirical optical model parameters on exotic nuclei. The Johnson-Soper (JS) adiabatic model, that treats the deuteron (neutron and proton) and projectile nucleus as a three-body problem, and calculates the required interactions between the neutron and proton and the projectile microscopically, overcomes both of these difficulties [1,2]. The JS model has been used previously to analyze the ^{48}Ca(d,n)^{49}Sc reaction, measured at energies up to 39.5 MeV/nucleon in normal kinematics [3]. This approach was also used recently to study spectroscopic factors for the ^{12}C(d,p)^{13}C$_{g.s.}$ reaction at energies from 6 to 28 MeV per nucleon [4].

The basis of the adiabatic model, written here for the (d,p) reaction, is the transfer reaction amplitude,

$$T(d,p) = \int d\vec{R}\, d\vec{r}\; \phi_n^*(\vec{R}_n)[\chi_p^{(-)}(\vec{R}_p)]^* \, V_{np}(\vec{r}) \Psi_d^{Ad}(\vec{r},\vec{R}),$$

where $\chi_p^{(-)}(\vec{R}_p)$ is the outgoing proton distorted wave, $\phi_n(\vec{R}_n)$ is the transferred neutron bound state and V_{np} is the neutron-proton interaction. Here $\Psi_d^{Ad}(\vec{r},\vec{R}) = \psi_d^{Ad}(\vec{r},\vec{R})\, \phi_d(\vec{r})$ is the adiabatic three-body wave function and $\phi_d(\vec{r})$, the deuteron ground state, appears as a factor because of the use of the adiabatic/sudden approximation. Breakup effects are retained through the dependence of $\psi_d^{Ad}(\vec{r},\vec{R})$ on the neutron-proton relative coordinate $\vec{r}$: the DWBA [5] is recovered if $\psi_d^{Ad}(\vec{r},\vec{R})$ is replaced by its elastic component [1, 5]. For each *fixed* $\vec{r}$, this three-body wave function satisfies the wave equation,

$$[E_d - T_R - U_{tot}(\vec{r},\vec{R})]\psi_d^{Ad}(\vec{r},\vec{R}) = 0$$

at the center of mass energy of the entrance channel, $E_d = E + \varepsilon_d$, with ε_d the deuteron separation energy, and $U_{tot}(\vec{r}, \vec{R})$ is the sum of the neutron- and proton-projectile optical potentials. Since, due to V_{np}, the transfer amplitude requires knowledge of this three-body wave function only for small neutron-proton separations, $U_{tot}(\vec{r}, \vec{R})$ is well described by $U_{tot}(\vec{r} \approx 0, \vec{R})$, the sum of the neutron-projectile and proton-projectile optical potentials [14] at coincidence. Small corrections to $U_{tot}(\vec{r}, \vec{R})$ due to the non-zero range of V_{np} are discussed in [6, 7]. The effects of the finite range of V_{np} in the transition amplitude itself are included using the local energy approximation (LEA) [5, 8]. We take the deuteron vertex function $V_{np}\phi_d(r)$ strength (D_0) and range (β) parameters from the Reid soft-core nucleon-nucleon (NN) interaction [9].

The nucleon-projectile optical model potentials in U_{tot} and in the exit channel are computed microscopically from the Jeukenne, Lejeune, and Mahaux (JLM) [10] nuclear matter effective NN interaction, based on the Reid hard-core free NN interaction [11]. This interaction includes a Gaussian form factor with a range of 1 fm, as in reference [12], and the required effective mass correction to the imaginary part of the potential (Eq. (29) of [10]) discussed in references [13, 14]. The nucleon optical potentials are obtained by folding the JLM interactions with the one-body density of the projectile and residual nuclei, using the mid-point local density prescription [12, 15]. These one-body densities were taken from spherical Hartree-Fock calculations using the Skyrme SKX interaction [16]. Analysis of nucleon elastic scattering data on both light and medium mass systems has shown that scale factors $\lambda_V = 1.0$ and $\lambda_W = 0.8$ should be applied to these computed real and imaginary parts of the optical potential [12, 15]. In this analysis, spin-orbit terms in the nucleon optical potentials were not included.

The transferred nucleon single-particle wave functions are calculated in a Woods-Saxon potential well with conventional radius and diffuseness parameters $r_0 = 1.25$ fm and $a = 0.70$ fm. The strengths of these binding potentials are adjusted to support bound eigenstates with the physical nucleon separation energy. Non-locality effects [17] are not included in the entrance or exit channel or the bound state wave functions. Calculations

are carried out with the computer code TWOFNR [18]. The results of these calculations are as follows.

The mid-target energy for the ^{48}Ca beam is 93.1 MeV/nucleon, as given in table I.1. In the case of $d(^{48}Ca,^{49}Sc)n$, a single proton is added into one of several orbits in the *fp* -shell. Previous transfer reaction studies of single particle states in ^{49}Sc and the reported spectroscopic strengths for the strongly populated states are summarized in table II.1.

TABLE II.1: Spectroscopic Strengths for Single Particle Proton States in ^{49}Sc

^{49}Sc state (MeV)[*]	C^2S	Reaction	Beam Energy	Reference
g.s. (7/2⁻)	0.72	^{48}Ca(d,n)^{49}Sc	79 MeV	[3][#]
	1.0	^{48}Ca(^{3}He,d)^{49}Sc	12 MeV	[19]
	0.91	^{48}Ca(^{3}He,d)^{49}Sc	22 MeV	[20]
	1.06	^{48}Ca(^{7}Li,^{6}He)^{49}Sc	34 MeV	[21]
3.08 MeV (3/2⁻)	0.31	^{48}Ca(d,n)^{49}Sc	79 MeV	[3][#]
	0.68	^{48}Ca(^{3}He,d)^{49}Sc	12 MeV	[19]
	0.60	^{48}Ca(^{3}He,d)^{49}Sc	22 MeV	[20]
	0.54	^{48}Ca(^{7}Li,^{6}He)^{49}Sc	34 MeV	[21]
4.07 MeV (5/2⁻)	0.20	^{48}Ca(^{3}He,d)^{49}Sc	12 MeV	[19]
	0.21	^{48}Ca(^{3}He,d)^{49}Sc	22 MeV	[20]
	0.22	^{48}Ca(^{7}Li,^{6}He)^{49}Sc	34 MeV	[21]
4.49 MeV (1/2⁻)	0.31	^{48}Ca(^{3}He,d)^{49}Sc	12 MeV	[19]
	0.25	^{48}Ca(^{3}He,d)^{49}Sc	22 MeV	[20]
	0.47	^{48}Ca(^{7}Li,^{6}He)^{49}Sc	34 MeV	[21]
5.09 MeV (5/2⁻)	0.35	^{48}Ca(^{3}He,d)^{49}Sc	12 MeV	[19]
	0.37	^{48}Ca(^{3}He,d)^{49}Sc	22 MeV	[20]
	0.38	^{48}Ca(^{7}Li,^{6}He)^{49}Sc	34 MeV	[21]

*Energies and spin and parity assignments for ^{49}Sc levels taken from reference [21]
#Spectroscopic factors in reference [3] were obtained using the JS adiabatic approximation. All others were obtained using a standard DWBA analysis technique.

In the present work, it was difficult to quantify which ^{49}Sc final states were being populated for several reasons. First, the inclusive $d(^{48}Ca,^{49}Sc)n$ reaction cross section was low compared with other reactions (see table I.9). Second, previous work involving the beta-decay of ^{49}Ca to ^{49}Sc [22] has shown that the gamma rays from the decay of the negative parity ^{49}Sc excited states are direct decays to the ground state. Thus, due to the low efficiency of SeGA for gamma ray energies above 3 MeV (<1%) and the difficulty in producing a Doppler reconstruction of the in-flight gamma rays for energies greater than

about 2.5 MeV, detection of the individual single-particle states was not possible, other than a *possible* small peak observed at 3.08 MeV. Third, the ground state of ^{49}Sc is not detected directly in the data, having no gamma-ray tag. However, the total production cross section for ^{49}Sc was detected in the S800 focal plane. Assuming therefore that (i) the same final states were populated in this work as in the previous experiments, and (ii) that the spectroscopic factors are constant with respect to energy, then a comparison can be made between the experimental and theoretically calculated total production cross sections. The partial cross section calculations to the individual final states in ^{49}Sc are shown in table II.2.

TABLE II.2: Adiabatic Model Calculations for $d(^{48}Ca,^{49}Sc)n$ at 93.1 MeV/nucleon

^{49}Sc state	l-value	σ_{theory} (mb)	Avg. C^2S [#]	$\sigma_{calculated}$ (mb)
g.s.	3	0.88	0.92	0.81
3.08 MeV	1	0.20	0.53	0.11
4.07 MeV	3	0.55	0.21	0.12
4.49 MeV	1	0.096	0.34	0.033
5.09 MeV	3	0.50	0.37	0.19
Total				1.26
			Experiment σ_{tot}	0.7 ± 0.08

[#]Average of Spectroscopic factors from references [3,19,20,21]

The $d(^{48}Ca,^{49}Sc)n$ calculations in table II.2 show a few interesting features. First, the calculated cross section of 1.26 mb is reasonable when compared with the experimental cross section of 0.71 mb. Most of the cross section for production of the ^{49}Sc is to the ground state. This is consistent with the experimental observation of few gamma decays of ^{49}Sc excited states. Also, states with $l = 3$ have higher calculated cross sections than the $l = 1$ states due to angular momentum matching favoring the states with higher orbital angular momentum. This result is in sharp contrast with work at lower beam energies, e.g. [21], where the $l = 1$ states (in particular the 3.08 MeV and 4.49 MeV states) have higher partial cross sections than the $l = 3$ states. Finally, the bound final state wave functions $\phi_n(\vec{R}_n)$ in the transfer amplitude are also sensitive to the radius parameter of the potentials used. However, despite these uncertainties, there is good agreement between the measured cross section and the calculated cross section.

Calculations were also carried out for the $d(^{48}Ca, {}^{49}Ca)p$ reaction at 93.1 MeV/nucleon. In this case, the $1f_{7/2}$ neutron shell is essentially full, leaving the $2p_{3/2}$, $2p_{1/2}$, and $1f_{5/2}$ shells available for the neutron to be transferred into. Earlier work has shown that the neutron can also be transferred to the $1g_{9/2}$ state [23, 24]. These earlier studies of the $^{48}Ca(d,p)^{49}Ca$ reaction, in normal kinematics and with energies above 20 MeV, are summarized in table II.3.

TABLE II.3: Spectroscopic Strengths for Single Particle Neutron States in ^{49}Ca

^{49}Ca state (MeV)[*]	C^2S	Reaction	Beam Energy	Reference
g.s. (3/2⁻)	0.72	^{48}Ca(d,p)^{49}Ca	20 MeV	[23]
	1.0	^{48}Ca(d,p)^{49}Ca	56 MeV	[24]
2.02 MeV (1/2⁻)	0.91	^{48}Ca(d,p)^{49}Ca	20 MeV	[23]
	1.06	^{48}Ca(d,p)^{49}Ca	56 MeV	[24]
3.59 MeV (5/2⁻)	0.17	^{48}Ca(d,p)^{49}Ca	20 MeV	[23]
	0.11	^{48}Ca(d,p)^{49}Ca	56 MeV	[24]
3.99 MeV (5/2⁻)	0.99	^{48}Ca(d,p)^{49}Ca	20 MeV	[23]
	0.84	^{48}Ca(d,p)^{49}Ca	56 MeV	[24]
4.03 MeV (9/2⁺)[#]	0.37	^{48}Ca(d,p)^{49}Ca	20 MeV	[23]
	0.14	^{48}Ca(d,p)^{49}Ca	56 MeV	[24]
4.07 MeV (3/2⁻)	0.13	^{48}Ca(d,p)^{49}Ca	56 MeV	[24]
4.26 MeV (1/2⁻)	0.12	^{48}Ca(d,p)^{49}Ca	56 MeV	[24]

* Energies and spin assignments taken from Nuclear Data Sheets [25] except where noted.
# The 4.03 MeV state has disputed spin values. DWBA analysis in [23,24] say that this level is $l = 4$, implying that this level corresponds to the $1g_{9/2}$ shell and would make the spin of this state 9/2⁺. However, ref. [25] gives the spin as 7/2⁺. For this work, it will be assumed the DWBA analysis is correct.

Similar experimental problems arise in the $d(^{48}Ca, {}^{49}Ca)p$ experiment. The measured total cross section in the S800 focal plane is low (see table I.10). Previous work with the $^{48}Ca(d, p\gamma)^{49}Ca$ reaction [26] has shown that there are low energy gamma rays that could have been observed, in particular a 659 keV transition from the decay of the 4.03 MeV state, and a 875 keV transition from the decay of the 4.89 MeV state. However, only gamma rays from the decay of the 2.02 MeV state were observed in the experiment. In the case of the 4.89 MeV state, the 875 keV transition was not observed, probably because, according to reference [24], the spectroscopic factor for that state is small. Also, unlike the ^{49}Sc case, the neutron separation energy of ^{49}Ca is relatively low; only 5.1 MeV [25]. Thus, levels populated in ^{49}Ca above 5.1 MeV will neutron decay and will not be detected with the present experimental setup. So, although significant single

particle strength has been observed to ^{49}Ca levels above the neutron threshold [23, 24], only those bound levels below the neutron threshold are relevant to this experiment.

TABLE II.4: JS Adiabatic Model Calculations for $d(^{48}Ca,^{49}Ca)p$ at 93.1 MeV/nucleon

^{49}Ca state	l-value	σ_{theory} (mb)	Avg. C^2S [#]	$\sigma_{calculated}$ (mb)
g.s.	1	0.059	0.86	0.051
2.02 MeV	1	0.020	0.99	0.020
3.59 MeV	3	0.18	0.14	0.025
3.99 MeV	3	0.17	0.92	0.16
4.03 MeV	4	1.6	0.26	0.42
4.07 MeV	1	0.015	0.13	0.002
4.26 MeV	1	0.0080	0.12	0.0001
Total				0.68
			Experimental σ_{tot}	0.6 ± 0.06

[#]Average of Spectroscopic factors from references [23, 24]

The adiabatic model calculations for $d(^{48}Ca,^{49}Ca)p$ are shown in table II.4. These show many features in common with ^{49}Sc. There is a reasonable agreement between the experimental cross section of $0.6\,\text{mb} \pm 0.06$ and the calculated cross section of 0.68 mb. Again, ^{49}Ca states with higher l-values are favored. This result is similar to the ^{49}Sc case, except that the states with higher l-values in ^{49}Ca are now excited states. In particular, the l=3 state at 3.99 MeV and the l=4 state at 4.03 MeV are responsible for a large part of the calculated cross section. However, the 659 keV transition from the decay of the 4.03 MeV excited state was not observed in this experiment due to the low statistics and low gamma ray detection efficiency of SeGA.

Calculations were also performed for the two exotic beam reactions $d(^{40}S,^{41}Cl)n$, and $d(^{42}S,^{43}Cl)n$. Several low-lying excited states were observed in each case, from gamma rays in coincidence with the detected residual nuclei in the S800 focal plane. The reaction calculations for these reactions are shown in tables II.5 and II.6.

The experimental cross sections for these reactions are of similar size, 0.55 ± 0.07 mb for $d(^{40}S,^{41}Cl)n$ and 0.62 ± 0.07 mb for $d(^{42}S,^{43}Cl)n$, since both reactions are expected to add a proton into the $1d_{3/2}$ orbital. They are similar also to those measured for $d(^{48}Ca,^{49}Sc)n$ and $d(^{48}Ca,^{49}Ca)p$ at these energies, suggesting that similar reaction

TABLE II.5: JS adiabatic calculations for $d(^{40}S,^{41}Cl)n$ at 92.4 MeV/nucleon.

^{41}Cl state[*]	*Assumed l-value*	σ_{theory} (mb)	Assumed C^2S [#]	$\sigma_{calculated}$ (mb)
g.s.	2	0.17	1	0.17
0.130 MeV	0	0.047	1	0.047
0.680 MeV	2 ($1d_{5/2}$ level)	0.20	1	0.20
0.680 MeV	3 ($1f_{7/2}$ level)	1.64	0.2	0.33

[#] These spectroscopic factors are adopted in the calculations and do not indicate measured values. See the discussion in the following paragraphs.

*Refs. [27, 28] suggest that the ground state of ^{41}Cl is actually the $s_{1/2}$ state and the 130 keV state is the $1d_{3/2}$ state. For the present work, it is assumed that the ^{40}S is highly deformed as in reference [29] and prolate. According to the Nilsson model, this would suggest that the $s_{1/2}$ level is already filled in ^{40}S and both the g.s. and 130 keV level would contribute to the total $d_{3/2}$ strength. Here, the 130 keV level is included as the $s_{1/2}$ state to illustrate that any contribution to the cross section from an $l=0$ is small compared to other state with higher l-values.

TABLE II.6 : JS adiabatic calculations for $d(^{42}S,^{43}Cl)n$ at 93.3 MeV/nucleon.

^{43}Cl state[*]	*Assumed l-value*	σ_{theory} (mb)	Assumed C^2S [#]	$\sigma_{calculated}$ (mb)
g.s. ($1d_{3/2}$)	2	0.16	1	0.16
g.s. ($1s_{1/2}$)	0	0.05	1	0.05
1.0 MeV	2 ($1d_{5/2}$ level)	0.19	1	0.19
1.0 MeV	3 ($1f_{7/2}$ level)	1.57	0.25	0.39

[#] These spectroscopic factors are adopted in the calculations and do not indicate measured values. See the discussion in the following paragraphs.

*Ref. [28] suggests that the ground state of ^{43}Cl is actually the $s_{1/2}$ state and the 330 keV state is the $1d_{3/2}$ state. For the present work, it is assumed that the ^{42}S is also highly deformed as in ref. [29] and prolate. According to the Nilsson model, this suggests that the $s_{1/2}$ level is already filled in ^{42}S and both the g.s. and 330 keV level would contribute to the total $d_{3/2}$ strength as suggested above for ^{41}Cl. Ref. [28] also suggests a $5/2^+$ level at around 1 MeV for ^{43}Cl. Two possible spin assignments are suggested for this level in the table for comparison of the cross sections calculated by the JS adiabatic model.

mechanisms are at work in the exotic beam reactions. Assuming that the ground and first excited states of both ^{41}Cl and ^{43}Cl arise from transfer of a proton to the *sd*-shell, the calculated cross sections are about a factor of 3 smaller than the measured values, even if the maximum spectroscopic factors are assumed. The calculated cross sections increase if a $1d_{5/2}$ level is included as an excited state, but it is unlikely that the spectroscopic factor for such a state would be as high as suggested in tables II.5 and II.6. If, on the other hand, an excited $1f_{7/2}$ level is included then the calculated cross section is too large. The high deformation of the ^{40}S and ^{42}S cores [29] may mean the $1f_{7/2}$ strength is fragmented and thus some of the spectroscopic strength from this shell may contribute as an excited state

in these reactions. Possible suggested values for the spectroscopic factors of the $1f_{7/2}$ excited state in ^{41}Cl and ^{43}Cl are also included in tables II.5 and II.6. Further experimental evidence of such $1f_{7/2}$ single particle strength in ^{41}Cl and ^{43}Cl will be needed but, in the absence of such a contribution, the calculated and experimental cross sections disagree.

In summary, adiabatic model transfer reaction calculations are able to reproduce the measured cross sections for $d(^{48}Ca,^{49}Sc)n$, $d(^{48}Ca,^{49}Ca)p$, $d(^{40}S,^{41}Cl)n$, and $d(^{42}S,^{43}Cl)n$ reasonably well. It is very clear that the basic linear and angular momentum matching of the transfer reaction mechanism at intermediate energies favors the population of single-particle states of high (orbital and) spin angular momentum. The detection of the outgoing proton and/or neutron from such reactions would allow comparisons with theory at the angular distribution level, and greater interrogation of the reaction mechanism and orbital angular momentum transfers. Such measurements, in inverse kinematics, would be challenging but would provide important insights for understanding the details of the spectroscopy suggested by the present data and analysis.

II. Eikonal Knockout Reaction Theory
A. Theoretical Description of Single-Nucleon Knockout Cross Sections

As was shown in Chapter 1, the inclusive cross sections for one-nucleon removal from the three beams used in the experiment are much larger than those for one nucleon pickup by the projectiles. As for these pickup reactions, adiabatic model calculations of one-nucleon transfer from the projectile to the target, i.e. the (d,t) or (d,^{3}He) reactions, also predict cross sections for these channels of order 1 mb at ~100 MeV/nucleon, whereas the experimental cross sections (see tables in section II) are in the range 40 to 125 mb. Thus, other nucleon-removal reaction mechanisms dominate at 100 MeV per nucleon.

Recently, an eikonal knockout reaction theory [30-35] has used to calculate inclusive and partial cross sections in one-nucleon removal reactions from stable and radioactive beams at intermediate energies. The approach assumes that the dominant nucleon removal mechanisms are (i) elastic breakup (also called diffraction dissociation) of the projectile, including (for targets with large Z) elastic breakup due to Coulomb interactions (Coulomb dissociation), and (ii) inelastic breakup or stripping of the nucleon

in an inelastic (absorptive) collision with the target. Coulomb dissociation of the projectile can certainly be neglected in the case of a deuteron target [30]. Thus, the total cross section for nucleon removal (the knockout cross section) involves both of these processes, that lead to distinct final states, and the measurements must be compared with

$$\sigma_{tot,c} = \sum C^2 S_c(l,j)[\sigma_{str} + \sigma_{el}].$$ (II.1)

Here $\sigma_{tot,c}$ is the total cross section for production of a bound, mass (A-1) residue. Thus, the sum must be taken over all bound final states of the residue and is weighted by $C^2 S_c$, the spectroscopic factor for each residue final state [35]. The calculation of the stripping (σ_{str}) and elastic breakup (σ_{el}) partial cross sections in the above [30, 35] requires a model calculation of the eikonal elastic S-matrices S_{cd} and S_{Nd} which describe the interactions between the core and the removed nucleon with the deuteron target, respectively. Given the loosely-bound composite nature of the deuteron target these are described as follows.

For the nucleon-deuteron system, we assume a complex, central Gaussian model interaction (V_{Nd}) of the form,

$$V_{Nd}(r) = -V_0 \exp(-r^2/r_V^2) - iW_0 \exp(-r^2/r_W^2).$$ (II.2)

Taking $V_0 = 21.0$ MeV, $r_V = 1.928$ fm, $W_0 = 12.0$ MeV, and $r_w = 1.764$ fm, the eikonal model calculation of S_{Nd} [36, 37] reproduces the measured total cross section for N+d scattering: $\sigma_{tot} = 101$ mb at 100 MeV/nucleon [38]. Moreover, the real and absorptive components of S_{Nd} are vital in determining the stripping and elastic breakup contributions to nucleon removal from the projectile by the deuteron. Note that the imaginary part of V_{Nd}, describing deuteron excitation (i.e. breakup), is entirely responsible for the stripping (target excitation) component. Thus these potential parameters were also chosen to reproduce the split of σ_{tot} between the N+d elastic (34 mb) and inelastic (67 mb) channels, as predicted by full three-nucleon calculations using the Bonn free NN interaction [39]. The V_{Nd} potential this provides a simple description of the nucleon-deuteron system that is consistent with both the refractive and the absorptive content of the best three-nucleon calculations. Having constrained V_{Nd} in this way, the calculations are rather insensitive to the details of the chosen geometry of the potential.

The core-deuteron interaction is constructed based on the core-neutron and core-proton two-body interactions, and described by their eikonal S-matrices S_{cn} and S_{cp} respectively. It then follows that the core-deuteron eikonal S-matrix is,

$$S_{cd}(b_{cd}) = \langle \phi_d | S_{cn}(b_{cn}) S_{cp}(b_{cp}) | \phi_d \rangle \tag{II.3}$$

and includes the additional absorption effects due to the elastic breakup of the deuteron target by the core. Here, as previously, ϕ_d is the deuteron ground state wave function which is calculated in a Woods-Saxon potential well with radius $R_0 = 1.25$ fm, diffuseness 0.55 fm, and with the depth adjusted to reproduce the deuteron separation energy of 2.225 MeV. This wave function is then also consistent with the empirical root mean squared (rms) neutron-proton separation.

The individual S_{cn} and S_{cp} S-matrices are calculated using the optical limit of Glauber's multiple scattering theory [37]. In each case, the interaction between the core and the nucleon is obtained by a folding of the core density with an energy and density independent Gaussian NN effective interaction [35, 40]. This has a range of 0.5 fm and a strength determined by (a) the free proton-proton and neutron-proton cross sections and (b) the real-to-imaginary ratios of the forward NN scattering amplitudes α_{pp} and α_{np}, as in [41]. The core densities are taken from spherical Hartree-Fock calculations, as were discussed in connection with the transfer reaction analysis. This approach has been used successfully previously to describe the core densities in many cases, e.g. [33].

B. Calculations for d(^{48}Ca,^{47}Ca+γ)X

Previous, low energy studies of the $^{48}Ca(d,t)^{47}Ca$ and $^{48}Ca(p,d)^{47}Ca$ reactions [42,43] have reported that the ground state of ^{47}Ca has a single neutron hole in the 1f$_{7/2}$ shell and the strongly populated excited states at around 2.6 MeV have a single neutron hole in the 1d$_{3/2}$ and 2s$_{1/2}$ shells respectively. The energy difference between the 1d$_{3/2}$ and the 2s$_{1/2}$ hole states is only 21 keV, and thus it is difficult to separate these states in a standard particle detection experiment at low energies. Nevertheless, the experiments that have been conducted so far have shown that the spectroscopic factors for the ground and low-lying excited states in ^{47}Ca approach their theoretical maxima. Previously reported spectroscopic factors for states in ^{47}Ca are listed in table II.7.

TABLE II.7: Spectroscopic Strengths for Single Neutron Hole States in ^{47}Ca

^{47}Ca state (MeV)[*]	C^2S	Reaction	Beam Energy	Reference
g.s. ($7/2^-$)	7.0	^{48}Ca(d,t)^{47}Ca	21.4 MeV	[42]
	6.7	^{48}Ca(p,d)^{47}Ca	40 MeV	[43]
2.58 ($3/2^+$)	2.5	^{48}Ca(d,t)^{47}Ca	21.4 MeV	[42]
	3.6	^{48}Ca(p,d)^{47}Ca	40 MeV	[43]
2.60 ($1/2^+$)	1.2	^{48}Ca(d,t)^{47}Ca	21.4 MeV	[42]
	1.8	^{48}Ca(p,d)^{47}Ca	40 MeV	[43]

* Energies and spin assignments taken from [43].

TABLE II.8: Eikonal Nucleon Knockout Calculation for $d(^{48}Ca,^{47}Ca)X$ at 93.1 MeV/nucleon

^{47}Ca state	σ_{str} (mb)	σ_{el} (mb)	Avg. C^2S [#]	$C^2S*(\sigma_{str}+\sigma_{el})$
g.s.	7.98	2.16	6.85	69.5
2.58 MeV	5.84	1.46	3.05	22.3
2.60 MeV	7.36	2.23	1.05	14.4
Total (mb)				106.2
			Experimental σ_{tot}	$125\,\text{mb}\pm14$

[#]Average of Spectroscopic factors from references [42, 43]

In the present work, the cross section for single nucleon knockout for $d(^{48}Ca,^{47}Ca+\gamma)X$ at 100 MeV/nucleon was large (125 ± 14 mb). As a result, the ^{47}Ca states populated in the reaction were observed directly with coincidences between the ^{47}Ca residual nuclei detected in the S800 focal plane and gamma rays from the decay of the ^{47}Ca excited states detected by SeGA. While the gamma decay of the first excited state of ^{47}Ca at 2.02 MeV ($3/2^-$) was observed in the spectrum, it is assumed that this gamma ray came exclusively from the decays of the two neutron hole states at 2.58 MeV and 2.60 MeV via the 564 keV and 586 keV gamma ray transitions also observed in the spectrum. The 2.58 MeV and 2.60 MeV excited states decaying through the first excited state at 2.02 MeV has been previously observed by analysis of the beta-decay of ^{47}K [44], and was confirmed in this work through $\gamma-\gamma$ coincidence analysis. A calculation of the total cross section for $d(^{48}Ca,^{47}Ca+\gamma)X$ at the mid-target energy of 93.1 MeV/nucleon is shown in table II.8. The agreement between the Eikonal model calculation in table 12 (106.2 mb) and the experimental cross section reported in table 2 ($125\,\text{mb}\pm14$) is quite reasonable.

C. Calculations for d(^{48}Ca,^{47}K+γ)X

Similar calculations to those carried out for the d(^{48}Ca,^{47}Ca+γ)X reaction were performed for the d(^{48}Ca,^{47}K+γ)X data. For these calculations, it was assumed that the ^{47}K products were populated via single proton knockout from the ^{48}Ca $2s_{1/2}$ and $1d_{3/2}$ levels. Spectroscopic factors from previous work at low energies for the ground and first excited state in ^{47}K are summarized in table II.9.

TABLE II.9: Spectroscopic Strengths for Single Proton Hole States in ^{47}K

^{47}K state (MeV)*	C^2S	Reaction	Beam Energy	Reference
g.s. (1/2$^+$)	1.55	^{48}Ca(d,^{3}He)^{47}Ca	79.2 MeV	[45]
	1.50	^{48}Ca(t,α)^{47}Ca	33 MeV	[46]
0.359 (3/2$^+$)	4.16	^{48}Ca(d,^{3}He)^{47}Ca	79.2 MeV	[45]
	3.88	^{48}Ca(t,α)^{47}Ca	33 MeV	[46]

 * Energies and spin assignments taken from [46]

In the present work, the cross section for d(^{48}Ca,^{47}K+γ)X was also relatively large (40 mb $\pm$ 4). Coincidences between ^{47}K events in the S800 focal plane and the gamma decays of the first excited state of ^{47}K at 359 keV were observed using SeGA. The Eikonal model calculation for d(^{48}Ca,^{47}K+γ)X is shown in Table II.10.

TABLE II.10: Eikonal Nucleon Knockout Calculation for d(^{48}Ca,^{47}K)X at 93.1 MeV/nucleon

^{47}K state	σ_{str} (mb)	σ_{el} (mb)	Avg. C^2S [#]	$C^2S*(\sigma_{str}+\sigma_{el})$
g.s.	5.79	1.59	1.53	11.3
0.359 MeV	4.80	1.08	4	23.5
Total (mb)				34.8
			Experimental σ_{tot}	40 $\pm$ 4

[#]Average of Spectroscopic factors from references [45,46]

The calculated cross section is again quite reasonable when compared with the measured cross section. However, as in ^{47}Ca, the $1d_{5/2}$ shell is highly fragmented into several excited states [45,46]. While the spectroscopic factors of several of these states are large, including these states in the calculation makes the calculation of the cross section too large. In addition, not including the $1d_{5/2}$ states is reasonable since the first 5/2$^+$ state is at 3.42 MeV, and there were no gamma ray transitions specifically from these states observed in the experiment.

D. Calculations for d(^{40}S,^{39}S+γ)X and d(^{42}S, ^{41}S+γ)X

In principle, the neutron knockout reactions involving the ^{40}S and ^{42}S exotic beams should be similar to the d(^{48}Ca,^{47}Ca)X case since all three reactions involve neutron removal from the $1f_{7/2}$, $1d_{3/2}$, and $2s_{1/2}$ shells. The only difference between the three beams for neutron knockout reactions, at first glance, is the number of neutrons in the $1f_{7/2}$ shell. However, ^{40}S and ^{42}S have been shown in experiments to be deformed nuclei [29], and the neutron separation energies are lower; 7.76 MeV for ^{40}S and 6.71 MeV for ^{42}S versus 9.45 MeV for ^{48}Ca [47]. Based on the eikonal model calculations for the ^{48}Ca nucleon knockout reactions, the lower neutron separation energies for ^{40}S and ^{42}S should lead to higher cross sections for neutron stripping and elastic breakup to the ^{39}S and ^{41}S ground states. As a first attempt at reproducing the experimental cross sections for these reactions, it is assumed that the spectroscopic factors are the

TABLE II.11: Eikonal Nucleon Knockout Calculation for d(^{40}S,^{39}S)X at 92.4 MeV/nucleon

^{39}S state	σ_{str} (mb)	σ_{el} (mb)	Assumed C^2S [#]	$C^2S*(\sigma_{str}+\sigma_{el})$
g.s.	9.57	2.61	4	48.72
1.0 MeV ($3/2^+$)*	7.71	2.01	4	38.88
2.0 MeV ($1/2^+$)*	9.48	2.96	2	24.88
Total (mb)				112.5

[#]Assumed spectroscopic factors from single particle shell model.
*Neutron-hole states taken from the positions of neutron hole states in ^{43}Ca [48]. See discussion in the following paragraphs.

TABLE II.12: Eikonal Nucleon Knockout Calculation for d(^{42}S,^{41}S)X at 93.3 MeV/nucleon

^{39}S state	σ_{str} (mb)	σ_{el} (mb)	Assumed C^2S [#]	$C^2S*(\sigma_{str}+\sigma_{el})$
g.s.	9.69	2.71	6	74.40
1.9 MeV ($3/2^+$)*	7.50	1.98	4	37.92
2.4 MeV ($1/2^+$)*	9.49	3.02	2	25.02
Total (mb)				137.3

[#]Assumed spectroscopic factors from single particle shell model.
*Neutron-hole states taken from the positions of neutron hole states in ^{45}Ca [49]. See discussion in the following paragraphs.

spectroscopic factors from the simple single particle shell model. In addition, since the level schemes of the residual nuclei are not well known, it is assumed that the neutron shell spacing between the $1f_{7/2}$, $1d_{3/2}$, and $2s_{1/2}$ levels is the same as in the nearest well-known nuclei with the same neutron numbers; namely ^{43}Ca [48] for ^{39}S and ^{45}Ca [49] for

^{41}S. The eikonal model calculations for $d(^{40}S, ^{39}S+\gamma)X$ and $d(^{42}S, ^{41}S+\gamma)X$ assuming the shell spacing in ^{43}Ca and ^{45}Ca are shown in tables II.11 and II.12.

Comparing the results of the calculations in tables II.11 and II.12 with the calculations for $d(^{48}Ca, ^{47}Ca)X$ in table II.8, the cross sections for neutron knockout from ^{40}S and ^{42}S should be about the same size or perhaps even larger than the ^{48}Ca neutron knockout cross section, and the cross section should be larger for the $d(^{42}S, ^{41}S)X$ reaction versus $d(^{40}S, ^{39}S)X$ reaction. However, the experimental results for the cross sections show that the $d(^{48}Ca, ^{47}Ca)X$ inclusive cross section was the largest (125 ± 14 mb) and the $d(^{40}S, ^{39}S)X$ (71 ± 8 mb) and $d(^{42}S, ^{41}S)X$ (69 ± 8 mb) were about 50% smaller and approximately the same size.

Several excited states were observed in ^{39}S and ^{41}S. While it was difficult to calculate the cross sections for the population of individual excited states due to the problems in determining the gamma ray detection efficiency mentioned earlier, it was possible to measure the parallel momentum distributions for events in coincidence with the gamma rays in the focal plane of the S800. Even with background subtraction, the parallel momentum distributions for the excited states were all remarkably similar for both ^{39}S and ^{41}S states and resembled previously published momentum distributions for $l=3$ momentum distributions shown in fig. 3 of ref. [34]. It has been suggested that the asymmetry of the parallel momentum distributions [34, 50] resulting in an extended "tail" at the low-energy end of the distribution may arise from several processes such as elastic scattering of the residual core on the target after the removal of the neutron, or perhaps from multi-step processes involving excitation of the beam into a low-lying excited state before the neutron is removed. Both of these processes, if included, would increase the cross sections already calculated. Thus, the difference between the calculations and the experimental results must arise either from an over-estimation of the spectroscopic factors, or a misunderstanding of how the knockout from the deformed shell structures of ^{39}S and ^{41}S contribute to the cross section.

To address the possibility of over-estimation of the spectroscopic factors, one notes that the average spectroscopic factors for $d(^{48}Ca, ^{47}Ca)X$ taken from previous experiments at low energy (table II.7) are all significantly lower than their theoretical maximums from the single particle shell model. The lower measurements are thought to

arise from spreading of the spectroscopic strength to higher excited states not observed in the experiment. Also, several recent publications [30, 33, 34, 50-52] have remarked that, in general, the eikonal model calculations with theoretically derived spectroscopic factors (single particle shell model or similar) are larger than the experimental cross sections because the spectroscopic factors are over-estimated due to the truncated model space model space used in the shell model calculations (i.e. only low-lying states are included in the model space), and incomplete treatment of the strongly repulsive core in the nucleon-nucleon interaction [33, 52]. This over-estimation of the spectroscopic factors results in a quenching factor R_s for comparing the calculated cross section to the experimental cross section defined as [33]:

$$R_s = \frac{\sigma_{inc}^{exp}}{\sigma_{inc}^{theory}} .$$ (4.7)

Typically, the quenching factor as measured in (e, $e'p$) and other nucleon knockout experiments from stable and well-bound nuclei is between 0.5 and 0.65 [30, 52]. In the present work, the quenching factors were 0.63 for $d(^{40}S,^{39}S)X$ and 0.50 for $d(^{42}S,^{41}S)X$. Thus, even though the experimental cross sections for $d(^{40}S,^{39}S)X$ and $d(^{42}S,^{41}S)X$ are approximately equal, they both have quenching factors that fall within the range of the previous knockout experiments. While more complex USD shell model or similar calculations may reduce the size of the spectroscopic factors used in these calculations and thereby improve the agreement between the calculations and the experiment, the question remains whether or not the quenching factors arise solely from the uncertainties in the shell model or from other effects not included in the calculations that may reduce the cross sections.

III. Discussion of Results and Summary

The JS adiabatic model proved useful in understanding the size of the (d,n) and (d,p) reaction cross sections. The model predicted the cross section of both single particle stripping reactions measured in this experiment within a factor of two. As a result, it showed that the two most important effects in determining the single-particle cross section are the size of the deuteron breakup contribution and the angular momentum matching between the transferred nucleon and open shell in the core nucleus. Thus, current accelerator facilities may be able to collect useful single particle spectroscopic

information for neutron rich f-p shell nuclei, which include single particle excited states in the $1f_{5/2}$ shell and $1g_{9/2}$ shells as in the ^{49}Ca case studied in this work.

The single nucleon knockout reactions measured on the liquid deuterium target were important tests for the Eikonal nucleon knockout reaction theory. Earlier studies of single nucleon knockout reactions have used heavier targets that were treated as black spheres in the analysis [e.g. 30-34, 50]. The deuterium target allowed Eikonal calculations with a more microscopic model, although it was found that the specific geometry of the system was unimportant when the final cross section size was calculated. With modifications of the target description to account for the nucleon-deuteron cross section differences, the cross sections for nucleon knockout were reasonably reproduced in the calculations. This result illustrates that the choice of target is not important when measuring properties of the beam nucleus in knockout experiments, provided that the target has a low proton number so that the Coulomb dissociation term in the model can be neglected. The subject of whether or not it is important that the target has bound excited states is still under debate, but certainly the single nucleon knockout cross sections can be reproduced with the Eikonal model with the loosely bound deuteron target as with the previously used ^{9}Be and ^{12}C targets.

Comparing the single particle stripping reactions (d,n) and (d,p) with the single nucleon knockout reactions at 100 MeV/nucleon reveals that the cross section for the (d,n) and (d,p) reactions is about 100 times smaller than that of the single nucleon knockout reactions. According to the cross sections presented in tables I.9 – I.12, it is much easier to remove even multiple nucleons from the beam nucleons than it is to add them. This result is expected because there are multiple mechanisms that can cause the removal of the nucleon from the beam, and knowledge of what happened to the removed nucleon after it was separated from the beam nucleus is not required in order to extract useful information from the residual core nucleus. The cross section for nucleon removal from the beam would be much smaller if one required, for example, that the knocked-out nucleon became bound to the deuteron in the target and that the resulting triton was detected. By the same argument, since there is only one mechanism that results in a nucleon being added to the beam nucleus as in the (d,n) and (d,p) reactions, the cross section for these reactions will be lower than for the knockout case. The cross section of

the nucleon pickup reactions is further impaired by whether or not the nucleon is properly matched in angular momentum to the open shell above the nuclear core of the beam. This limitation is not present in the nucleon knockout case because the size of the cross section only depends on how tightly bound the valence nucleon to the residual core.

The author would like to acknowledge the help of Jeff Tostevin in providing the computer codes TWOFNR for the JS adiabatic model calculations and the code for the Eikonal single nucleon knockout calculations. The calculations for the reaction cross sections presented in this dissertation were performed by the author. These results will published in future papers.

CHAPTER 3

UPGRADE TO OPPLIS AND POLARIZED BEAM STUDIES

I. Introduction

The scattering of polarized ions has been an area of experimental interest for several decades. Sources of the polarized protons, tritons (^{3}H), and ^{3}He have been available since the 1960s, and these spin-½ particles made possible experimental measurements of the nuclear spin-orbit force. Since that time, polarized sources for particles of higher spin have been developed, and the current focus of the research is on particles with nuclear spin=3/2 such as ^{7}Li. ^{7}Li nuclei are ideal for observations of internal projectile effects because the spin-orbit interaction between heavy-ions, like lithium, and a target nucleus has been shown, both theoretically and experimentally, to be weak [1]. A polarized ^{7}Li ($^7\vec{Li}$) beam also allows measurement of first order (spin-orbit), second order, and third order analyzing powers, which measure the tensor effects of the nuclear scattering potential. Detailed measurements of these observables can lead to determinations of the structure of a given target nucleus by uniquely identifying the spin and parity of the states in the nucleus. Also, the measurement of analyzing powers has revealed some of the reaction mechanisms that take place during the scattering of nuclei (e.g. reorientation of the ^{7}Li nucleus in elastic scattering [2]). Understanding of these reaction mechanisms for the scattering of loosely-bound stable nuclei like ^{7}Li may shed light on the reaction mechanisms involved in the scattering of loosely-bound exotic nuclei close to the neutron dripline [3].

This chapter reviews the author's work with the Florida State University (FSU) optically pumped polarized lithium ion source (OPPLIS) from May 2002 until May 2006. The focus of this work has been to increase the nuclear spin polarization of the $^7\vec{Li}$ beams produced by OPPLIS as measured on target during scattering experiments. Previously, typical $^7\vec{Li}$ beam polarizations were $t_{10}= 0.54 \pm 0.02$, or 40% of the maximum possible value for first rank polarization, $t_{20}= 0.60 \pm 0.03$, or 60% of the maximum possible value for second rank polarization and $t_{30}= 0.55 \pm 0.03$, or 41% of the maximum possible value for third rank polarization [4]. The maximum possible values for t_{10} ($\sqrt{(9/5)}$) and t_{20} (+1) (equation 1 in [5]) are obtained when all the ^{7}Li nuclei in the

beam are in the m_I=+3/2 substate (see section II.B). Similarly, the maximum possible value of t_{30} ($\sqrt{(9/5)}$) is obtained when all the ^{7}Li nuclei are in the m_I= −1/2 substate. While these beam polarizations are sufficient for the measurement of scattering reactions with large magnitude analyzing powers within a reasonable amount of time, they are insufficient for the accurate measurement of small magnitude analyzing powers. This is because the experimental errors in the analyzing powers decrease as the product of the *Polarization^2*Beam Current (P^2I)* increases [6]. Thus, improvements in the $^7\vec{Li}$ beam polarization and beam current output of OPPLIS will lead to faster, more precise measurements of the analyzing powers in $^7\vec{Li}$ scattering experiments.

II. Background information about OPPLIS
A. Spin polarization of a beam of nuclei, in particular, ^{7}Li

The FSU Optically Pumped Polarized Lithium Ion Source (OPPLIS) has been in operation since 1991 producing nuclear spin polarized ion beams of ^{6}Li and ^{7}Li. As shown by Mendez et al. [7], it was relatively easy to obtain a highly polarized beam of ^{6}Li using OPPLIS by the method of optical pumping. However, highly polarized ^{7}Li beams have been difficult in general to obtain, and typical values for ^{7}Li beam polarization were much lower than the beam polarization obtained for ^{6}Li [8]. This report details the recent upgrade to OPPLIS which includes the installation and testing of a new laser system to perform the optical pumping of the ^{7}Li atomic beam and on-target tests of the beam polarization.

In general, there are two commonly used ways to spin polarize an atomic beam of an alkali such as ^{6}Li, ^{7}Li or ^{23}Na: the Stern-Gerlach method and the optical pumping method. In the Stern-Gerlach method [e.g. 9], an atomic beam is passed through a region of non-uniform magnetic field generated by a multipole magnet, such as a six-pole magnet. The spin of the outermost atomic electron couples to the non-uniform magnetic field and a spatial separation is achieved between different spin substates states of the atomic beam. Then, nuclear polarization is produced from the polarized atomic beam using various radio frequency (rf) transitions to transfer some of the atoms from other hyperfine states into a specific hyperfine substate such as the F, m_F=2 substate with m_I=+3/2. The part of the beam with the desired substate is focused and then accelerated

for experiments, while the beam with the undesired substate is blocked or deflected away. However, the Stern-Gerlach method, has the following disadvantages. First, the Stern-Gerlach method plus rf transitions is capable of separating the ^{7}Li atoms into a single atomic magnetic substate m_F (see figure III.1). While this technique separates the ^{7}Li atoms into beams with good atomic polarization m_J, it produces states with mixed nuclear polarization m_I since $m_F=m_I+m_J$.   In particular, the atomic magnetic substates with $m_F=$ -1,0, and 1 are mixed because there are multiple values of m_I and m_J that mix to form each. Therefore, it is impossible to obtain a ^{7}Li beam with a pure nuclear polarization (all nuclei in the same m_I state) with this method. As a further consequence of being unable to separate the mixed nuclear spin substates, the first and third rank analyzing powers (and also the first and third rank beam polarizations) cannot be separated (see for example [5] where a $^7\vec{Li}$ beam with $m_I=+1/2$ is used to measure the analyzing powers iT_{31} and iT_{32}). So, a polarized ^{7}Li beam created with the Stern-Gerlach method is also unable to measure complete sets of analyzing powers. Another drawback is that the Stern-Gerlach method requires the atomic beam with the undesired electron polarization state to be blocked, thus decreasing the amount of beam current available for an experiment. Finally, the spatial separation between the different electron spin states is often quite small, making it difficult to separate out the atomic beam with the pure electron spin polarization.

Another method of polarizing an atomic beam is the method of optical pumping. The optical pumping method takes advantage of the hyperfine splitting of the valence level of the electron. The hyperfine interaction between the magnetic moments of the electron and the nucleus splits the pure electronic energy levels into two energy levels, each with coupled angular momentum $F=I_{nuclear}+J_{electron}$. In the optical pumping method, an electro-optically modulated and circularly polarized laser beam is used to excite the ^{7}Li atom from both the $2S_{1/2}$ hyperfine levels to the $2P_{1/2}$ levels while the atomic beam is subjected to a weak magnetic holding field (10 gauss). When the atom decays back to the $2S_{1/2}$ state by emitting a photon, it is again excited by the laser beam. This process continues until the atom reaches a state of maximum coupled angular momentum $m_F=F_{max.}$ In the case of ^{7}Li shown in fig. III.1, the atom in its ground state ($2S_{1/2}$) can be in either the F=1 or F=2 hyperfine level. If the atom is excited by a laser of wavelength 670.8nm electro-optically modulated at 402 MHz, then atoms in either of the $2S_{1/2}$

hyperfine levels are excited with the same laser beam to the $2P_{1/2}$ state and then spontaneously decay back to the $2S_{1/2}$ state. If the circular polarization of the laser light is σ^+ (right circular polarization), the laser induces a $\Delta m_F = +1$ transition of the electron, where m_F is the magnetic quantum number for the hyperfine interaction. Although the spontaneous decay to the $2S_{1/2}$ state can be $\Delta m_F = 0, \pm 1$, as the atoms go through successive cycles of excitation and decay, they eventually end up in the $2S_{1/2}$, F=2, $m_F =$ +2 hyperfine level, corresponding to the nuclear spin substate with $m_I =+3/2$ [10]. Finally, the atomic beam passes into a region of strong magnetic field (see figure III.3) where it is adiabatically transformed into a state where the nuclear polarization is uncoupled from the polarization of the atomic electron (see section II.B). Once the
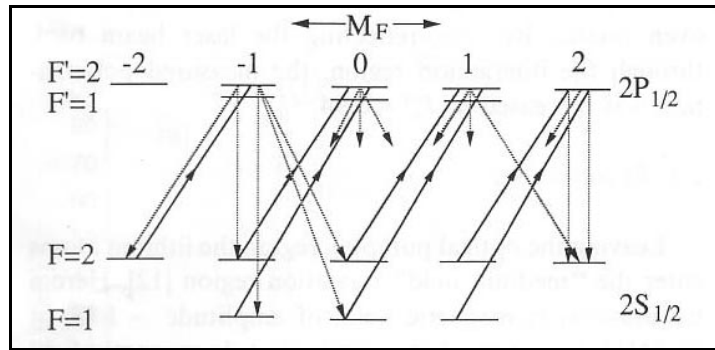
Figure III.1: Optical pumping of the ^{7}Li atom by a σ^+ laser beam [10]. The $2S_{1/2}$, F=1 and F=2 hyperfine states are separated by 804 MHz, and the $2S_{1/2}$ and $2P_{1/2}$ atomic energy levels are separated by about 1.85 eV. A laser with wavelength λ=670.9 nm and electro-optically modulated at 402 MHz optically pumps ^{7}Li atoms in either of the possible $2S_{1/2}$ hyperfine states, producing a $\Delta m_F = +1$ transition to the $2P_{1/2}$ state. After approximately four cycles of atomic excitation and decay, most of the atoms are in the F=2, m_F=2 hyperfine state [10].

nuclear polarization is uncoupled, the atom is ionized, producing a beam with, in principle, pure nuclear polarization. This method has the obvious advantage that most of the atomic beam is transferred into a single, pure, nuclear polarization state which allows all possible analyzing powers to be measured. In addition, there is no need to separate or block any of the atomic beam to filter out unwanted polarization states. The optical pumping method is the method used to polarize the lithium atomic beam in OPPLIS.

B. The FSU Optically Pumped Polarized Li Ion Source (OPPLIS): Previous Setup

The setup of OPPLIS prior to May 2002 is shown below in figure III.2. An argon ion laser (Coherent, Inc. I-200-10) was used to pump a dye laser (Coherent, Inc. 699-21)

to produce a laser beam with a wavelength of 670.8nm for optically pumping the lithium atomic beam. The Ar^+ ion laser and dye laser were housed in a separate, temperature controlled room. The laser beam was transported from the laser room to the ion source platform with 50m of fiber optic cable. After being collimated by the fiber optic coupling lens at the output of the fiber, the laser beam was split into two beams, one for polarization of the lithium atomic beam by optical pumping, and the other for atomic polarization measurement by laser-induced fluorescence (LIF). A more detailed explanation of the optics setup for OPPLIS prior to May 2002 is given by Mendez et al. [6].
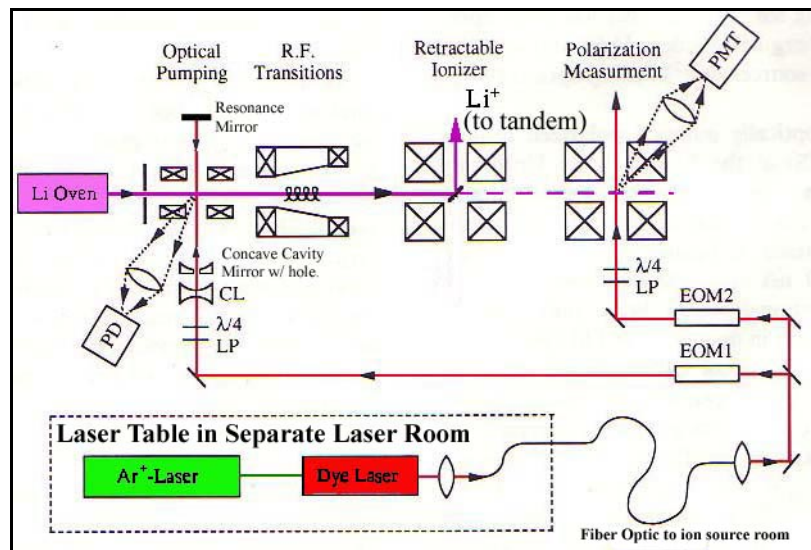
Figure III.2: Optics Setup for OPPLIS prior to May 2002. LP=linear polarizer, $\lambda/4$ = quarter wave plate, PMT= photomultiplier tube, CL = cylindrical lens, PD= photodiode, EOM= electro-optic modulator.

The previous optics setup (prior to May 2002) had the limitation that the maximum amount of laser power that could be transmitted through the fiber optic cable was about 65 mW. This was due to stimulated Brillouin scattering in the fiber optic cable; a non-linear process that caused a diminishing increase in output power for a given increase in the input laser power. In addition, the "home-made" electro-optic modulator (EOM1) used to electro-optically modulate the laser frequency (see section III.D) lowered the laser power available for optical pumping to about 40 mW. While this amount of laser power was sufficient to optically pump ^{6}Li atomic beam, it was in general not sufficient to optical pump the ^{7}Li atomic beam to a high degree of beam polarization (see section II.C).

The elements for steering and focusing the lithium beam into the FSU tandem-linac accelerator were not changed during the upgrade. The following describes the production of the lithium atomic beam in OPPLIS and the manipulation of that beam into a beam of Li^- ions suitable for acceleration by the FSU tandem-linac accelerator. An oven of lithium metal is heated to between 750° C and 800° C, causing the lithium to vaporize and produce a gas of atomic lithium. This gas is directed through a Laval nozzle as it leaves the oven, creating the lithium atomic beam. At this point, the atomic beam is polarized by the laser beam using the method of optical pumping described in the previous section. Next, the lithium atomic beam passes through a region where it undergoes radio-frequency (RF) "medium-field" transitions (MFT). In this region, the lithium atomic beam in the F=2, m_F=2 state can be transferred into other F, m_F polarization states, such as those corresponding $\frac{1}{2}^+$ or $\frac{1}{2}^-$ nuclear polarization states for ^7Li. Next, the atomic beam passes into a region of strong magnetic field where the atoms are adiabatically transformed from atoms with well-defined F, m_F hyperfine states to atoms with uncoupled nuclear and atomic polarizations that have definite values of $I_{nuclear}$, m_I and $J_{electron}$, m_J. This region of strong magnetic field surrounds a hot tungsten ionizer strip. As the atomic beam hits the hot tungsten ionizer strip, it ionized to Li^+. Since Li^+ is a Helium-like ion with a closed $1S_{1/2}$ atomic shell, there is no further hyperfine interaction between the atomic electrons and the ^7Li nucleus that can change the nuclear polarization. The Li^+ beam is then extracted from the ionizer strip by an extraction grid, and accelerated vertically into a spherical deflector by an electrostatic potential of 4.7 kV. After going around the spherical deflector, the Li^+ beam passes through the Cesium Charge Exchange Canal (CEC) where the Li^+ beam interacts with a cesium vapor. About 5% of the Li^+ beam gains two electrons and becomes Li^- beam that is accelerated by the tandem accelerator. Like the Li^+ ions, the Li^- beam is in a closed atomic shell configuration ($1S_{1/2}^2 2S_{1/2}^2$) with no net electronic angular momentum and thus no hyperfine interaction with the polarized lithium nucleus. The remaining elements of the ion source are for steering and focusing the Li^- beam, except for the Wien filter spin precessor. The Wien filter uses a uniform magnetic field to precess the beam polarization (Larmor precession) direction so that after acceleration the beam has the desired polarization direction. The elements in the OPPLIS beamline are shown in figure III.4.
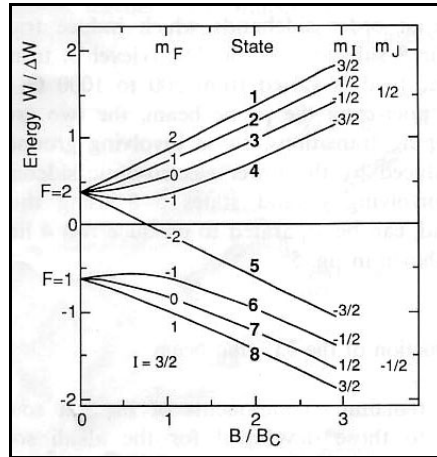
Figure III.3: Breit-Rabi diagram for atoms with $I=3/2$, such as ^{7}Li. At weak magnetic field (10 G), the atoms are well-defined hyperfine states with definite F, m_F. Once the atoms are optically-pumped into a single F, m_F state, the atoms can be transferred to other F, m_F states with radio frequency (RF) transitions at slightly higher magnetic field (around 30 G). Finally, the atoms pass into a region of strong magnetic field ($B/B_C > 1$, where $B_C = 287$ G for ^{7}Li) where the nuclear and atomic spin substates are uncoupled. At this point, the ^{7}Li atom is ionized to Li$^+$, producing a Helium-like ion with definite nuclear polarization I, m_I [10].
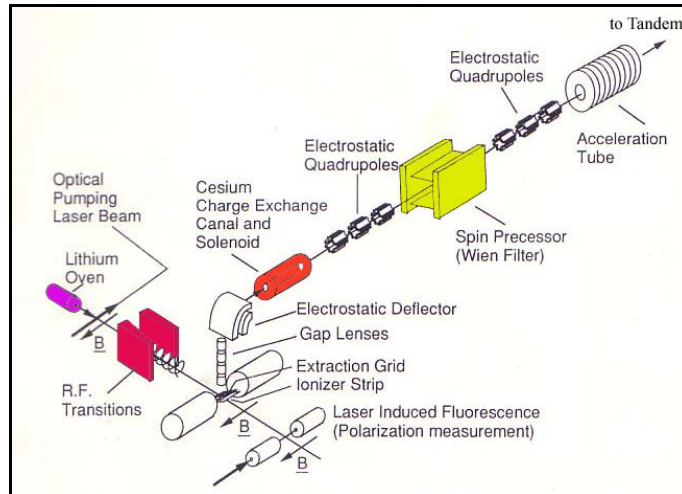
Figure III.4: Beam focusing elements of OPPLIS.

C. Reasons and goals for the upgrade to OPPLIS

An upgrade of OPPLIS was necessary for the following reasons. First, the on-target beam polarizations of $t_{10} = 0.54 \pm 0.03$, $t_{20} = 0.60 \pm 0.03$ and $t_{30} = 0.55 \pm 0.03$ [5] for ^{7}Li needed to be increased to improve the quality of experimental data. In fact, some experiments involving the measurement of small analyzing powers could not be performed in a reasonable amount of time (~2 wks.) unless the polarization was

84

improved. On-target first-rank beam polarization ratios for ^{7}Li had been seen in the past as high as $t_{10} = 0.95 \pm 0.08$ for short periods of time [11], but performing experiments requires easily attained high beam polarization that remains stable for long periods of time. Another reason for the upgrade is that the Ar$^+$ ion laser gas tube is very expensive to replace if it ever should break, not to mention that the Ar$^+$ ion laser itself is sometimes difficult to stabilize.

The factors required to improve the beam polarization of ^{7}Li are believed to be the amount of laser power available for optical pumping, the geometry of the laser-atomic beam overlap such that the horizontal divergence and vertical extent of the atomic beam is matched to the horizontal divergence and vertical extent of the laser beam in the optical pumping region, the temperature and surface condition of the ionizer strip, the uniform magnetic field strength of the Wien Filter. The goal of the OPPLIS upgrade was to remove the constraints on laser power and ionizer temperature from the previous source setup, and to try to improve the reproducibility of obtaining good beam polarization.

In principle, if the ^{7}Li atomic beam is well-collimated and the laser beam has negligible divergence at the optical pumping region, a relatively small amount of laser power is required to polarize the ^{7}Li atomic beam. A lower-limit to the amount of laser power P needed to polarize a given flux of atomic beam Φ is [10]:

$$P = \Phi \cdot n_p \cdot E$$

where E is the quantum energy of the photon required to excite the ^{7}Li atomic beam in eV, the laser power P is given in mW and the atomic beam current is given in particle-mA. Assuming four photons ($n_p = 4$) are needed on average to polarize each lithium atom, about $130 \, \text{particle-} \mu\text{A}$ of Li beam can be polarized per mW of laser power under these ideal conditions. However, the lithium atomic beam begins to diverge immediately after exiting the lithium oven described in section II.B. This divergence lowers the density of the atomic beam and only a small amount of fraction of the laser power is actually absorbed. The absorption of the laser beam by the ^{7}Li atomic beam was studied in detail by Myers and Mendez [10,12]. Mendez showed that with 40 mW of laser power in a non-divergent beam pumping a non-divergent ^{7}Li atomic beam, a beam with nearly all the atoms populating the F=2, m_F=2 state could easily be produced, as expected. However, once the atomic beam is allowed to diverge slightly as it does in OPPLIS, the number of

atoms pumped into the F=2, m_F=2 state for the same laser power was reduced to about 25% of the atoms in the beam, with the other atoms populating the other seven possible hyperfine states. By properly matching the laser divergence to the atomic beam divergence with a cylindrical lens such that atoms with different trajectories are all able to intersect the atomic beam at right angles. With 40 mW of laser power Mendez [12] showed that approximately 60% of the [7]Li atoms in the beam would populate the F=2, m_F=2 state, and other atoms would populate other states. This would result in a polarized beam of [7]Li atoms with nuclear vector polarization of t_{10}= 0.998, or 74% of the maximum possible value. Thus, according to this simulation, additional laser power would be needed in order to completely polarize a slightly divergent [7]Li atomic beam. Further details on simulations of the optical pumping of the [7]Li atomic beam can be found in [10,12].

The purpose of the upgrade to OPPLIS described in the following sections was to remove the limitation of the fiber-optic cable on the available laser power and thus allow an experimental determination of the optimum amount of laser power needed to produce a fully-polarized lithium atomic beam, accounting for the divergence of the atomic beam. The upgrade increased the amount of laser power available for optical pumping from around 40 mW to about 200 mW. It is important to note, however, that more laser power alone does not increase the atomic polarization. Proper adjustment of the laser beam divergence to match the divergence of the [7]Li atomic beam is essential to obtaining an atomic beam in a pure F, m_F hyperfine state. Another important consideration with higher laser power is to consider that additional scattered light from surfaces around the optical pumping region may depolarize the atomic beam after it is initially polarized, since laser light scattered from these surfaces is not properly circularly polarized. The improvements to the laser optics setup described in section IV.C undertaken to increase the polarization of the atomic beam were taken with these considerations in mind.

III. Upgrades to OPPLIS

A. The Verdi V-5 Diode Pumped Laser

The diode-pumped Verdi V-5 laser (Coherent Inc.) is a frequency doubled Neodymium Yttrium Vanadate (Nd:YVO$_4$) laser capable of providing a stable laser

output of between 0.01 W and 5 W at a wavelength of 532 nm. These specifications, in addition to its compact size and ease of operation, make it a suitable and necessary replacement for the Ar^+ ion laser as the "pump" laser for the dye laser.

The Verdi laser was installed as shown in figure III.5 in May 2002. The laser was mounted on a 3 ft by 4 ft vibration canceling laser table. The laser table was contained within a small clean room with a clean air filter near OPPLIS. There were two tests conducted to test its operation. The first was to determine if the passive heat sink that the laser head was mounted on was adequate for dispersing the heat generated by the laser head while it was on. The laser power was increased by 0.5 W every 10 minutes and then was allowed to run for 30 minutes at 4 W output power. If the heat sink was inadequate, the laser head would become warm to the touch in a short period. This heating of the laser head was not observed during the test however, so the passive heat sink suffices to keep the laser head from over-heating. The other test conducted on the Verdi laser was a power stability test to make sure the output laser power was stable over long periods of time. In this test, the laser was set to a specific value on the controller and a laser power meter measured the laser beam output power. At the same time, the current used to power the laser diode in the power supply/controller for the Verdi laser was also monitored. Fluctuating amounts of current needed for the laser diode would indicate a problem with the controller or the laser diode itself. No fluctuations above the resolution of power meter (± in the laser power output were observed on the laser power meter at laser power outputs up to 4 W over the course of 20 minute tests, and the laser diode supply current was also stable at each power setting.

The manual for the Verdi laser indicates that an increase in the amount of laser diode supply current needed to produce a given amount of output laser power from the Verdi laser indicates that the laser diode may have to be replaced [13]. Thus, for future reference, a graph of laser diode supply current vs. output laser power from the above tests is shown in figure III.6. At no time during the operation of the Verdi laser over the past year has the laser diode supply current been greater than 20 A, although the manual for the Verdi laser suggests this current will increase when the laser diode begins to deteriorate.
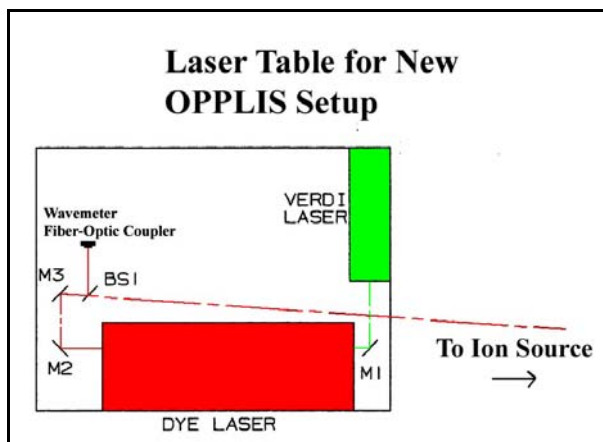
Figure III.5: Setup of the laser table in ion source room near OPPLIS. The laser table was completely contained within a small clean room with a clean-air filter. The dye laser beam was passed to OPPLIS through a small hole in the plastic surrounding the clean room.
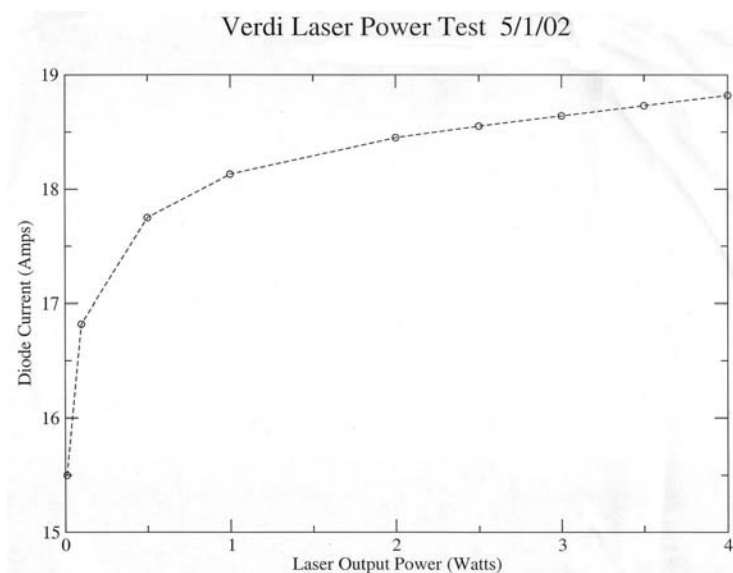
Figure III.6: Laser diode current vs. laser power output for the Verdi V-5 laser. The dashed line between points is to guide the eye. Deviations from this curve may signal that the laser diode is deteriorating.

B. Installation of the dye laser

Once the Verdi laser was successfully installed and tested, the dye laser from the previous source setup was moved from the separate laser room into the ion source room and mounted on the same laser table as the Verdi laser as shown in figure III.5. The laser cavity of the dye laser consists of four mirrors that must be aligned so that a laser beam can circulate around the cavity and come back on itself while passing through the various small apertures and the center of the dye jet. The pump beam from the Verdi V-5 laser must also be aligned and focused onto the dye jet as it overlaps the dye laser beam in the

88

dye jet. Once properly tuned, the dye laser produces the single frequency laser light with wavelength 670.9 nm needed to optically pump the lithium atomic beam.

Assuming the laser table is level, the height of the "pump" laser beam as it emerges from the Verdi laser is 11.88 cm above the table. The dye laser was positioned and aligned such that a mirror reflected the "pump" laser beam from the Verdi laser 90 degrees directly into the input of the dye laser, keeping the height of the "pump" laser beam above the table a constant. In theory, this allows the "pump" beam to reflect off of mirrors inside the dye laser, exciting the dye and generating the dye laser beam with a wavelength of 670.8nm. However, in practice getting the dye laser to lase initially was rather difficult. The mirrors that make up the dye ring laser cavity must be precisely aligned in order for the dye laser to lase. A procedure for aligning these mirrors is outlined in the dye laser manual, but it is difficult to follow. With the help of Ed Myers and after several hours of work, the mirrors were properly aligned and the dye laser was operational.

Once initially aligned, the mirrors in the dye laser should not have to be realigned to the extent they were in the installation of the dye laser. However, with the varying humidity and temperature of the climate in Tallahassee, as well as changes in the mirror alignment caused by heating from the "pump" and dye laser beams, the dye laser does need to be tuned from time to time. Usually, the power improves significantly if the input mirror and the output coupling mirrors are adjusted with the tuning knobs on the dye laser. If the dye laser does not lase initially after being pumped by 4 W of laser power when first turning it on and using the procedure suggested in Appendix A, the most likely reason that the dye laser is not lasing is that the output coupler mirror is slightly misaligned. A procedure for fixing this problem is outlined in Appendix A.IV.

C. Optics Setup

The new optics setup for OPPLIS is shown in figures III.7 and III.8. Using mirrors, the 670.9 nm laser beam output from the dye laser is reflected 180° on the laser table towards a beam splitter. This beam splitter samples a small amount of the laser beam for a wavelength measurement by a wavemeter on the laser table. The rest of the laser beam continues toward the ion source where it is reflected by a mirror mounted on one of the legs of the ion source towards the optics setup of the previous ion source setup.
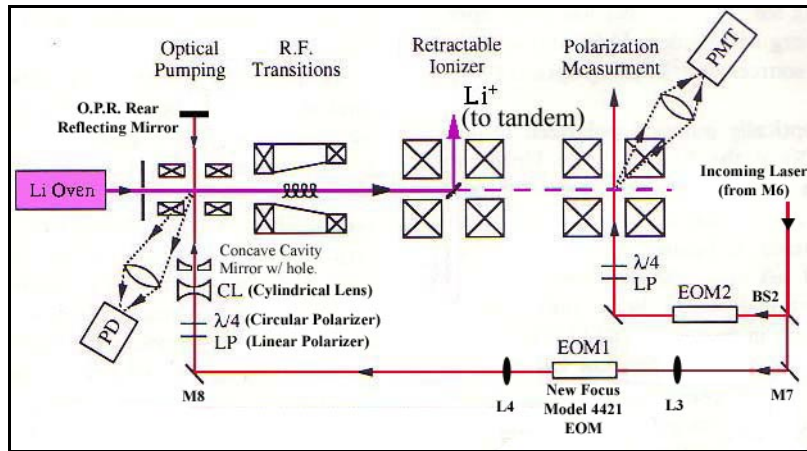
Figure III.7: Close-up of laser optics leading to optical pumping region in OPPLIS
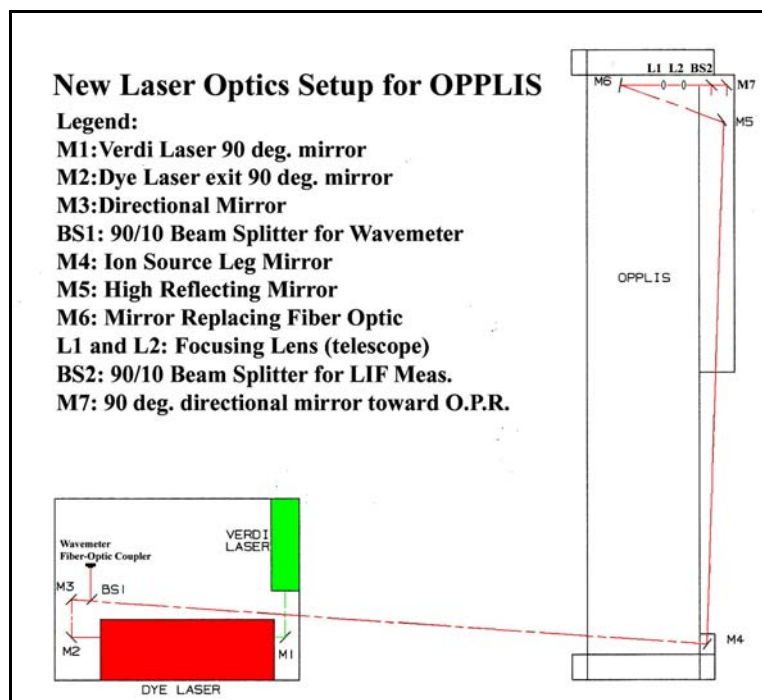
Figure III.8: Laser optics for new OPPLIS setup.

This mirror was placed at 96.2 cm above the floor of the ion source room. The laser then hits the high reflecting mirror, which steers the laser beam to another mirror placed in the position of the fiber optic in the previous source setup. Finally, the laser is refocused using a pair of lenses and then is introduced into the laser optics from the previous OPPLIS source setup. The optics setup of OPPLIS around the optical pumping region (O.P.R.) from the previous source setup is mostly unchanged, except that the focusing

90

lenses were repositioned to produce the proper divergence of the laser beam as described in section IV.C and a new electro-optic modulator (EOM) was installed in the position of EOM1.

D. The New Focus Model 4421 High Frequency Electro-Optic Phase Modulator (EOM1).

In order to account for the hyperfine splitting between the $2S_{1/2}$ atomic levels in ^{7}Li shown in figures III.1 and III.3, the atomic beam must be optically pumped at two slightly different frequencies, 804 MHz apart. To accomplish this, the laser beam is electro-optically modulated at half the $2S_{1/2}$ hyperfine splitting (402 MHz), causing the first-order frequency sidebands to match the frequency of the hyperfine splitting and allowing the same laser beam to optically pump both hyperfine levels.

The electro-optic phase modulator (EOM) in the previous setup for OPPLIS used for splitting the dye laser beam into the two beams, 804 MHz apart in frequency, is damaged when more than 100 mW of laser power is passed through the crystal in it due to the photorefractive effect. Thus, this EOM was replaced to remove this constraint on the laser power available for optical pumping.

The new EOM for OPPLIS is the New Focus model 4421 High-Frequency Electro-Optic Phase Modulator. This EOM has a crystal of magnesium oxide doped lithium niobate (MgO:LiNbO$_3$) housed in a resonant cavity. The magnesium oxide doping in the crystal in the New Focus EOM prevents damage from the photorefractive effect as long as the laser beam intensity is below 5 W/mm^2 and the wavelength is longer than 600nm [14]. As the maximum input laser power into the new EOM is about 300 mW for a 1mm^2 beam, and the wavelength is 670.8 nm, these limits are not approached with the new laser and optics setup for OPPLIS. The resonant cavity housing is necessary because the larger size of the crystal requires a higher radio frequency (rf) voltage to induce the change in the refractive index. The resonant cavity is of dimensions such that its resonant frequency is equal to that of the frequency of the input rf signal. Thus, a relatively low amount of input rf power can be converted into the high amplitude electric field needed for the crystal to modulate the laser beam frequency.

Implementation of the new EOM into OPPLIS was a long process that took several months from 6/2002 until 6/2003. There were several problems that needed to be overcome before a final working procedure could be established.

1. Setup of the radio-frequency (rf) circuit for driving the EOM resonant cavity

The setup of the rf circuit for driving the EOM resonant cavity is shown in figure III.9. It is essentially identical to the setup for driving the original "home-made" EOM in the previous setup, except that a Voltage-Controlled Oscillator (VCO) replaced the previous crystal oscillator, and the Hewlett-Packard 1 dB step attenuator was replaced by a Kay Elemetrics Model 1/837 rf attenuator capable of producing attenuations in steps of 0.1 dB, allowing a precise amount of rf power to be used for driving the EOM resonant cavity.
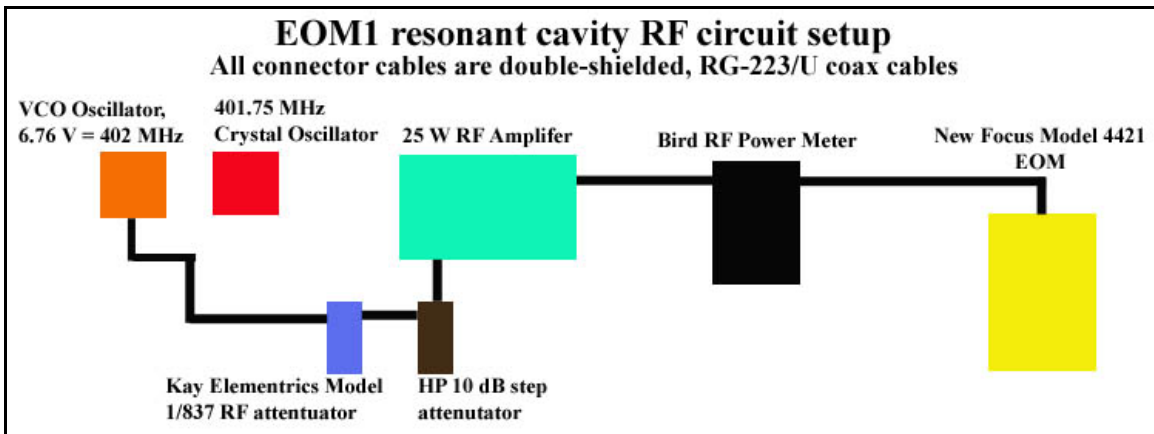
Figure III.9: Electronics setup for new EOM1

2. Tests of the New Focus EOM

The following describes the different tests that are used to determine if the new EOM is working properly.

The first and most common type of test is the **rf power meter test**. In this test, an rf power meter is placed between the rf amplifier and the EOM resonant cavity as shown in figure III.9. The rf power meter measures the rf power going forward into the cavity through the cable, and the reflected power coming back out of the cavity. If the forward rf signal matches the resonant frequency for the cavity, all the rf power efficiently excites the electric field inside the resonant cavity and very little rf power is reflected back to the power meter. However, if the signal does not exactly match the resonant frequency, rf

power will be reflected into the cable and the amplitude of the electric field inside the cavity will be greatly reduced. A lower depth of phase modulation for the laser beam results and consequently the 1st order side bands in the laser frequency are reduced, decreasing the efficiency of the optical pumping of the atomic pumping. Thus, this test can be used to ensure the rf signal is properly matched to the resonant cavity.

Another test is the **spectrum analyzer test**. The spectrum analyzer can sample the laser beam and display the frequency components of the beam. It is usually placed after the output of the EOM crystal in order to test if the laser beam is actually being phase modulated. Under ideal conditions, the EOM will transfer 70% of the laser power at the central, carrier frequency into the 1st and 2nd order frequency side bands. The transfer into the first order sidebands is used for effective optical pumping of the lithium atomic beam, as this produces the two laser frequencies 804 MHz apart to pump the $2S_{1/2}$ hyperfine levels of the lithium atom.

The last test was the **frequency generator test**. If the two previous tests of the EOM fail to produce modulation of the laser beam, there are three possibilities. First, the EOM itself could be damaged. Second, the radio frequency being input into the EOM does not match the EOM resonant cavity frequency. Or, third, the cavity itself might be grossly mistuned so that even though the VCO or crystal rf oscillator might be at the proper frequency, the cavity itself is not of the proper dimensions to oscillate. The frequency generator test was used to deal with possibilities 2 and 3. In this test, the VCO rf source is replaced by a frequency generator and the output frequency is measured by a high speed oscilloscope. Once the output frequency has been determined, the signal from the generator is connected to the rf amplifier circuit shown in figure III.9 to be tested on the resonant cavity. Using this test at the same time as the rf power meter and spectrum analyzer test can thus determine if the EOM is actually modulating the laser beam and also the resonant frequency of EOM resonant cavity. If that resonant frequency is found to be too high or low, then the cavity can be adjusted back to the range of frequencies accessible to the VCO or crystal oscillators.

3. Getting the new EOM to work properly

The New Focus Model 4421 EOM is at times difficult to work with because its operation depends on the stability of the rf resonant cavity that houses the EOM crystal.

The cavity can become unstable because driving the cavity at high input rf power causes heating of the electronics inside the cavity, causing the cavity to expand and thus changing its resonant frequency. If the cavity is allowed to expand too much, the resulting change in the resonant frequency of the cavity will lower the electric field inside the cavity and thus lower the efficiency of the laser beam phase modulation. Proper tuning of the resonant cavity is achieved when the forward rf power going into the cavity is around 2.6 W and the reflected power from the cavity is less about 0.030 W. The reflected power as measured by the rf power meter should not change much once the cavity is stable.

Stabilizing the rf resonant cavity involved replacing the crystal oscillator used for driving the old EOM with a Mini-Circuits ZOS-535 Voltage Controlled Oscillator (VCO). The rf frequency of this oscillator can be tuned between 300 MHz and 520 MHz using a DC voltage input. This allows the rf driving frequency of the EOM to be changed as the EOM heats up and its resonant frequency changes. Since the resonant frequency of the cavity changes on the order of ± 2 MHz as it heats up and expands, adjusting the input rf frequency by adjusting the DC input voltage on the VCO allows the EOM cavity to be stabilized easily on its resonant frequency. This method also has the advantage that the tuning screw on top of the EOM cavity does not need to be adjusted. However, the rf frequency spectrum of the VCO is somewhat more broad than that of the crystal oscillator, resulting in a reflected power of 0.030 W at 2.7 W of input rf power. This amount of reflected power does not affect the frequency modulation of the laser beam. However, it was found that the frequency of the resonant cavity also drifted over time using this method due to the heating of the cavity electronics. This problem was fixed with the addition of a cooling fan mounted behind the EOM cavity.

An rf input power of about 2.6 W produces the desired frequency modulation of the laser beam if the resonant cavity of the EOM is properly tuned and stabilized. Ideally, the 0th order frequency peak should be about the same height as the second order frequency peaks as measured by the spectrum analyzer. This depth of phase modulation produces the most laser power in the 1st order frequency peaks, which are 804 MHz apart in frequency. Thus, the laser power in the 1st order frequency peaks is of the proper

frequency separation to pump both $2S_{1/2}$ hyperfine levels of the ^{7}Li atomic beam. If this is true, then the EOM is working properly.

The current setup for the EOM electronics could be improved by setting up a self-excited loop circuit to drive the EOM. In this way, the radio frequency driving the cavity would be actively stabilized to account for the change in the cavity's resonant frequency due to the heating of the cavity electronics.

IV. Measuring and Optimizing the ^{7}Li on-target beam polarization
A. Measuring the on-target beam polarization

The reaction $p(^7Li, \alpha)\alpha$ is the reaction commonly chosen to monitor the ^{7}Li on-target beam polarization because of its large cross section and analyzing powers. Zupranski et al. showed that at $\theta_{lab} = 0°$, the only non-zero analyzing power is $T_{20} = -1$. This value for T_{20} at $\theta_{lab} = 0°$ holds at all energies by angular momentum conservation [15]. However, placing a detector at $0°$ is usually not done because the detector quickly becomes radiation damaged from the neutrons produced at $0°$ when the beam stops in the tantalum foil placed in front of the detector (the alpha particles from the reaction require more stopping power than the ^{7}Li beam, and thus they would pass through the tantulum foil while beam is stopped. Later, Tungate et al. showed that with the Zupranski result and data for the inverse reaction from $^7Li(p, \alpha)\alpha$ with polarized protons from Plattner et al. [16] that the first rank analyzing power $^TT_{10}$ approaches +1 for the reaction $p(^7Li, \alpha)\alpha$ at 42 MeV and $\theta_{cm} = 45°$ [17]. This center of mass angle corresponds to $\theta_{lab} = 19.6°$. Using this information, the ^{7}Li beam polarization t_{10} can be determined using the following equation:

$$t_{10}^{3/2} = \left(\frac{-9}{5\ ^TT_{10}} \right) \left(\frac{1}{\sum\limits_{-3/2}^{3/2} Y_i} \left(2Y_{3/2} + \frac{4}{3}Y_{1/2} + \frac{2}{3}Y_{-1/2} \right) - 1 \right) \tag{IV.1}$$

where "Y_i" is the experimental yield measured from a nuclear reaction with the polarized ^{7}Li beam in polarization state "i" [18].

For the tests of the new OPPLIS setup, the ^{7}Li beam was accelerated by the FSU tandem-linac accelerator to an energy of 42 MeV. This beam was impinged on a plastic polyethylene (CH$_2$) target made from a Ziploc freezer bag with thickness of about 500 $\mu g / cm^2$. The target was mounted in the FSU 85cm scattering chamber (fig. III.10) and kept at high vacuum (about 10^{-6} torr). A silicon ΔE-E counter telescope was placed at θ_{lab}=19.6° on the right side of the chamber to detect the α – particle products from the $p(^7Li,\alpha)\alpha$ reaction. Since all four spin polarization states of the ^{7}Li beam were produced by OPPLIS during the test, equation IV.1 was then used to determine the beam polarization t_{10} assuming $^TT_{10} = 0.91 \pm 0.07$ at this lab angle for this reaction. This value of $^TT_{10}$ was taken from a previous, unpublished measurement [19].
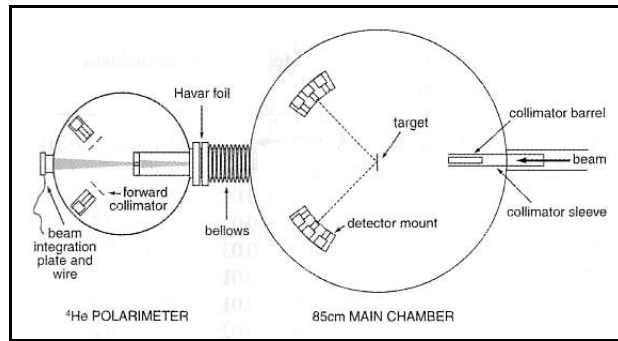
Figure III.10: 85cm scattering chamber setup for tests of OPPLIS.

B. The first test of the new setup, 8/8/03

The first test of the new OPPLIS setup was performed on 8/8/03 with the settings for the polarized source shown in Table III.1. The optimized settings for the ionizer strip 90 degree magnet, cesium charge exchange cell magnetic holding field current, and the cesium charge exchange cell center temperature in this table were determined by Peter Green in a similar, previous test experiment using the previous ion source setup [20]. The forward rf power for the new EOM1 was determined with the spectrum analyzer test mentioned in section III.D to optimize the phase modulation of the laser beam.

For this test, the Wien Filter magnetic field current was varied from 600mA – 690mA to verify that it was at the optimum value to compensate for the Larmor spin rotations the beam experiences as it travels through the accelerator magnets. Then, when

the optimum value of the Wien Filter magnetic field was found, the ionizer strip current was varied to see if making the ionizer strip hotter affected the on-target polarization. Finally, the laser power available for optical pumping was varied from 30mW to 105mW to investigate the effect this would have on the on-target polarization. A typical run

TABLE III.1: OPPLIS Source Parameters for test experiment 1 on 8/8/03

OPPLIS Source Parameter	Value Used
Tungsten ionizer strip 90 degree magnet current	8.90 A
Cesium charge exchange magnetic holding field current	50 A
Cesium charge exchange cell center temperature	150° C
Forward rf power into EOM1	2.6 W at 402 MHz (VCO oscillator)
Voltage drop across VCO	6.76 V (402 MHz)
Tungsten ionizer strip current/temp control	Varied from 120A to 140A (on supply)
Laser power at optical pumping region	Varied from 25mW to 105mW

during this test lasted about 20 minutes. During these runs, measurements for the unpolarized beam and all four polarization states of the ^{7}Li beam were cycled through 2 times, spending about 2 minutes in each polarization state. At the end of each run, the yields of the $\alpha -$ particle peak were recorded for each polarization state and the value for t_{10} and the ratio of the 3/2$^-$ polarization state yield to the 3/2$^+$ state polarization state were calculated. The results are shown in table III.2 and figures III.11 and III.12.

TABLE III.2: Optimized OPPLIS parameters for low polarization exp. 8/8/03

Optimized Wien filter magnetic current = **660mA** (in run 241)

unp yield	3/2$^+$	½$^+$	½$^-$	3/2$^-$	t_{10}	3/2$^-$/3/2$^+$
2288	1198	1573	2084	3028	0.5 ± 0.04	2.53 ± 0.09

Optimized Ionizer Strip Current = **120 A** (in run 249)

unp yield	3/2$^+$	½$^+$	½$^-$	3/2$^-$	t_{10}	3/2$^-$/3/2$^+$
942	481	709	845	1264	0.51 ± 0.04	2.62 ± 0.14

Optimized laser power input at optical pumping region = **35 mW** (in run 251)

unp yield	3/2$^+$	½$^+$	½$^-$	3/2$^-$	t_{10}	3/2$^-$/3/2$^+$
834	375	596	754	1190	0.59 ± 0.05	3.17 ± 0.19

Test of Effect of Ionizer Current/Temperature on beam polarization
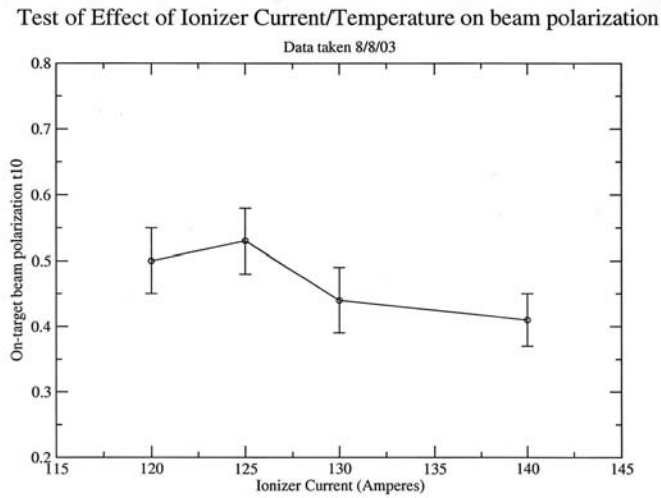
Figure III.11: On-target beam polarization vs. ionizer current for the first test experiment.

Test of Effect of laser power on beam polarization
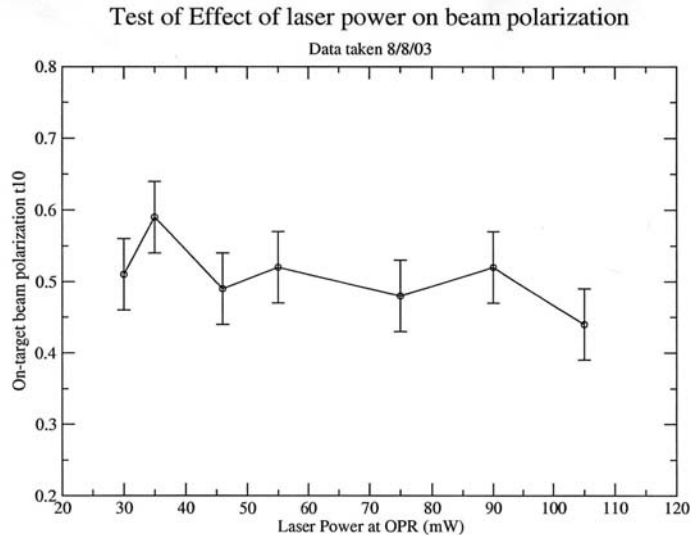
Figure III.12: On-target beam polarization vs. laser power.

The results shown in figure III.11 indicate that raising the temperature of the tungsten ionizer strip in OPPLIS did not improve the on-target beam polarization and actually made the on-target beam polarization worse. The reason for this is because the higher temperature of the ionizer strip evaporates lithium condensed on the walls of the ionizer box and becomes part of the ionized beam when it hits the ionizer strip. This evaporated lithium is unpolarized, and contributes to lowering the total polarization of the beam. At 120 A, the ionizer is still hot enough to ionize the ^{7}Li atomic beam effectively, but is cool enough not to evaporate a significant amount of unpolarized beam from the

walls of the ionizer box. Thus, this current setting was seen to be the optimized setting for the tungsten ionizer strip.

The results shown in figure III.12 suggest that increasing the amount of laser power at the optical pumping region also did not improve the on-target beam polarization and made the beam polarization worse as laser power was increased above 35 mW, the optimum value for the laser power from the previous OPPLIS setup. As is shown in next section, this was mainly due to a problem with the alignment of laser beam with atomic beam. More laser power does not necessarily increase the polarization since the divergence of the laser must be properly matched to the divergence of the atomic beam to optically pump the lithium.

In summary, the results of the OPPLIS test of 8/8/03 were encouraging because polarized beam was seen on-target with polarization comparable to the polarized beam seen on-target from the previous OPPLIS source setup. However, since no improvement was seen from increasing the ionizer strip temperature or increasing the laser power, further improvements to new OPPLIS source setup were necessarily. These improvements are described in the next section.

C. Changes to OPPLIS from 8/8/03 to 8/12/03

On 8/11/03, the setup of OPPLIS was scrutinized for anything that could be preventing the beam polarization from improving. The following problems with the source setup of 8/8/03 were found:

- The high mirror (M5) that reflected the laser beam to the former position of the fiber optic cable was found to be vibrating because of the design of the mirror mount. This vibration caused the laser beam spot to continually move on and off the reflective surface of the mirror resulting in varying amounts of transmitted laser power to the optical pumping region.

- The laser beam was tightly focused and only illuminated a small section of the lithium atomic beam in the optical pumping region. The fluorescence spot on the lithium atomic beam was thus also small, limiting the amount of time the atomic beam had to be optically pumped by the laser beam.

- The laser beam was also interacting with the lithium atomic beam at an odd angle (not perpendicular to the beam direction). This was due partly to the misalignment of

the mirror behind the optical pumping region that is used to eliminate the "dark state" of lithium atoms in the F=1,2, m_F=0 state (state 3). However, the laser beam had been aligned to interact with the atomic beam at this odd angle because the manual LIF scan indicated that the polarization of state 1 (F=2, m_I=+3/2, m_J=+1/2) was optimized when the laser was aligned this way. This indicated that there was some other problem with the laser optics, likely a problem with either the linear or circular polarizing optics in front of the optical pumping region.

- By applying the ¼ wave plate test to the circular polarizer in front of the optical pumping region (see Appendix C), it was discovered that the ¼ wave plate crystal was misaligned in the circular polarizer. This meant that the laser beam did not have a pure circular polarization when it interacted with the lithium atomic beam, which greatly decreased the efficiency of the optical pumping. Thus, this problem was immediately suspected to be the main reason that increasing the laser power had not improved the on-target beam polarization.

  The problems above were addressed on 8/11/03 with these improvements to the OPPLIS source setup:

- The poorly designed aluminum mount for the high mirror that was vibrating was replaced with a stainless steel mount with a broader base to damp out as much of the vibration as possible. This new mount reduced the vibration of the mirror. In addition, the new mirror mount was made ¼ inch shorter in height, allowing the laser beam to reflect off of the center of the mirror instead of the bottom edge. With this improvement, any remaining vibration of the mirror would not affect the laser beam intensity since the laser beam spot was now in the center of the reflective surface of the mirror at all times.

- The focusing lenses of the laser optics were adjusted to make the laser beam more divergent in the region where the laser beam interacted with the atomic beam. E.G. Myers et al. [21] suggest that the divergence of the laser beam in the optical pumping region of OPPLIS should be equal to the divergence of the lithium atomic beam in the same region to achieve the best optical pumping efficiency. This divergence angle is about 40 mrad, which corresponds to a laser beam spot 2.5 mm high by 6 mm wide.

The lenses of the laser optics were adjusted so that the laser beam spot had approximately these measurements in the optical pumping region.

- The retro-reflecting mirror in front of the optical pumping region was removed so that it did not reflect the laser beam back into the lithium atomic beam at any odd angles not perpendicular to the atomic beam axis.

- The ¼ wave plate crystal in the circular polarizer was rotated into the proper alignment by rotating the crystal slightly and using the ¼ wave plate test (appendix C) to check the alignment. In this way, the circular polarization of the laser beam was corrected.

- The laser beam was aligned perpendicular to the lithium atomic beam at the optical pumping region and the manual LIF scan showed that this alignment now produced the optimal optical pumping of polarization state 1 (F=2, m_I=+3/2, m_J=+1/2).

- A small amount of oxygen gas was bled onto to the tungsten ionizer strip to aid in the ionization of the lithium atomic beam and also served, in theory, to react away the unpolarized, evaporating lithium from the walls of the ionizer box.

OPPLIS was tested after these changes with LIF scans of the lithium atomic beam to determine if any improvement had been made in the polarization at the source. The LIF scan revealed that nearly all the ^{7}Li atomic beam was being pumped into polarization state 1 (F=2, m_F=2). It was also observed that the peak for state 1 on the LIF scan increased in size as the laser power going into the optical pumping region was increased from 50 mW to 150 mW and then decreased in size as the laser power was increased from 150 mW to 200 mW. Based on this observation, it was hypothesized that the polarization of the ^{7}Li atomic beam is saturated at 150mW, meaning that additional laser power would only serve to optically pump the atomic beam out of state 1 as a result of the extra scattered light and fluorescence. However, a second test of the on-target polarization would be necessary to see if any of these improvements had truly improved the polarization of the ^{7}Li beam.

D. Second test of the new OPPLIS setup, 8/12/03

The second test of the on-target beam polarization was performed on 8/12/03 using the same nuclear reaction, detector setup, and run plan used in section IV.B. In this test, the optimized values from the first source test for the Wien Filter Magnetic current

(I_{Wien} = 660 mA) and the ionizer current ($I_{Ionizer}$ = 120 A) were used since most of the source improvements described in section IV.C involved the laser beam and the laser optics. A preliminary test of the on-target polarization with the laser power at the optical pumping region = 180 mW gave the results shown in table III.3.

TABLE III.3: Preliminary test of on-target polarization on 8/12/03

Laser Power at optical pumping region = **180mW** (run 275)

unp yield	$3/2^+$	$\frac{1}{2}^+$	$\frac{1}{2}^-$	$3/2^-$	t_{10}	$3/2^-/3/2^+$
6799	2585	4830	6114	12004	0.76 ± 0.06	4.64 ± 0.1

Note the obvious improvement in both the measurement of t_{10} and ratio of the $3/2^-$ to the $3/2^+$ polarization state.

With this encouraging result, the effect of laser power on the on-target beam polarization was tested again using the same $p(^7Li,\alpha)\alpha$ reaction used in the previous test. The laser power going into the optical pumping region was varied between 60 mW and 180 mW and a measurement of the on-target beam polarization was taken in each case. The results are shown in figure III.13 and sample data from the run with the optimized value for the laser power are shown in Table III.4.

TABLE III.4: Optimized in-going Laser Power for OPPLIS on 8/12/03

Laser Power at optical pumping region = **150mW** (run 283)

unp yield	$3/2^+$	$\frac{1}{2}^+$	$\frac{1}{2}^-$	$3/2^-$	t_{10}	$3/2^-/3/2^+$
3203	1151	2400	2924	6162	0.81 ± 0.07	5.35 ± 0.17

In the previous source setup, an improvement in the on-target beam polarization was seen with the addition of the retro-reflecting mirror in front of the optical pumping region. This mirror allowed the laser to reflect through the atomic beam multiple times. This mirror was removed, as noted in section IV.C, to simplify the laser optics setup so that the problem with it could be identified. Now that the on-target beam polarization was much higher, the retro-reflecting mirror was again added to the laser optics setup for OPPLIS to see if it produced any improvement in the on-target beam polarization. The result of this test is shown in table III.5. Note that the value of t_{10} remained unchanged,

but the ratio of $3/2^-/3/2^+$ improved significantly. A possible explanation for this result is given in the next section.
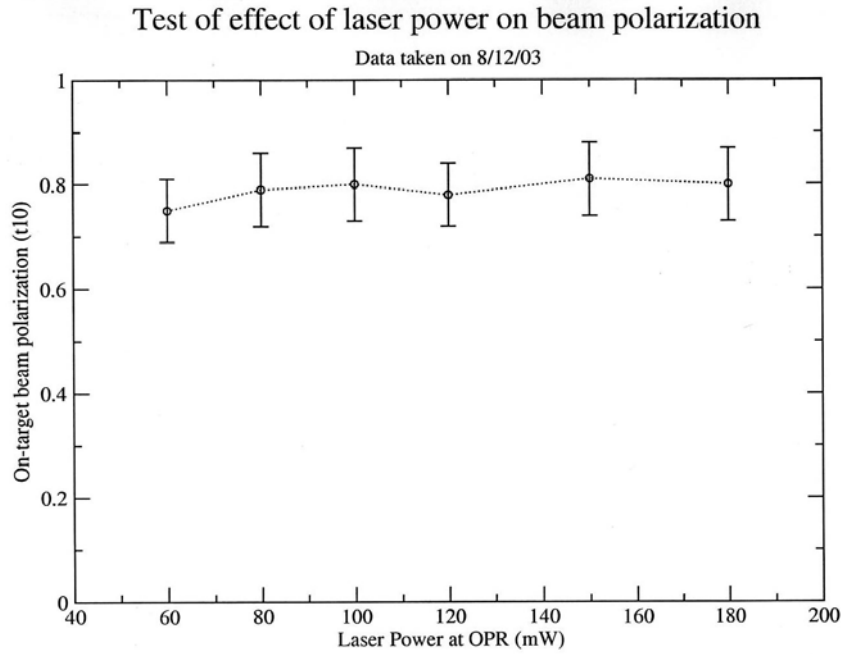

Figure III.13: On-target polarization vs. laser power on 8/12/03 with the retro-reflecting mirror (concave mirror with hole) removed. The result shown was obtained by passing the laser through the atomic beam and a single reflection back through.

TABLE III.5: Test for OPPLIS with Retro-Reflecting Mirror on 8/12/03

Laser Power at optical pumping region = **150mW** (run 289)

Retro-Reflecting Mirror added to OPPLIS laser optics setup.

unp yield	$3/2^+$	$1/2^+$	$1/2^-$	$3/2^-$	t_{10}	$3/2^-/3/2^+$
4157	1300	3256	3892	7700	0.81 ± 0.07	5.92 ± 0.18

E. Discussion of results from the OPPLIS source test of 8/12/03

The results of the OPPLIS source test on 8/12/03 show that the improvements made in section III and section IV.C significantly increased the on-target ^{7}Li beam polarization. The improvement of on-target beam polarization from $t_{10} = 0.54 \pm 0.03$ for the previous setup to $t_{10} = 0.81 \pm 0.07$ for the new setup shows this. However, this improvement would not have been possible if the problems identified in section IV.C had not been fixed. In particular, the importance of the proper alignment of the ¼ wave plate crystal can be seen comparing figure III.11 to figure III.12. When the crystal was not

103

properly aligned as in figure III.11, an increase in the laser power above 35 mW decreased the on-target polarization. In figure III.12, the crystal was properly aligned and an increase in laser power increased the on-target polarization until it was saturated at laser power greater than 150 mW. Thus, proper alignment of the laser optics is essential for not only attaining higher on-target beam polarization, but is also essential for observing any improvement in the beam polarization due to the increase in laser power.

Figure III.13 shows that although the on-target beam polarization t_{10} was improved overall on 8/12/03 when compared with figure III.12 from 8/8/03, the increase in laser power from 60 mW to 150 mW did not significantly improve the on-target polarization statistically over the course of the experiment on 8/12/03. This seems to suggest that the increased laser power had only a small effect. This result shows that the geometry of the laser alignment with the divergence of the atomic beam was most important improvement between the two setups for the two experiments. However, figure III.14 shows the effect of laser power on the $(3/2^-)/(3/2^+)$ yield ratio. Although the value of t_{10} did not change much as the laser power was increased, the $(3/2^-)/(3/2^+)$ ratio improved from 4.73 ± 0.2 at 60 mW laser power to 5.35 ± 0.2 at 150mW of laser power. So, additional laser power above 60mW has some effect on on-target polarization. The reason this improvement is not seen in the measurement of t_{10} is because if one looks at equation IV.1, the numerator in this equation does not depend on the yield measured when the beam is in the $3/2^-$ polarization state. Also, since the measurement of t_{10} does depend on the transfer of beam polarization from the $3/2^+$ polarization state to the $\frac{1}{2}^+$ and $\frac{1}{2}^-$ polarization states using the medium field transitions (MFT), it is possible that further improvements in t_{10} can be obtained by optimizing the MFT on-target using a similar method to the one used to optimize the ionizer current value and the laser power value. Further improvements are theoretically possible since the maximum possible value for t_{10} is given by $\sqrt{3s/(s+1)}$ where "s" is the nuclear spin. For ^{7}Li with s=$I_{nuclear}$=3/2, this maximum value is approximately $t_{10} \approx 1.34$ [22].
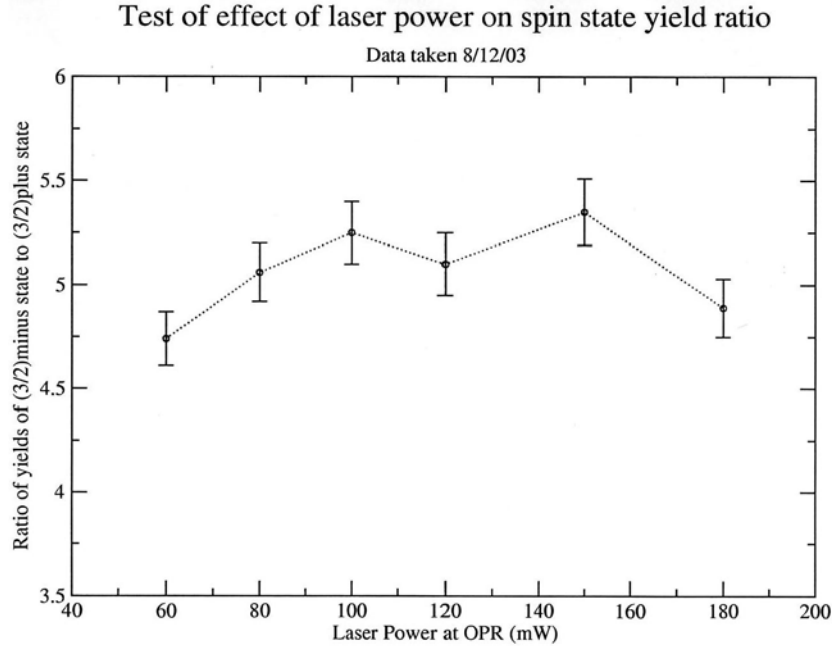
Figure III.14: Ratio of yields of spin states vs. laser power. The polarization ratio was measured to be higher with 150mW vs. the initial 60 mW of laser power.

V. Conclusion and Summary

The optically pumped polarized lithium ion source (OPPLIS) has been successfully upgraded. This was done by installing the Verdi V-5 laser as the new pump laser, moving the dye laser from the separate laser room into the ion source room, devising and installing a new optics scheme to reflect the laser beam into the optical pumping region, and the installation and testing of a new electro-optic modulator (EOM) for the laser. In addition, a new power supply for the tungsten ionizer strip capable of producing up to 200 A of current was installed to allow for higher ionizer strip temperatures.

An initial on-target test of the new source setup revealed that the on-target polarization attained was similar to that of the previous setup. Additional improvements, such as re-aligning the ¼ wave plate on the circular polarizer, improving the mount of the high reflecting mirror to decrease its vibration, re-aligning the optics of the laser to produce the proper laser beam alignment and focus with respect to the atomic beam, and bleeding oxygen gas onto the ionizer strip further increased the polarization to $t_{10} = 0.81 \pm 0.07$; a large improvement over the previous source setup.

It is hoped that the tests of the new OPPLIS source setup outlined in this paper not only have identified ways to solve problems with the on-target polarization, but also in the future will lead to a repeatable procedure to setup the ion source to give highly polarized ^{7}Li beam on target for upcoming experiments.

APPENDIX A

Operating Procedures for the Verdi Laser and Dye Laser System

I. Procedure for Powering – up the Verdi Laser / Dye Laser setup

1. Ensure the Key Switch on the front panel of the Power Supply is turned to the "Standby" position.

2. Reach to rear panel of the Power Supply and push Power Switch to the "On" position.

3. The main display on the front panel of the Power Supply should now be illuminated. The message "System Warming Up" should be displayed in the upper right hand corner of the display.

4. At this time, check the deionized water level in the Dye Laser Chiller. Fill up to top fill line and push the power button. The digital display will briefly show the temperature set point of 4.0° C, and then will show the current water temperature. Allow water to cool automatically to 4.0° C (should take ~15 minutes).

5. Turn on the Dye Pump for the Dye Laser. Flip the switch on the front panel of the dye pump to "Pump" and allow the pump to build a pressure higher than 40 psi (should only take a few seconds). When this happens, flip switch all the way up into "JET MODE" to allow dye to circulate. Optimum dye pressure is 46 psi.

6. Allow the Power Supply of the Verdi Laser approximately 45 minutes to warm its components to operating temperature. This will be done automatically.

7. When the message "Standby" is displayed in the upper right hand corner of the Power Supply display, the Verdi Laser is ready for use.

II. Operation of the Verdi Laser / Dye Laser

Ensure the message "Standby" appears in the display window on the Verdi Laser power supply.

1. Ensure the Dye Laser Chiller reads a temperature of 4.0° C.

2. Using the "Power Adjust" knob on the front panel of the Verdi Laser power supply, select your laser output wattage. The wattage will be displayed on the main display screen of the Power Supply. The desired setting will be between 3 and 4 Watts. Use between 3.5 W and 4.0 W to get Dye Laser to lase initially.

3. Turn the Key Switch to the "On" position.

4. Open the Main Shutter by pressing the "Shutter Open" button on the power supply front panel.

5. Observe that the output current displayed on the display ramps up to approximately 15 A. At this time, even at the lowest power setting, the Verdi laser will begin to lase. This will take about 5 seconds. Typical current outputs at 3 to 4 Watts are approximately 18 A.

6. To be safe, when the Laser is not in use, close the main shutter by pushing the button on the front panel of the power supply. Also, if the Laser will not be in use for an extended period of time, the life of the Laser Diodes can be saved if the "Key Switch" is turned to the "Standby" position.

III. Shutting down the Diode Laser / Dye Laser Setup

1. Turn the "Key Switch" on the front panel of the Verdi Laser power supply to the "Standby" position.

2. Close the Main Shutter by pushing the "Sputter Open" button on the power supply front panel.

3. Push the "Menu Select" button on the power supply. Scroll down and select the "LBO Settings" Submenu by pushing "Menu Select" button again.

4. The display will now display the temperature of the LBO crystal along with the temperature monitoring mode. Push the "Menu Select" button one time to execute the LBO cooling process. The message "LBO cooling" should now be displayed.

5. The temperature of the LBO crystal will begin to decrease from 150°C to 40°C. This process will take about 50 minutes and will proceed automatically.

6. Do not turn off the power switch to the Diode Laser until the LBO crystal temperature is below 40°C. Doing so will unnecessarily drain the backup power supply for the Diode Laser.

7. Turn off the Dye Pump for the Dye Laser by flipping the Dye Pump all the way down to the "off" position.

8. Turn the Chiller for the Dye Laser off by pushing the power button.

9. When the LBO crystal temperature is displayed as below 40°C on the power supply display, push the "Menu Exit" button twice to return to the main display of the Verdi Laser.

10. Push the Power Switch on the rear panel of the Verdi Laser power supply to the "Off" position. The Verdi Laser is now properly powered down.

IV. TroubleShooting for the Dye Laser

If the dye laser does not lase when 3.5 W to 4.0 W of laser power from the Verdi Laser is put into it initially, the internal mirrors of the dye laser may require some tuning to account for changes in temperature and humidity in the air since the last time the dye laser was used. The following procedure can be used to fix a minor misalignment of the internal mirrors inside the dye laser. If it is not successful, the full mirror alignment procedure outlined in the dye laser manual may be necessary.

1. With the pump beam from the Verdi laser between 3.5 and 4.0 Watts, use a white card to observe the output of the dye laser. Ideally, you should see 3 fluorescence spots, one green and the others orange. If this is true, proceed to step 2.

2. Carefully remove the top cover of the dye laser, taking care not to bump the tuning knobs or the internal mirrors of the dye laser. Also, do not position your head directly above the dye laser optics as the lasers may reflect into your eyes.

3. Most likely, the "output coupler" of the dye laser shown in figure A.IV.1 is slightly misaligned. It can be misaligned vertically, horizontally, or both. With your hand, carefully push on the output coupler in the hortizontal direction and pull on the coupler in the vertical direction while observing the fluorescence spots from the output of the dye laser on a white card. If all goes well, a brief period of lasing should be observed while this manipulation of the output coupler is occurring.
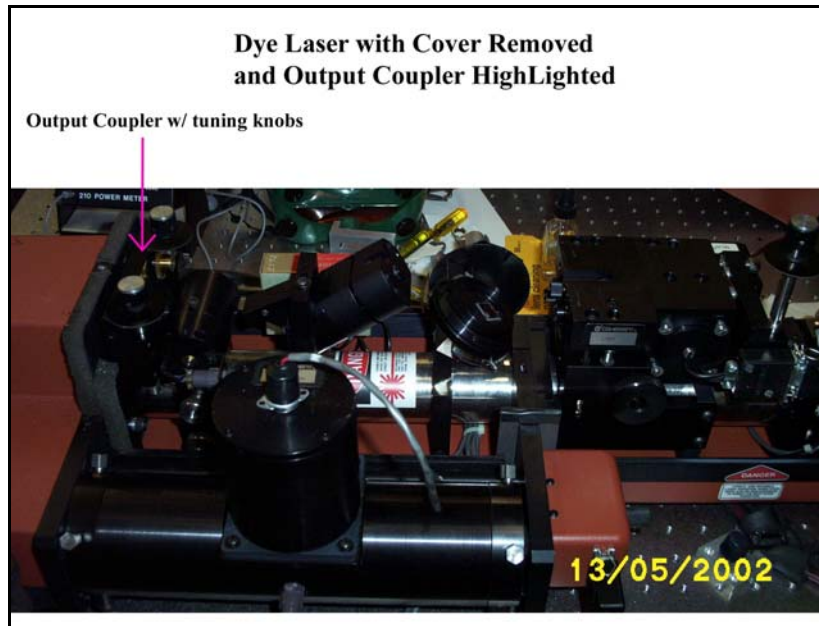
Figure A.IV.1: Dye laser output coupler.

4. Use the tuning knobs for the output coupler to adjust the vertical and horizontal position of the output coupler until a constant lasing is achieved. Use the laser power meter to observe the output laser power while optimizing the position of the dye laser mirrors. In general, you should only have to tune the output coupler and the low input mirror to achieve stable output laser power from the dye laser.

5. Carefully replace the dye laser cover over the dye laser optics. Once it is lasing, the dye laser usually continues to lase, although further tuning of the dye laser mirrors may be necessary to stabilize and optimize the laser power output of the dye laser.

APPENDIX B

Procedure to adjust the new EOM1 on resonant frequency the Voltage Controlled Oscillator (VCO)

1. Setup the rf circuit for EOM1 as shown in figure III.8.

2. Set the rf attenuators to 30 dB initially.

3. Turn on the rf amplifier. Observe the forward and reflected rf power on the rf power meter. The forward power should be about 0.6W. Allow the rf amplifier to warm up for about 10 minutes. As the amplifier warms up, the forward rf power will decrease slightly.

4. Decrease the rf attenuation to 27 dB while observing the forward and reflected rf power on the rf power. Adjust the voltage on the potentiometer of the VCO to allow the resonant cavity to oscillate at its resonant frequency (this can be attained by minimizing the reflected rf power as read by the rf power meter). As the cavity electronics heat up, the voltage on the VCO will have to be decreased to account for the change in the resonant frequency of the cavity.

5. Wait about 15 minutes for the cavity to warm up to its operating temperature. You may have to tune the VCO slightly a few times.

6. When the EOM1 cavity is more or less stable at 27 dB, decrease the rf attenuation further until the forward rf power going into the cavity is about 2.6W (should be around 22 dB). Adjust the voltage on the VCO such that the reflected power approaches $0.030 \text{ W} \pm 0.005$. The cavity will stabilize at this power input after about 30 minutes.

7. Continue to monitor the reflected rf power with the rf power meter to ensure the EOM1 cavity oscillates at or near 402 MHz (6.76 ± 0.02 V). If the cavity's resonant frequency drifts away from 402 MHz, it may be necessary to tweak the the tuning screw on top of the resonant cavity to adjust the resonant frequency of cavity back to the proper value.

APPENDIX C

Procedure for testing the ¼ wave plate

The setup of the optics around the optical pumping region allows the ¼ wave plate alignment in the circular polarizer to be easily tested. The test for the ¼ wave plate works on the principle that if a linearly polarized laser beam is converted to pure left or right circular polarization by a properly aligned ¼ wave plate and then hits a mirror perpendicular to the path of the laser beam, the resulting reflected laser beam will have the opposite circular polarization. This reflected laser beam is converted back to a linearly polarized beam when it passes back through the ¼ wave plate, but the polarization is rotated 90° with respect to the original linear polarization. Thus when the reflected laser beam passes through the linear polarizer again, it is completely absorbed instead of transmitted. However, any deviation in the alignment of the ¼ wave plate results in the transmission of the improperly polarized portion of the laser beam. This transmitted laser beam can be viewed as shown in figure C.1. The following is the procedure for testing and aligning the ¼ wave plate in the circular polarizer.

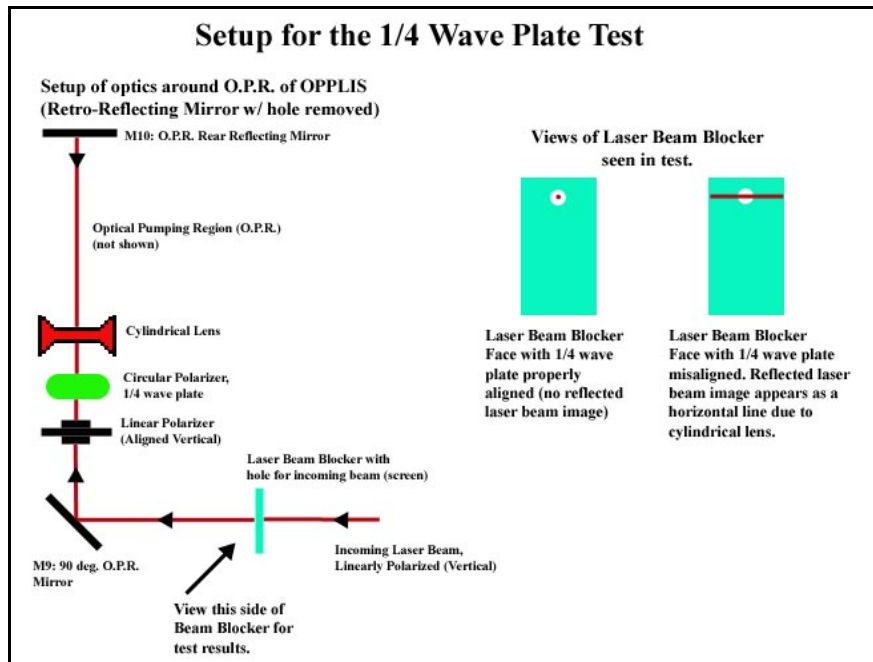**Figure C.1:** ¼ - wave plate test diagram

1. Remove the front retro-reflecting mirror (concave mirror with the hole) from in front of the optical pumping region.

2. Insert the laser beam blocker with the hole for the incoming laser beam (screen) as shown in figure C.1. Align with incoming laser beam so that it passes though the hole.

3. Observe reflected laser beam on back of beam blocker. If ¼ wave plate crystal is properly aligned in the circular polarizer, there will be no reflected laser light on back of beam blocker.

4. If the ¼ wave plate is misaligned, there will be a horizontal laser light line on the back of the beam blocker. Rotate the circular polarizer manually until the horizontal line disappears. This is the position of proper alignment of the ¼ wave plate crystal.

5. Mark alignment of ¼ wave plate crystal. Take circular polarizer out of its mount and remove ¼ wave plate crystal by removing front face of the rotating section of the circular polarizer. Rotate ¼ wave plate crystal such that it is properly aligned with the vertical linear polarizer (90 deg.). Put circular polarizer back together.

6. Perform ¼ wave plate test again to test alignment of ¼ wave plate. It may take several tries to get the ¼ wave plate properly aligned with the linear polarizer, thus producing the situation where there is no reflected laser light on the beam blocker.

APPENDIX D

A Procedure to Get Polarized ^{7}Li Beam on target

1. Heat lithium oven to above 750° C while the oven vacuum is less than 4 X10^{-6} on the Penning gauge. Heat tungsten ionizer strip to 114 A (120 A on power supply) and observe beam current. Extraction current should be greater than 25 μA and current on cup 1 of the source should be greater than 10 μA.

2. While lithium oven is heating, start up Verdi laser and dye laser system using procedure in Appendix A.

3. Use procedure in Appendix B to lock the EOM1 on its resonant frequency. Forward power into the EOM should be between 2.6 and 2.7 W. Reflected power should be kept less than 0.030 W.

4. Remove Retro-Reflecting mirror with hole in front of O.P.R. if applicable.

5. Illuminate lithium atomic beam with laser from dye laser and EOM.

6. Find the fluorescence peak of the atomic beam by tuning the dye laser frequency while illuminating the atomic beam in the optical pumping region. In the beginning, use about 50 mW of laser power going into the optical pumping region.

7. Tune mirrors and lenses such that the laser beam is perpendicular to the atomic beam in the optical pumping region.

8. Perform ¼ wave plate test as described in Appendix C. Fix any problems observed with alignment of ¼ wave plate crystal.

9. Rotate circular polarizer 90 degrees using automatic motor turn. Verify that circular polarizer rotates without getting stuck. Also verify that reflected horizontal laser light line is not seen in either the left or right rotation of the circular polarizer (verifies 90 deg. rotation).

10. Adjust laser divergence to match vertical and horizontal divergence of the atomic beam. Fluorescence spot size should be about 2.5 mm high by 6 mm wide.

11. Cool off ionizer strip (take current to 0 A) and withdraw out of atomic beam. Turn on LIF scan power supply and photo-multiplier tube. Perform LIF scan.

12. Tweak mirrors and lenses around optical pumping region to maximize state 1 polarization peak on LIF scan. A good goal is to have the state 1 peak about 10

times as large as the state 2 peak in height (or no state 2 peak). Some improvement may also be observed if laser power into O.P.R. is increased to 150 mW.

13. If running all four polarization states, test transfer to states 2 and 3 by setting MFT power supply current with the computer. Note that this test should be done by having the computer switch the states to simulate the change in the MFT power supply current during a normal run. Typically, the MFT supply is set to 2.30 A for state 3 and 2.40 A for state 2.

14. When LIF scan is satisfactory, turn off LIF photo-multiplier tube and re-insert ionizer strip. Heat ionizer strip to 114 A (120 A on supply). Tune ion source deflectors so that between 5-7 μA of atomic beam is on cup 2.

15. Heat cesium charge exchange cell to 150° C in the center and 200° C in the reservoir (55-60 A on reservoir heater). Negative beam should appear on cup 2.

16. Bleed a small amount of oxygen gas on to tungsten ionizer strip. Vacuum in ionizer region should not be allowed to be greater than 3 X10^{-6} on the ionizer Penning gauge while oxygen is on.

17. Accelerate beam and put on target. Perform a test similar to those described in Chapter 3:Section III to verify that beam is polarized.

18. For additional on-target polarization, insert retro-reflecting mirror with hole in front of optical pumping region and align such that ingoing laser beam goes through the hole, but reflected laser beam hits mirror slightly off center from the hole.

REFERENCES

FOREWARD

[1] P.G. Hansen and J.A. Tostevin, Annu. Rev. Nucl. Part. Sci. **53**, 219 (2003).

[2] C.A. Bertulani and P.G. Hansen, Phys. Rev. **C70**, 034609 (2004).

[3] E.G. Myers, A.J. Mendez, B.G. Schmidt, and K.W. Kemper, Nucl. Instr. and Meth. **B56/57**, 1156-1160 (1991).

[4] P.D. Cathers, P.V. Green, E.E. Bartosz, M.W. Cooper, N. Curtis, N. Keeley, K.W. Kemper, F. Maréchal, E.G. Myers, B.G. Schmidt, K. Rusek, and V. Hnizdo, Phys. Rev. **C63**, 064601 (2001).

CHAPTER 1

[1] N.K. Glendenning, in Nuclear Spectroscopy and Reactions, edited by J. Cerny (Academic, New York, 1975), Pt. D., p. 319.

[2] J.R. Erskine, A. Marinov, and J.P. Schiffer, Phys. Rev. **142**, 633, (1966).

[3] D.D. Armstrong and A.G. Blair, Phys. Rev. **140**, B1226, (1965).

[4] P. Doll, G. Mairle, H. Breuer, K.T. Knöpfle, T. Tohei, and G.J. Wagner, J. Phys. G: Nucl. Phys. **Vol. 5, No. 10**, 1421 (1979).

[5] Eugene Eichler, and Subramanian Raman, Phys. Rev. **C3**, 2268, (1971).

[6] K.W. Kemper, A.F. Zeller, and T.R. Ophel, Nucl. Phys. **A348**, 339 (1980).

[7] Maria G. Mayer and J. Hans D. Jensen, Elementary Theory of Nuclear Shell Structure. (Wiley, New York, 1955).

[8] T.W. Burrows, Nuclear Data Sheets **68**, 1 (1993).

[9] R.B. Firestone, V.S. Shirley, Table of Isotopes: 8th Edition, (Wiley, New York, 1996) Vol. 1.

[10] J. Hufner, K.Schafer, and B. Schurmann, Phys. Rev. **C12**, 1888 (1975).

[11] B. Blank, S. Andriamonje, R. Del Moral, J.P. Dufour, A. Fleury, T. Josso, M.S. Pravikoff, S. Czajkowski, Z. Janas, A. Piechaczek, E. Roeckl, K.-H. Schmidt, K. Sümmerer, W. Trinder, M. Weber, T. Brohm, A. Grewe, E. Hanelt, A. Heinz, A. Junghans, C. Röhl, S. Steinhäuser, B. Voss, M. Pfützner, Phys. Rev. **C 50**, 2398 (1994).

[12] P.G. Hansen and J.A. Tostevin, Annu. Rev. Nucl. Part. Sci. **53**, (2003) 219.

[13] E. Sauvan, F. Carstoiu, N.A. Orr, J.S. Winefield, M. Freer, J.C. Angelique, W.N. Catford, N.M. Clarke, N. Curtis, S.Grevy, C. LeBrun, M. Lewitowicz, E. Liegard, F.M. Marques, M. Mac Cormick, P. Roussel-Chomaz, M.-G. Saint-Laurent and M. Shawcross, Phys. Rev. C **69**, 044603 (2004).

[14] F. Carstoiu, E. Sauvan, N.A. Orr, A. Bonaccorso, Phys. Rev. C **70**, 054602 (2004).

[15] A. Gade, D. Bazin, B.A. Brown, C.M. Campbell, J.A. Church, D.C. Dinca, J. Enders, T. Glasmacher, P.G. Hansen, Z. Hu, K.W. Kemper, W.F. Mueller, H. Olliver, B.C. Perry, L.A. Riley, B.T. Roeder, B.M. Sherrill, J.R. Terry, J.A. Tostevin, K.L. Yurkewicz, Phys. Rev. C **69**, 034311 (2004)

[16] A. Gade, D. Bazin, C.A. Bertulani, B.A. Brown, C.M. Campbell, J.A. Church, D.C. Dinca, J. Enders, T. Glasmacher, P.G. Hansen, Z. Hu, K.W. Kemper, W.F. Mueller, H. Olliver, B.C. Perry, L.A. Riley, B.T. Roeder, B.M. Sherrill, J.R. Terry, J.A. Tostevin, K.L. Yurkewicz, Phys. Rev. C **71**, 051301, (2005).

[17] J. Fridmann, I. Wiedenhover, A. Gade, L.T. Baby, D. Bazin, B.A. Brown, C.M. Campbell, J.M. Cook, P.D. Cottle, E. Diffenderfer, D.-C. Dinca, T. Glasmacher, P.G. Hansen, K.W. Kemper, J.L. Lecouey, W.F. Mueller, H. Olliver, E. Rodriguez-Vieitez, J.R. Terry, J.A. Tostevin, K. Yoneda, Nature Vol. 435 (2005) 922.

[18] H. Ryuto, M. Kunibu, T. Minemura, T. Motobayashi, K. Sagara, S. Shimoura, M. Tamaki, Y. Yanagisawa, Y. Yano, Nucl. Instr. and Meth. **A 555**, 1 (2005).

[19] D.J. Griffiths, Introduction to Electrodynamics: Third Edition. (Prentice Hall, New Jersey, 1998). Chapter 12.2.4, 519-520.

[20] W.E. Burcham, Nuclear Physics: An Introduction. (McGraw-Hill, New York, 1963). Chapter 5.2, 154-155.

[21] D. Bazin, J.A. Carggiano, B.M. Sherrill, J. Yurkon, A.F. Zeller, Nucl. Instr. Meth. Phys. Res. **B 204**, (2003) 629.

[22] W.F. Mueller, J.A. Church, T. Glasmacher, D. Gutknecht, G. Hackman, P.G. Hansen, Z. Hu, K.L. Miller, P. Quirin, Nucl. Instr. and Meth. **A 466**, (2001) 492.

[23] J. Yurkon, D. Bazin, W. Benenson, D.J. Morrissey, B.M. Sherrill, D. Swan, R. Swanson, Nucl. Instr. and Meth. **A 422**, 291 (1999).

[24] R.B. Firestone, V.S. Shirley, Table of Isotopes: 8th Edition, (Wiley, New York, 1996) Vol. 2. Appendix C.

[25] see, for example, D.C. Radford, http://radware.phy.ornl.gov/gf3/gf3.html.

[26] W.F. Mueller, *private communication.*

[27] Z. Hu, T. Glasmacher, W.F. Mueller, I. Wiedenhöver, Nucl. Instr. and Meth. **A 482**, 715 (2002).

[28] D. Bazin, O. Tarasov, M. Lewitowicz, O. Sorlin, Nucl. Instr. Meth. A **482**, 307 (2002); O.Tarasov, D. Bazin, Nucl. Phys. **A 746**, 411 (2004).

[29] W.E. Burcham, Nuclear Physics: An Introduction. (McGraw-Hill, New York, 1963). Chapter 5.1, 142-144.

[30] D.J. Griffiths, Introduction to Quantum Mechanics. (Prentice Hall, New Jersey, 1995). Chapter 11.1, 355.

[31] J.R. Taylor, An Introduction to Error Analysis: Second Edition. (University Science Books, Sausalito, California, 1997). Chapter 3, 58.

[32] M. Mocko, M.B. Tsang, L. Andronenko, M. Andronenko, F. Delaunay, M. Famiano, T. Ginter, H. Hua, S. Lukyanov, W. G. Lynch, A. Ono, A. Rogers, M. Steiner, A. Stolz, O. Tarasov, M.-J. van Goethem, G. Verde, M. S. Wallace, *in preparation.*

[33] K. Sümmerer, W. Brüchle, D.J. Morrissey, M. Schädel, B. Szweryn, and Yang Weifan, Phys. Rev. **C 42**, 2546, (1990).

[34] A. Obertelli, A. Gade, D. Bazin, C.M. Campbell, J.M. Cook, P.D. Cottle, A.D. Davies, D.-C. Dinca, T. Glasmacher, P.G. Hansen, T. Hoagland, K.W. Kemper, J.-L. Lecouey, W.F. Mueller, R.R. Reynolds, B.T. Roeder, J.R. Terry, J.A. Tostevin, K. Yoneda, H. Zwahlen, Phys. Rev. **C 73**, 044605 (2006).

[35] Yu.L. Parfenova and M.V. Zhukov, Eur. Phys. J. A **12**, 191 (2001)

[36] J.F. Lecolley, C. Varignon, J. Thum, F. Borne, E. Martinez, S. Ménard, Ph. Pras, A. Boudard, J.C. Duchazeaubeneix, D. Durand, J.M. Durand, J. Fréhaut, F. Hanappe, C. Le Brun, F.R. Lecolley, X. Ledoux, F. Lefebvres, R. Legrain, S. Leray, M. Louvel, G. Milleret, Y. Patin, L. Stuttgé, Y. Terrien, Eur. Phys. J. A **5**, 321, (1999).

[37] D. Ridikas, W. Mittig, H. Savajols, P. Roussel-Chomaz, S.V. Förtsch, J.J. Lawrie, G.F. Steyn, Phys. Rev. C **63**, 014610, (2000).

CHAPTER 2

[1] R.C. Johnson and P.J.R. Soper, Phys. Rev. C 1, 976 (1970).

[2] J.D. Harvey and R.C. Johnson, Phys. Rev. C **3**, 636 (1971).

[3] J.W. Watson, W. Pairsuwan, B.D. Anderson, A.R. Baldwin, B.S. Flanders, C. Lebo R. Madey, J.D. Brown, C.C. Foster, D.L. Friesel, H. Nann, E.J. Stephenson, P.B. Foot, G.G. Shute, B.M. Spicer, Phys. Rev. C **40**, 570, (1989).

[4] X.D. Liu, M.A. Famiano, W.G. Lynch, M.B. Tsang, J.A. Tostevin, Phys. Rev. C **69**, 064313, (2004).

[5] N.K. Glendenning, in *Nuclear Spectroscopy and Reactions*, edited by J. Cerny (Academic, New York, 1975), Pt. D., p. 319.

[6] G.L. Wales and R.C. Johnson, Nucl. Phys. **A274**, 168, (1976).

[7] R.C. Johnson and P.C. Tandy, Nucl. Phys. **A235**, 56, (1974).

[8] P.J.A. Buttle and L.J.B. Goldfarb, Proc. Phys. Soc. London, 83, 701 (1964).

[9] L.D. Knutson, J.A. Thomson and H.O. Meyer, Nucl. Phys. **A241**, 36 (1975).

[10] J.P. Jeukenne, A. Lejeune, and C. Mahaux, Phys. Rev. C **16**, 80 (1977).

[11] R.V. Reid, Jnr., Ann. Phys. (N.Y.) **50**, 411, (1968).

[12] J.S. Petler, M.S. Islam, R.W. Finlay, and F.S. Dietrich, Phys. Rev. C **32**, 673 (1985).

[13] J.W. Negele and K. Yazaki, Phys. Rev. Lett. **47**, 71 (1981).

[14] S. Fantoni, B.L. Friman, and V. Pandharipande, Phys. Lett. B **104**, 89 (1981).

[15] S. Mellema, R.W. Finlay, F.S. Dietrich, and F. Petrovich, Phys. Rev. C 28, 2267 (1983).

[16] B.A. Brown, Phys. Rev. C **58**, 220 (1998).

[17] F. Perey and B. Buck, Nucl. Phys. **32**, 353 (1962).

[18] M. Igarashi, et al. Computer Program TWOFNR (Surrey University version).

[19] J.R. Erskine, A. Marinov, and J.P. Schiffer, Phys. Rev. **142**, 633, (1966).

[20] D.D. Armstrong and A.G. Blair, Phys. Rev. **140**, B1226, (1965).

[21] K.W. Kemper, A.F. Zeller, and T.R. Ophel, Nucl. Phys. **A348**, 339 (1980).

[22] Eugene Eichler, and Subramanian Raman, Phys. Rev. **C3**, 2268, (1971).

[23] W.D. Metz, W.D. Callender, and C.K. Bockelman, Phys. Rev. **C12**, 827, (1975).

[24] Y. Uozumi, O. Iwamoto, S. Widodo, A. Nohtomi, T. Sakae, M. Matoba, M. Nakano, T. Maki, and N. Koori, Nucl. Phys. **A576**, 123, (1994).

[25] T.W. Burrows, Nuclear Data Sheets, **76**, 191, (1995)

[26] T.R. Canada, C. Ellegaard, and P.D. Barnes, Phys. Rev. **C4**, 471, (1971).

[27] J. Ollier, R.Chapman, X.Liang, M.Labiche, K.-M.Spohr, M.Davison, G.de Angelis, M.Axiotis, T.Kroll, D.R.Napoli, T.Martinez, D.Bazzacco, E.Farnea, S.Lunardi, A.G.Smith, Phys. Rev. **C67**, 024302, (2003).

[28] O. Sorlin, Zs.Dombradi, D.Sohler, F.Azaiez, J.Timar, Yu.-E.Penionzhkevich, F.Amorini, D.Baiborodin, A.Bauchet, F.Becker, M.Belleguic, C.Borcea, C.Bourgeois, Z.Dlouhy, C.Donzaud, J.Duprat, L.Gaudefroy, D.Guillemaud-Mueller, F.Ibrahim, M.J.Lopez, R.Lucas, S.M.Lukyanov, V.Maslov, J.Mrazek, C.Moore, F.Nowacki, F.Pougheon, M.G.Saint-Laurent, F.Sarazin, J.A.Scarpaci, G.Sletten, M.Stanoiu, C.Stodel, M.Taylor, Ch.Theisen, Eur. Phys. J. **A22**, 173, (2004).

[29] H. Scheit, T.Glasmacher, B.A.Brown, J.A.Brown, P.D.Cottle, P.G.Hansen, R.Harkewicz, M.Hellstrom, R.W.Ibbotson, J.K.Jewell, K.W.Kemper, D.J.Morrissey, M.Steiner, P.Thirolf, M.Thoennessen, Phys. Rev. Lett. **77,** 3968 (1996).

[30] P.G. Hansen and J.A. Tostevin, Annu. Rev. Nucl. Part. Sci. **53**, (2003) 219.

[31] E. Sauvan, F. Carstoiu, N.A. Orr, J.S. Winefield, M. Freer, J.C. Angelique, W.N. Catford, N.M. Clarke, N. Curtis, S.Grevy, C. LeBrun, M. Lewitowicz, E. Liegard, F.M. Marques, M. Mac Cormick, P. Roussel-Chomaz, M.-G. Saint-Laurent and M. Shawcross, Phys. Rev. C **69**, 044603 (2004).

[32] F. Carstoiu, E. Sauvan, N.A. Orr, A. Bonaccorso, Phys. Rev. C **70**, 054602 (2004).

[33] A. Gade, D. Bazin, B.A. Brown, C.M. Campbell, J.A. Church, D.C. Dinca, J. Enders, T. Glasmacher, P.G. Hansen, Z. Hu, K.W. Kemper, W.F. Mueller, H. Olliver, B.C. Perry, L.A. Riley, B.T. Roeder, B.M. Sherrill, J.R. Terry, J.A. Tostevin, K.L. Yurkewicz, Phys. Rev. C **69**, 034311 (2004)

[34] A. Gade, D. Bazin, C.A. Bertulani, B.A. Brown, C.M. Campbell, J.A. Church, D.C. Dinca, J. Enders, T. Glasmacher, P.G. Hansen, Z. Hu, K.W. Kemper, W.F. Mueller, H. Olliver, B.C. Perry, L.A. Riley, B.T. Roeder, B.M. Sherrill, J.R. Terry, J.A. Tostevin, K.L. Yurkewicz, Phys. Rev. C **71**, 051301, (2005).

[35] J.A. Tostevin, Nucl. Phys. A682, 320c-331c, (2001)

[36] J.A. Tostevin, "Reaction Theories for Exotic Nuclei", <u>Proceedings of the 3rd Balkan School on Nuclear Physics</u>, Thessaloniki, September 18-24, 2002, 221-242.

[37] R.J. Glauber, in <u>Lectures in Theoretical Physics</u>, ed. By W.E. Brittin (Interscience, New York, 1959) Vol. 1, Pg. 315.

[38] W. Glockle, H.Witala, D.Huber, H.Kamada, J.Golak, Phys. Rep. 274, 107, (1996)

[39] H. Witala, Private Communication (2004)

[40] J.A. Tostevin, J. Phys. G 25, 735, (1999)

[41] L. Ray, Phys. Rev. C 20, 1857, (1979)

[42] J.L. Yntema, Phys. Rev. **186**, 1144, (1969)

[43] P. Martin, M. Buenard, Y. Dupont, M. Chabre, Nucl. Phys. **A185**, 465 (1972)

[44] D.E. Alburger, E.K. Warburton, and B.A. Brown, Phys. Rev. **C30**, 1005, (1984)

[45] S.M. Banks, B.M. Spicer, G.G. Shute, V.C. Officer, G.J. Wagner, W.E. Dollhopf, L. Qingli, C.W. Glover, D.W. Devins, and D.L. Friesel, Nucl. Phys. **A437**, 381 (1985).

[46] C.A. Ogilvie, D.Barker, J.B.A.England, M.C.Mannion, J.M.Nelson, L.Zybert, R.Zybert, Nucl. Phys. **A465**, 445, (1987).

[47] J.A. Cameron and B. Singh, Nuclear Data Sheets **102**, 293, (2004). B. Singh and J.A. Cameron, Nuclear Data Sheets, **92**, 1, (2001). T.W. Burrows, Nuclear Data Sheets **68**, 1 (1993).

[48] J.A. Cameron and B. Singh, Nuclear Data Sheets **92**, 783, (2001).

[49] T.W. Burrows, Nuclear Data Sheets, **65**, 1, (2002).

[50] C.A. Bertulani and P.G. Hansen, Phys. Rev. C70, 034609 (2004)

[51] J. Lee, J.A. Tostevin, B.A. Brown, F. Delaunay, W.G. Lynch, M.J. Saelim, and M.B. Tsang, Phys. Rev. **C 73**, 044608 (2006).

[52] V.R. Pandharipande, I. Sick, and P.K.A. de Witt Huberts, Rev. Mod. Phys. **69**, 981, (1997).

CHAPTER 3
[1] H. Amakawa and K.I. Kubo, Nucl. Phys. **A266**, 521, (1976).

[2] H. Nishioka, J.A. Tostevin, R.C. Johnson, and K.I. Kubo, Nucl. Phys. **A415**, 230, (1984).

[3] T. Matsumoto, T. Kamizato, K. Ogata, Y. Iseri, E. Hiyama, M. Kamimura, and M. Yahiro, Phys. Rev. **C68**, 064607, (2003).

[4] M. Simonius, "Theory of polarization measurements, observables, amplitudes, and symmetries", in: Lecture Notes in Physics, vol. 30, ed. D. Fick (Springer, Heidelberg, 1974), Pg. 48, eg. 3.27.

[5] P.D. Cathers, E.E. Bartosz, M.W. Cooper, N. Curtis, N. Keeley, K.W. Kemper, F. Maréchal, E.G. Myers, B.G. Schmidt, K. Rusek, and V. Hnizdo, Phys. Rev. C 63, 064601, Pg. 3.

[6] H. Jänsch, K. Becker, K. Blatt, H. Leucker, D. Fick, R. Butsch, B. Heck, D. Krämer, K.H. Möbius, W. Ott, P. Paul, R. Suntz, G. Tungate, I.M. Turkiewicz, A. Weller, and E. Steffens, Nucl. Instr. and Meth. **A254**, 7, (1987).

[7] A.J.Mendez, E.G. Myers, K.W.Kemper, P.L. Kerr, E.L. Reber, and B.G. Schmidt, Nucl. Instr. and Meth. **A329**, 37-45, (1993).

[8] P.D. Cathers, P.V. Green, E.E. Bartosz, K.W. Kemper, F. Maréchal, E.G. Myers, and B.G. Schmidt, Nucl. Instr. and Meth. A457 (2001) 509-516.

[9] D.P. Sanderson, A polarized ^{6}Li source and a study of polarization effects in the scattering of ^{3}He and ^{6}Li. Florida State University PhD Dissertation, 1986.

[10] E.G. Myers, A.J. Mendez, B.G. Schmidt, and K.W. Kemper, Nucl. Instr. and Meth. B56/57 (1991) 1156-1160.

[11] Peter V. Green, Analyzing Powers in Light Systems and ^{6,7}Li Beam Polarization Studies. Florida State University PhD Dissertation, 1995, Pg. 65.

[12] A. J. Mendez, An Optically Pumped Polarized Lithium Ion Source and an Investigation of ^{12}C(^{6}Li,α)^{14}N. Florida State University, PhD Dissertation, 1993, Pgs. 33-41.

[13] Operator's Manual for Verdi V-2/V-5 Diode Pumped Lasers, Coherent Inc., section 7-7.

[14] User's Manual for High-Frequency Electro-Optic Phase Modulators Model Series 4421, New Focus Inc., Pg. 18.

[15] P. Zupranski, W. Dreves, P. Egelhof, E. Steffens, D. Fick, and F. Rosel, Nucl. Instr. and Meth. 167 (1979) 193-200.

[16] G.R. Plattner, T.B. Clegg, L.G. Keller, Nucl. Phys. **A111**, 481, (1968).

[17] G. Tungate, W. Ott, and H. Leucker, Z. Phys. A 321 (1985) 103-105.

[18] P.D. Cathers, E.E. Bartosz, M.W. Cooper, N. Curtis, N. Keeley, K.W. Kemper, F. Maréchal, E.G. Myers, B.G. Schmidt, K. Rusek, and V. Hnizdo, Phys. Rev. C 63, 064601, Pg. 3.

[19] Peter V. Green, <u>Analyzing Powers in Light Systems and ^{6,7}Li Beam Polarization Studies</u>. Florida State University PhD Dissertation, 1995,, Pg. 57.

[20] Peter V. Green, <u>Analyzing Powers in Light Systems and ^{6,7}Li Beam Polarization Studies</u>. Florida State University PhD Dissertation, 1995, Pg. 42.

[21] - E.G. Myers, A.J. Mendez, B.G. Schmidt, and K.W. Kemper, P.L. Kerr, and E.L. Reber, Nucl. Instr. and Meth. B79 (1993) 701-704.

[22] – M. Simonius, "Theory of polarization measurements, observables, amplitudes, and symmetries", in: <u>Lecture Notes in Physics, vol. 30,</u> ed. D. Fick (Springer, Heidelberg, 1974), Pg. 48, eq. 3.27.

BIOGRAPHICAL SKETCH

Brian T. Roeder

The author was born on January 19, 1979, in Flint, Michigan. He grew up in the small town of Holly, Michigan. His interest in physics developed after a visit to Space Camp in Huntsville, Alabama, when he was 14, where he first realized that space travel was not as simple as just "flying around in space" as is depicted in most television shows. He excelled in his high school studies at Holly High School, graduating as co-valedictorian of the class of 1997. From there, he pursued his undergraduate studies at Michigan State University in East Lansing, Michigan. While originally hoping to study medicine, the opportunity of a job at the National Superconducting Cyclotron Laboratory (NSCL) led him to an interest in nuclear physics. At the NSCL, he helped to develop an automated system for filling germanium detectors with liquid nitrogen. He also spent a summer during his undergraduate years studying French language in Tours, France. He received his Bachelor of Science degree in physics from Michigan State University in May 2001. Then, beginning in June 2001, he began graduate school at Florida State University in Tallahassee, Florida. He spent his first year teaching astronomy laboratory classes, and then became a research assistant in nuclear physics research for Professor Kirby Kemper in May 2002. While a research assistant for Professor Kemper, Brian was involved as either first or second author in the following journal publications:

1. B.T. Roeder, K.W. Kemper, N. Aoi, D. Bazin, M. Bowen, C.M. Campbell, J.M. Cook, D.-C. Dinca, A. Gade, T. Glasmacher, H. Iwasaki, S. Kanno, T. Motobayashi, W.F. Mueller, T. Nakamura, H. Sakurai, H. Suzuki, S. Takeuchi, J.R. Terry, and K. Yoneda, H. Zwahlen, "*Production cross sections for heavy-ion fragmentation reactions on a liquid deuteron target at intermediate energy*," submitted to Phys. Rev. C.
2. O.A. Momotyuk, N. Keeley, K.W. Kemper, B.T. Roeder, A.M. Crisp, W. Cluff, B.G. Schmidt, M. Wiedeking, F. Maréchal, K. Rusek, S. Yu. Mezhevych, J. Liendo, "*Target Independent ^{7}Li Elastic Scattering at Low Momentum Transfers*," submitted to Physics Letters B.
3. A.M. Crisp, B.T. Roeder, N. Keeley, K.W. Kemper, F. Maréchal, O. Momotyuk, K. Rusek, W. Weintraub, and M. Wiedeking, "*5p-4h cluster states in ^{17}O measured with five particle transfer reactions*," in preparation.